

University of Windsor

Scholarship at UWindor

Electronic Theses and Dissertations

Theses, Dissertations, and Major Papers

2017

Quantum Control of Open Systems and Dense Atomic Ensembles

Christopher DiLoreto
University of Windsor

Follow this and additional works at: <https://scholar.uwindsor.ca/etd>

Recommended Citation

DiLoreto, Christopher, "Quantum Control of Open Systems and Dense Atomic Ensembles" (2017).
Electronic Theses and Dissertations. 5976.
<https://scholar.uwindsor.ca/etd/5976>

This online database contains the full-text of PhD dissertations and Masters' theses of University of Windsor students from 1954 forward. These documents are made available for personal study and research purposes only, in accordance with the Canadian Copyright Act and the Creative Commons license—CC BY-NC-ND (Attribution, Non-Commercial, No Derivative Works). Under this license, works must always be attributed to the copyright holder (original author), cannot be used for any commercial purposes, and may not be altered. Any other use would require the permission of the copyright holder. Students may inquire about withdrawing their dissertation and/or thesis from this database. For additional inquiries, please contact the repository administrator via email (scholarship@uwindsor.ca) or by telephone at 519-253-3000ext. 3208.

Quantum Control of Open Systems and Dense Atomic Ensembles

By

Christopher DiLoreto

A Dissertation

Submitted to the Faculty of Graduate Studies
through the Department of Physics
in Partial Fulfillment of the Requirements for
the Degree of Doctor of Philosophy
at the University of Windsor

Windsor, Ontario, Canada

2017

©2017, Christopher DiLoreto

Quantum Control of Open Systems and Dense Atomic Ensembles

by

Christopher DiLoreto

APPROVED BY:

M. Spanner, External Examiner

University of Ottawa

J. Gauld

Department of Chemistry

E.H. Kim

Department of Physics

G.W.F. Drake

Department of Physics

C. Rangan, Advisor

Department of Physics

April 25, 2017

Declaration of Previous Publication

This thesis includes an original paper that has been previously published/submitted for publication in peer reviewed journals, as follows:

Thesis Chapter	Publication title/full citation	Publication status
Chapter 3	C.S. DiLoreto and C. Rangan. Polarization control of spontaneous emission for rapid quantum-state initialization. <i>Phys. Rev. A</i> , 95:043834, 2017.	Published

I certify that I have obtained a written permission from the copyright owner(s) to include the above published material(s) in my thesis. I certify that the above material describes work completed during my registration as a graduate student at the University of Windsor.

I declare that, to the best of my knowledge, my thesis does not infringe upon anyones copyright nor violate any proprietary rights and that any ideas, techniques, quotations, or any other material from the work of other people included in my thesis, published or otherwise, are fully acknowledged in accordance with the standard referencing practices. Furthermore, to the extent that I have included copyrighted material that surpasses the bounds of fair dealing within the meaning of the Canada Copyright Act, I certify that I have obtained a written permission from the copyright owner(s) to include such material(s) in my thesis. I declare that this is a true copy of my thesis, including any final revisions, as approved by my thesis committee and the Graduate Studies office, and that this thesis has not been submitted for a higher degree to any other University or Institution.

Abstract

Controlling the dynamics of open quantum systems; i.e. quantum systems that decohere because of interactions with the environment, is an active area of research with many applications in quantum optics and quantum computation. My thesis expands the scope of this inquiry by seeking to control open systems in proximity to an additional system. The latter could be a classical system such as metal nanoparticles, or a quantum system such as a cluster of similar atoms. By modelling the interactions between the systems, we are able to expand the accessible state space of the quantum system in question.

For a single, three-level quantum system, I examine isolated systems that have only normal spontaneous emission. I then show that intensity-intensity correlation spectra, which depend directly on the density matrix of the system, can be used to detect whether transitions share a common energy level. This detection is possible due to the presence of quantum interference effects between two transitions if they are connected. This effect allows one to assess energy level structure diagrams in complex atoms/molecules.

By placing an open quantum system near a nanoparticle dimer, I show that the spontaneous emission rate of the system can be changed “on demand” by changing the polarization of an incident, driving field. In a three-level, Λ system, this allows a qubit to both retain high qubit fidelity when it is operating, and to be rapidly initialized to a pure state once it is rendered unusable by decoherence. This type of behaviour is not possible in a single open quantum system; therefore adding a classical system nearby extends the overall control space of the quantum system.

An open quantum system near identical neighbours in a dense ensemble is another example of how the accessible state space can be expanded. I show that a

dense ensemble of atoms rapidly becomes disordered with states that are not directly excited by an incident field becoming significantly populated. This effect motivates the need for using multi-directional basis sets in theoretical analysis of dense quantum systems. My results demonstrate the shortcomings of short-pulse techniques used in many recent studies.

Based on my numerical studies, I hypothesize that the dense ensemble can be modelled by an effective single quantum system that has a decoherence rate that changes over time. My effective single particle model provides a way in which computational time can be reduced, and also a model in which the underlying physical processes involved in the system's evolution are much easier to understand. I then use this model to provide an elegant theoretical explanation for an unusual experimental result called "transverse optical magnetism". My effective single particle model's predictions match very well with experimental data.

Acknowledgements

I would to take a brief moment to thank all the people who helped me complete this in some way. Firstly I would like to thank Dr. Chitra Rangan, my advisor, for making this project possible and for providing me with the majority of feedback I needed to complete it. Secondly I would like to thank my friends and family for their moral support. Thirdly I would like to thank the people I had the pleasure to work with; my advisory committee, fellow TAs, Sharcnet and UWindsor support staff and members of the Rangan group.

Contents

Declaration of Previous Publication	iii
Abstract	iv
Acknowledgements	vi
List of Figures	xi
Glossary Of Symbols	xxi
1 Introduction	1
1.1 Dissertation Overview	2
1.1.1 Control of a Single, Open Quantum System	3
1.1.2 Control of an Open Quantum System Interacting with a Nearby Classical System	4
1.1.3 Evolution of Dense Quantum Ensembles	5
1.1.4 Effective Single Particle Model of the Evolution of a Dense Quantum Ensemble	7
1.1.5 Appendices	8
2 Control of an Individual, Open Quantum System	9
2.1 Spectroscopic Detection of Couplings Between State Transitions . . .	9
2.2 Theoretical Model	11

2.3	Effect of Detuning on the Correlation Spectrum	15
2.4	Effect of Spontaneous Emission on the Correlation Spectrum	19
2.5	Effect of Dephasing on the Correlation Spectrum	20
2.6	Potential Application of this Method	21
2.7	Summary	23
3	Quantum Behaviour with a Classical Environment	24
3.1	Motivation - Improving Qubit Preparation/Cooling Times	24
3.1.1	Description of a Classical Environment	26
3.1.2	Effect of a Noble-Metal Nanoparticle on a Quantum System	26
3.2	Theoretical Methodology	28
3.2.1	Electromagnetic Field Propagation	28
3.2.2	Electromagnetic Field Enhancement Around a Silver Nanoparticle	29
3.2.3	Decay Rate Enhancement Around a Ag Nanoparticle	30
3.3	Control of a Quantum System between two Silver Nanoparticles	33
3.4	Summary	42
4	Quantum Behaviour in Dense Ensembles	43
4.1	Theory and Implementation	45
4.1.1	Evolution of the Electromagnetic Field and the Quantum State	45
4.1.2	Generalized Directional State Basis	46
4.1.3	Mean-field Environmental Interaction	47
4.1.4	Electromagnetic Field Generation From Quantum Elements	49
4.1.5	Summary of Evolution Methodology	50
4.2	Spectrum of the Electric Field Outside a Driven Nanosphere	51
4.3	Disorder and Directional State Leakage in Dense Quantum Ensembles	53
4.3.1	Effect of Increasing Ensemble Density	57

4.3.2	Effect of Changing the Incident Field Frequency	57
4.3.3	Consequences of the Onset of the Disordered State	57
4.3.4	Quantifying Disorder and Directional State Leakage in Dense Quantum Systems	67
4.4	Summary	71
5	Modelling Dense Ensemble Dynamics with Single Particle Tech- niques	74
5.1	Dense Ensemble Quantum Control with Single Particle Dynamic De- coherence	75
5.2	Pulsed Excitations in Dense Quantum Systems and Magnetic-Dipole Scattering	83
5.2.1	Case: Decoherence Rates are Independent of State Populations	86
5.2.2	Case: Decoherence Rates are Modified by Excited State Popu- lations	87
5.3	Summary	90
6	Conclusion	92
6.1	Summary of Original Contributions	95
6.2	Future Directions	97
A	Rotating-Wave Approximation Hamiltonian	99
A.1	RWA for Optically-Linked Chains of States Using an Intuitive Repre- sentation	100
A.1.1	Two-level System	101
A.1.2	Three-level System	103
A.1.3	Degenerate Five-level W System	104
B	Scaling Parameters	105

B.1	Number Density	106
C	Steady State Solutions to the Master Equation	107
C.1	Steady State Conditions of a Two-Level System	108
C.2	Preparation Limitations of Two-level Quantum Systems	109
C.2.1	Purity of a Two-level System in a Steady-State	114
C.3	Preparing Pure States in a Three-level Lambda System with Decay Enhancement	115
D	Lorentz-Lorenz Shift	118
D.1	Classical Evaluation	118
E	Pseudo-Spectral Time Domain	121
E.1	Evolution of the Fields	121
E.1.1	PSTD Stability	129
E.1.2	Introduction of the Source	130
E.1.3	Parallel Implementation	131
F	Ensemble fitting parameters	133
	Bibliography	136
	Vita Auctoris	150

List of Figures

2.1	Schematic of the model three-level Λ system. The two transitions of the Λ are driven by the fields with Rabi frequencies Ω_0 and Ω_2 respectively.. The detuning of the incident field from each of the transitions (Δ_0 and Δ_1) are not equal in general.	12
2.2	Intensity-intensity correlation spectra for varying values of detuning Δ_1 with $\Omega_0 = \Omega_2 = \Omega$. The detuning Δ_0 is kept fixed at a value of 1.0Ω . The spontaneous decay rate from the excited state is low with $\gamma/\Omega = 0.01$	17
2.3	Intensity-intensity correlation spectra of a fluorescent transition in a Λ system for various values of Δ_1 for $\Delta_0 = 0$. Both transitions are driven by the same Rabi frequency Ω . The rate of spontaneous decay is low with $\gamma \ll \Omega$	18
2.4	Intensity-intensity correlation spectra for increasing amounts of spontaneous decay γ with fixed detuning $\Delta_1 = \frac{\Omega}{2}$, and $\Delta_0 = 0$. As the rate of spontaneous decay increases, the peaks broaden and become less distinguishable.	20
2.5	Intensity-intensity correlation spectra for increasing amounts of dephasing $\delta_d = \delta_0 = \delta_2$ with fixed detuning $\Delta_1 = \frac{\Omega}{2}$, and $\Delta_0 = 0$ as well as fixed spontaneous decay ($\gamma = 0.01\Omega$) . As the rate of spontaneous decay increases, the peaks broaden and become less distinguishable.	21

3.1 An xy plot of electric field intensities ($|E|$ at 475 nm) for a \hat{y} polarizaed wave travelling in the \hat{z} direction around a 20 nm Ag nanoparticle. 30

3.2 A plot of electric field intensity enhancement ($|E|/E_0$) as a function of wavelength for a \hat{y} polarized wave travelling in the \hat{z} direction at distance of 10 nm from the surface of a spherical Ag nanoparticle or radius r 31

3.3 (a) Field enhancements ($M_{E,i} = |E_i|/E_0$) and (b) decay rate modification ($M_d = \gamma/\gamma_0$) of the quantum emitter placed halfway in between two silver NPs with $r = 20$ nm and $d = 12nm$ surface-to-surface separation for two different incident polarizations. The blue, solid (red, dashed) curves corresponds to when the incident field is perpendicular (parallel) to the interparticle axis. The two solid vertical lines in (b) correspond to the maximum decay rate enhancement for the \hat{x} orientation (370 nm) and the largest relative ratio of decay rate enhancement, \hat{x}/\hat{z} (≈ 420 nm). 36

3.4 Polarization control scheme for rapid qubit initialization. Two applied fields near resonant with the $|g\rangle - |e\rangle$ and $|c\rangle - |e\rangle$ transitions are linearly polarized in the $x - z$ plane. The z components of the field excite the blue (solid) transitions, while the x components of the field excite the red (dashed) transitions. For preparation, the Rabi frequencies of all transitions are high with respect to spontaneous decay rates. The spontaneous emission rates of the operational (blue, solid) transitions, $\gamma_{ge,z}$ and $\gamma_{ce,z}$, stay low, whereas those of the preparation transitions (red, dashed), $\gamma_{ge,x}$, and $\gamma_{ce,x}$, are greatly enhanced. The detunings are chosen to coherently trap the system in a dark state. 39

- 3.5 The time required to reach a final, pure state is plotted with respect to the ratio of spontaneous decay rates ($\gamma_{ge,x}/\gamma_{ge,z} = \gamma_{ce,x}/\gamma_{ce,z}$) for various driving field strengths. The effective five level system is initially driven from an operational, completely mixed state ($\rho_{gg} = \rho_{(e,0)(e,0)} = \rho_{cc} = \frac{1}{3}$). The calculation parameters are $\Omega_{ce,x} = \Omega_{ge,x} = \Omega_{ce,z} = \Omega_{ge,z}$, $\gamma_{ge,x} = \gamma_{ce,x} = \gamma_{e,x}$ and $\gamma_{ge,z} = \gamma_{ce,z} = \gamma_{e,z}$. The preparation time is normalized to the time taken for an equivalent three-level λ system to reach a steady state. 41
- 4.1 a) When the polarization of an electromagnetic field sets the quantization axis of an atom, the effective quantum system is a two-level system with the direction of the transition dipole oriented along that polarization direction. b) When the polarization of an incident control field is different from the quantization axis, the effective quantum system is a four-level system with a dipole transition oriented along each field component. 48
- 4.2 Electric field spectra for different time windows outside a 10 nm radius nanosphere of atoms with on-resonant excitation located at a spatial position $y=3$ nm outside the nanosphere. Surface plasmons are created by illumination with a monochromatic field of $f=2.41 \times 10^{14}$ Hz and $E = 1.5 \times 10^9$ V/m. The system has degenerate energy level spacings in the x, y and z direction of 1 eV and a number density of 4×10^{27} atoms per cubic metre. (a) Frequency components that appear in the time window 0 - 200fs after the start of excitation. (b) Frequency components that appear in the time window 100 - 300fs after the start of excitation. Notice that the blue-shifted frequency components die out. 52

4.3 Snapshots of \hat{y} and \hat{x} direction free currents (in A/m^2) showing the ordered and disordered phases in both the incident field polarization direction (a, b, c - \hat{y}) and a non-principle direction (d, e, f - \hat{x}) in a 10 nm nanosphere of atoms at times (a/d) 10 fs, (b/e) 100 fs and (c/f) 250 fs. Populations are evaluated using a 1 nm grid and are illuminated with a constant field intensity of $E=1.5 \times 10^9$ V/m. The system has degenerate energy level spacings in the x, y and z direction of 1 eV and a number density of 4×10^{27} atoms per cubic metre. The beam is polarized in the \hat{z} direction and the snapshot bisects the nanosphere in the xy plane. 55

4.4 Schematic of different regimes in the evolution of a dense quantum ensemble excited principally along the \hat{y} direction. (a) In the short time regimes, the ensemble behaves in a similar fashion to a single quantum element - all individual components are in phase and display a uniform oscillation. (b) Entropy is introduced to the system, transitioning it from a uniform ordered phase to a disordered phase with multi-directional excited states. (c) This system is in a disordered phase and has all directional states excited to some degree. In this phase it operates in a similar fashion to a classical discrete dipole system as the coherent oscillations are suppressed by directional state leakage. 56

4.5 Spatially averaged excited state populations in the \hat{x} , \hat{y} and \hat{z} directions for a 10 nm radius nanosphere of atoms with various number densities. Populations are evaluated using a 1 nm grid and are illuminated with a constant field intensity of $E=1.5 \times 10^9$ V/m. The system has degenerate energy level spacings in the x, y and z direction of 1 eV. 58

4.5	Spatially averaged excited state populations in the \hat{x} , \hat{y} and \hat{z} directions for a 10 nm radius nanosphere of atoms with various number densities. Populations are evaluated using a 1 nm grid and are illuminated with a constant field intensity of $E=1.5 \times 10^9$ V/m. The system has degenerate energy level spacings in the x, y and z direction of 1 eV.	59
4.5	Spatially averaged excited state populations in the \hat{x} , \hat{y} and \hat{z} directions for a 10 nm radius nanosphere of atoms with various number densities. Populations are evaluated using a 1 nm grid and are illuminated with a constant field intensity of $E=1.5 \times 10^9$ V/m. The system has degenerate energy level spacings in the x, y and z direction of 1 eV.	60
4.6	Spatially averaged excited state populations in the \hat{x} , \hat{y} and \hat{z} directions for a 10 nm radius nanosphere of atoms with lower energy off-resonant excitation. Populations are evaluated using a 1 nm grid and are illuminated with a constant field intensity of $E=1.5 \times 10^9$ V/m. The system has degenerate energy level spacings in the x, y and z direction of 1 eV and a number density of 5×10^{27} atoms per cubic metre.	61
4.6	Spatially averaged excited state populations in the \hat{x} , \hat{y} and \hat{z} directions for a 10 nm radius nanosphere of atoms with lower energy off-resonant excitation. Populations are evaluated using a 1 nm grid and are illuminated with a constant field intensity of $E=1.5 \times 10^9$ V/m. The system has degenerate energy level spacings in the x, y and z direction of 1 eV and a number density of 5×10^{27} atoms per cubic metre.	62

4.6	Spatially averaged excited state populations in the \hat{x} , \hat{y} and \hat{z} directions for a 10 nm radius nanosphere of atoms with lower energy off-resonant excitation. Populations are evaluated using a 1 nm grid and are illuminated with a constant field intensity of $E=1.5 \times 10^9$ V/m. The system has degenerate energy level spacings in the x, y and z direction of 1 eV and a number density of 5×10^{27} atoms per cubic metre.	63
4.7	Spatially averaged excited state populations in the \hat{x} , \hat{y} and \hat{z} directions for a 10 nm radius nanosphere of atoms with higher energy off-resonant excitation. Populations are evaluated using a 1 nm grid and are illuminated with a constant field intensity of $E=1.5 \times 10^9$ V/m. The system has degenerate energy level spacings in the x, y and z direction of 1 eV and a number density of 5×10^{27} atoms per cubic metre.	64
4.7	Spatially averaged excited state populations in the \hat{x} , \hat{y} and \hat{z} directions for a 10 nm radius nanosphere of atoms with higher energy off-resonant excitation. Populations are evaluated using a 1 nm grid and are illuminated with a constant field intensity of $E=1.5 \times 10^9$ V/m. The system has degenerate energy level spacings in the x, y and z direction of 1 eV and a number density of 5×10^{27} atoms per cubic metre.	65
4.7	Spatially averaged excited state populations in the \hat{x} , \hat{y} and \hat{z} directions for a 10 nm radius nanosphere of atoms with higher energy off-resonant excitation. Populations are evaluated using a 1 nm grid and are illuminated with a constant field intensity of $E=1.5 \times 10^9$ V/m. The system has degenerate energy level spacings in the x, y and z direction of 1 eV and a number density of 5×10^{27} atoms per cubic metre.	66

4.8	Effective ensemble decay rates (γ_{ens}) for a 10 nm radius nanosphere of atoms with varying number density (N_a). Populations are evaluated using a 1 nm grid and are illuminated with a constant field intensity of $E=1.5 \times 10^9$ V/m. The system has degenerate energy level spacings in the x, y and z direction of 1 eV. The base decay rate for the individual quantum systems is $2.6 \times 10^6 s^{-1}$	70
4.9	Effective ensemble decay rates (γ_{ens}) for a 10 nm radius nanosphere of atoms with varying number density (N_a). Populations are evaluated using a 1 nm grid and are illuminated with a constant field intensity of $E=7.5 \times 10^8$ V/m. The system has degenerate energy level spacings in the x, y and z direction of 1 eV. The base decay rate for the individual quantum systems is $2.6 \times 10^6 s^{-1}$ and a logistic function is fit to the data.	72
5.1	When significant dipole-dipole interactions are present in an ensemble system, it becomes possible for spontaneous emission from one excited state to excite state population from the ground state to another excited state. This allows for “spontaneous-emission” to occur between optically forbidden transitions using emission followed by absorption (δ 's in green). This results in a modified Lindblad decay scheme when examining ensemble populations. δ_{xx} , δ_{yy} and δ_{zz} reflect “parallel” transitions, whereas δ_{xy} , δ_{yz} , and δ_{zx} reflect “perpendicular” transitions. These dephasing rates do not affect the total state population, it only reduces the overall coherence of the ensemble state.	77

5.2 Spatially averaged excited state populations for a 10 nm radius nanosphere of atoms. Populations are evaluated using a 1 nm grid and are illuminated with a constant field intensity of $E=1.5 \times 10^9$ V/m. The system has degenerate energy level spacings in the x, y and z direction of 1 eV and a number density of 4×10^{27} atoms per cubic metre. A single particle calculation in the RWA approximation is overlaid to compare the two models. 81

5.3 Spatially averaged excited state populations for a 10 nm radius nanosphere of atoms. Populations are evaluated using a 1 nm grid and are illuminated with a constant field intensity of $E = 1.5 \times 10^9$ V/m. The system has degenerate energy level spacings in the x, y and z direction of 1 eV and a number density of 2.5×10^{27} atoms per cubic metre. A single particle calculation in the RWA approximation is overlaid to compare the two models. 82

5.4 Full Ensemble Calculation: Spatially averaged excited state populations for a 10 nm radius nanosphere of an atoms with various number densities. Populations are evaluated using a 1 nm grid and are illuminated with a 20 fs width Gaussian pulse. The system has degenerate energy level spacings of 1 eV and a number density of 1×10^{27} atoms per cubic metre. 85

5.5 Excited state populations for a Lindblad dissipation evolution scheme with decay coupling parameters found by examining state evolution in Fig 5.4. The system evolves from an almost pure excited state and spontaneous emission from this state is able to excite other transitions. For this case coupling parameters are assumed to be constant. 88

5.6	Excited state populations for a Lindblad dissipation evolution scheme with decay coupling parameters found by examining state evolution in Fig 5.4. The system evolves from an almost pure excited state and spontaneous emission from this state is able to excite other transitions. For this case, coupling parameters follow the dependence on the density matrix outlined in Section 5.1.	89
A.1	Pictorial representation of the process of determining the unitary transformation matrix in a 5 level chain. (A) Each transition connects two levels and all edges oscillate at some fast frequency (this oscillation is represented by a circle). A reference level ($ 3\rangle$) is chosen and U_{ref} is applied. (b) With $ 3\rangle$ serving as a reference level (indicated by diagonal lines under the energy level), the nearest left ($ 3\rangle \rightarrow 2\rangle$) and right ($ 3\rangle \rightarrow 4\rangle$) transitions are selected for minimization using rotation R^0 . (c) The previous rotation, R^0 which affects all nodes to the left (blue arrow) and to the right (green arrow) removes the oscillation in $ 3\rangle \rightarrow 2\rangle$ and $ 3\rangle \rightarrow 4\rangle$. The next nearest left ($ 2\rangle \rightarrow 1\rangle$) and right ($ 4\rangle \rightarrow 5\rangle$) transitions are then selected for minimization using rotation R^1 . (d) Applying R^1 (orange/red arrows) minimizes all rotations and the process is complete.	102
C.1	Ground state populations and coherences of the qubit with $\gamma = 2.81 \times 10^{10} s^{-1}$ and $\Delta = 1.37 \times 10^{14} s^{-1}$ is evolved from a variety of initial conditions to reach the desired state populations $\rho_{gg} = 0.75$ and $\rho_{ee} = 0.25$	112
C.2	Purity of the qubit, with $\gamma = 2.81 \times 10^{10} s^{-1}$ and $\Delta = 1.37 \times 10^{14} s^{-1}$, when it is evolved from a variety of initial conditions to reach the desired state populations $\rho_{gg} = 0.75$ and $\rho_{ee} = 0.25$	113

C.3	The time required to reach a steady state in a three-level lambda system, normalized to the case in which one decay rate is negligible when compared to the other, is plotted versus various ratios of decay rates.	117
E.1	Parallel scheme for performing the PSTD calculation; coarse-grain lattice cells are arranged and split amongst cores according to the x-position. At each lattice-cell centre, electric fields and density matrices are tracked in real-time and updated.	132

Glossary of Symbols

Parameter	Symbol	Description	Formula/Value
Energy Level	E_n	Energy level of a given state	N/A
Transition Frequency	ω_{nm}	Frequency corresponding to the energy level separation between levels n and m	$\frac{E_n - E_m}{\hbar}$
Field Frequency	ω_k	Frequency corresponding to an incident field frequency	N/A
Incident Electric Field Amplitude	E	Amplitude corresponding to an incident electric field	N/A
Local Electric Field	$\mathbf{E}(\mathbf{r}, t)$	Positional electric field	N/A
Local Magnetic Field	$\mathbf{B}(\mathbf{r}, t)$	Positional magnetic field	N/A
Dipole moment	μ_{mn}	Dipole moment of a specific amount transition dipole between levels n and m	$\approx (0.1 \text{ nm}) e$
Rabi Frequency	Ω_{nm}	Rabi frequency corresponding to the transition between level n and m	$\Omega_{nm} = \frac{\mu_{mn} \cdot \mathbf{E}(t)}{\hbar}$
Spontaneous Decay Rate	γ_{nm}	Rate corresponding to the decay of $ n\rangle \rightarrow m\rangle$	N/A

Parameter	Symbol	Description	Formula/Value
Dephasing Rate	δ_{mm}	Rate corresponding to the dephasing in the transition with upper level $ m\rangle$	N/A
Detuning	Δ_k	Frequency corresponding to the difference between an incident field frequency and the transition frequency	$\Delta_k = \omega_{nm} - \omega_k$
Number Density	N_a	Number of atoms per unit volume	N/A

Chapter 1

Introduction

Controlling the dynamics of quantum systems (quantum control [1, 2, 3]) is essential for various applications such as coherently populating specific atomic or molecular eigenstates [4], causing atomic gases to become selectively transparent to specific wavelengths of light [5] and performing computational logic operations on groups of atoms [6, 7]. In all of these applications, the quantum system has a negligible or constant interaction with its environment. The overall effects of these external interactions can be modelled by one or more constant decoherence rates (γ) [8]. In theoretical calculations, the assumption that the environmental interaction is negligible or constant greatly simplifies the complexity of a system and how to control its behaviour. In this work, I explore the effects of time-dependent decoherence rates, with these we can extend the overall quantum control space, and find novel ways to exploit decoherence-dependent processes.

As the behaviour of any quantum system is often considered to be entirely dependent on its instantaneous state (the Markovian assumption [9]), the quantum dynamics of the system, including environmental interactions, must depend on the eigenstates of the Hamiltonian, and their superposition. Therefore, the dynamics of the quantum system must be investigated in the time-domain since the state of the

system and that of the environment change over time [10, 11, 12]. This is particularly important when the interaction with the environment is time-dependent. The time-dependent environmental interaction increases the overall number of possible process “knobs” that we can use for quantum control.

Coherent control of quantum systems is typically applied through the use of precise, pulsed-laser excitations which can drive specific transitions, and change the state of the system from one superposition of eigenstates to another [13, 14]. By properly timing and shaping these laser excitations, the system can ideally be driven to almost any state desired [15, 16].

There are, however, many factors that can affect how atoms respond to external stimuli, which complicates this external form of control. This is true in both aggregate and individual systems; these systems can have multiple quantum transitions connected by shared levels, and these transitions do not respond independently of one another [17, 18, 19]. In these types of systems, purely quantum effects arise due to the interference between different transitions. This requires us to apply control techniques to a system as a whole, as opposed to viewing the system as a series of independent transitions [20].

1.1 Dissertation Overview

The control of a quantum system is a vast area of research in the field of quantum control [12, 21]. In this dissertation, I present the results from a series of theoretical investigations on the control of several classes of quantum systems, wherein quantum systems undergo laser-excitation in the presence of decoherence and dissipation. These investigations have been organized into four main sections based on increasing complexity in the type of environmental interaction influencing the evolution of the quantum systems.

- Firstly, I look at the control of a single open quantum system with negligible or constant environmental interactions.
- Secondly, I look an open quantum system that interacts with a nearby classical system. The quantum system’s environment is spatially non-uniform; however, the environment does not have an explicit time-dependence.
- Thirdly, I examine a quantum system interacting with a number of identical quantum systems. The environment of a single one in the ensemble is fully quantum mechanical in nature. In this case, the decoherence rates of a single system could be time-dependent.
- Lastly, I propose a model for evaluating the behaviour of a dense ensemble of quantum systems using single-particle techniques. This model is significantly faster to implement computationally than the multi-particle model, and provides a greater understanding of the underlying physics involved. I then use this model to provide a simple explanation for an unusual experimental effect.

1.1.1 Control of a Single, Open Quantum System

In Chapter 2, I investigate an open quantum system exposed to an incident electromagnetic field. In these systems, quantum interference effects occur between connected transitions and complicated the evolution of the system’s state. These interference effects have been both theoretically predicted and measured [22, 23, 24, 25, 26]; however, they have largely been used with the “two-photon resonance” condition to show effects such as correlated and anti-correlated spectra in pairs of transitions.

By extending past this resonance condition and by modelling the system’s state evolution in time, I show that small changes in the detuning of pairs of quantum transitions can be used to easily determine the connectivity of these transitions in the overall quantum system. I predict that by experimentally measuring the two-time

intensity-intensity correlation function [27] as a function of the detuning of a single quantum transition, one can detect the presence of connected transitions. This serves as a simple, direct way of confirming energy level diagrams in complex systems. In addition, this method could also be used to track real-time changes in state energy-levels due to ambient interactions.

1.1.2 Control of an Open Quantum System Interacting with a Nearby Classical System

In Chapter 3, I investigate how the asymmetric enhancement of the decoherence rate of a quantum system can be used to increase the usable “uptime” of quantum information systems by reducing the required “cooling” time in which the system is allowed to spontaneously decay back down to the ground state. This rapid state initialization is another of the main requirements for the practical implementation of quantum computers [28]; however it is largely neglected due to the greater difficulty in obtaining qubits with long lifetimes. As such, my improvement scheme presents a significant advance over typical qubit enhancement schemes [29, 30, 31, 32, 33] which all attempt to reduce the overall decoherence of the system.

Practically, this asymmetric decoherence enhancement is obtained when the quantum system (such as an atom or molecule) is placed next to a metal nanoparticle dimer. This dimer is a nano-scale plasmonic system that is capable of greatly enhancing local fields and spontaneous decay rates [34, 35]. Metal nanoparticle dimers are highly ‘tunable’ in the sense that the wavelengths of light that they enhance can be changed by changing the size and spacing between the particles in the dimer [36]. For this system, the dimer structure creates a directionally-asymmetric, decoherence rate enhancement for a proximate radiating dipole. This asymmetry makes it possible to change the decoherence rate of the system by changing the polarization of the driving electromagnetic fields. This allows field-polarization to become a control pa-

parameter. Using this effect, I have proposed a novel way of changing the spontaneous emission of a system “on demand”. The field-polarization can also affect the purity of the quantum system, which is a useful metric that serves as an indicator of qubit quality [30].

For this investigation, I have left the choice of quantum system general to allow for experimental freedom. These solid state quantum systems could take the form of semiconducting quantum dots [37, 38, 39], or Josephson junctions [40, 41]. Although we have used a nanoparticle, the nearby classical system could be also be a cavity [42, 43, 44, 45] or photonic crystal [46] as long as the system is capable of asymmetrically enhancing a quantum system’s spontaneous emission rate.

1.1.3 Evolution of Dense Quantum Ensembles

In Chapter 4, I examine the control of systems in which the behaviour of a quantum system depends on its environment, which can also be a quantum system. Developing techniques for evaluating the quantum response of nanoscale systems has become an important, recent area of investigation as quantum-based optical effects allow for the design of systems with unique properties [47, 48, 49].

Recent large-scale simulations for low-intensity systems have shown that inter-atomic interactions can induce transparency [48], shift resonance absorptions unusually in cold dense gases [50, 51], modify spontaneous emission rates [52] and decoherence rates [53] and overall scattering processes [54, 55]. However, as these simulations all occur at low-intensity, they largely neglect the overall evolution of the systems quantum state and may not be able to accurately capture spontaneous emission based effects or inelastic scattering [47]. In addition a number of these studies use approximations, such as short pulse-methods [55, 49] and quantum basis sets that only excites along a single field polarization direction [48, 49], which I show, are not universally applicable for systems that are strongly driven and/or have high amounts

of decoherence.

As such, I investigated the quantum optical response of nanoscale quantum systems to more intense incident fields, longer timescales and with a multi-directional state basis. The study of this type of system requires the implementation of a new methodology in which quantum evolution and electromagnetic field propagation are solved concurrently. This type of investigation allows for the direct testing of computational assumptions that are typically used in the literature.

This work was also motivated by the potential application of dense quantum systems to enhancing the response of solar cells to solar radiation. This would take advantage of a strong, coherent Lorentz-Lorenz shift [56] to increase the absorption of incident infra-red radiation around quantum nanostructures. The interactions with nanostructures would change the energy of these infra-red photons to above the bandgap of silicon and allow them to produce photoelectrons. A preliminary calculation was promising; however the effect decoheres rapidly (≈ 200 fs) and becomes unusable for solar cell applications. This strong decoherence rate in dense collections of quantum systems motivated my more in-depth theoretical study of how dense collections of quantum systems behave under a control field.

Firstly, my analysis shows that the use of restricted, uni-directional basis sets [48] can lead to incorrect models of the behaviour of dense atomic systems under external fields. These models do not take into account the “leakage” of state population into states not directly excited by the control field. My analysis uses three-directional basis sets, which allows this leakage to be observed. I have used this analysis to provide a method for determining the rate of this leakage effect by observing an order-disorder transition. Without higher-directional basis sets, the leakage effect is intrinsically neglected, and the accuracy of the theoretical model is reduced. This requirement for high-directional basis sets is similar to how Ising models in statistical mechanics have phase transitions that scale quite differently in higher dimensions [57, 58].

Secondly, my analysis indicates that the “short-pulse” method (using a fs pulse to approximate continuous scattering amplitudes) used in classical electrodynamics calculations [59, 47] of scattering does not translate to applications involving dense collections of quantum emitters. Since these dense systems appear to develop a very strong decoherence rate, the “short-pulse” method greatly overestimates the effects of coherent scattering in these systems.

1.1.4 Effective Single Particle Model of the Evolution of a Dense Quantum Ensemble

In Chapter 5, I use my investigations into the dynamics of a dense collection of quantum emitters to suggest that a single quantum system model with modified decoherence terms could be used to approximate the behaviour of the dense ensemble. In this model, the decoherence rates are dynamic (i.e. they change over time) since they depend on the ensemble state of the quantum system itself (as opposed to depending on only the environment). This simplified model allows the computational time of simulations to be greatly reduced, and it allows the underlying physical processes to be more clearly understood. This is useful as it allows for the rapid prediction of quantum-based optical effects in strongly-driven, dense systems which can allow for the design of systems with unique optical properties.

In addition, this model provides a theoretical explanation for an unusual experimental result called “transverse optical magnetism” [60, 61, 62]. In these experiments, a strong ultrafast pulse is scattered off a liquid (such as H_2O , CCl_4), and the transverse scattered light is observed to have rotated polarization. The theoretical explanation provided by the experimentalists [60, 61, 62] is controversial, and there is debate as to the origin of this effect [63, 64, 65, 66, 67]. My analysis, incorporating state leakage and molecular interactions, provides a simple and elegant model that reproduces the features of the experiment. This analysis also explains why this effect

is only seen in pulsed excitations with high intensities [60].

1.1.5 Appendices

In order to increase the clarity and readability of this thesis, the majority of details of standard techniques and technical implementations have been moved to the Appendices.

Chapter 2

Control of an Individual, Open Quantum System

At the simplest level, individual quantum systems can be studied based on their interaction with incident, external fields. This is done by assessing how the applied fields appear in the system's Hamiltonian and by accounting for any inherent decoherence present in the system. In order to do this, I will be operating under the assumption that the incident fields perturb the quantum system.

2.1 Spectroscopic Detection of Couplings Between State Transitions

Spectroscopic methods are frequently used to experimentally determine energy level spacings and detect changes in them. However, simple spectroscopic measurements typically monitor the behaviour of transitions individually, and therefore cannot provide a complete picture of the energy level structure of the system in question. However, it is possible to use more complex spectroscopic methods to provide a more complete picture of the system's quantum structure by searching for quantum inter-

ference in Rabi frequencies between pairs of transitions. As these effects only appear if a pair of transitions share a common energy level, these effects can be used to detect coupled transitions. This allows for the direct construction of energy level diagrams without requiring any previous information about the quantum system's inherent properties and therefore could be useful in analyzing complex atoms/molecules. It also serves as a simple, direct way of confirming energy level diagrams in complex systems.

In Ref. [68], Huang *et al.* have shown that in zero-detuned (resonantly excited) systems, correlation spectra reflect fundamental quantum characteristics such as the amount of spontaneous decay. Other calculations and experiments [22, 23, 24, 25, 26] have used the “two-photon resonance” condition, where the detunings of both transitions are equal, to show effects such as correlated and anti-correlated spectra. In this chapter, I calculate the two-time intensity-intensity correlation spectrum from a driven three-level quantum system in the Λ configuration as a function of changes in the detuning of *both* transitions. I show that quantum interference effects and energy level changes in a three-level fluorescent atom/molecule can be directly detected by monitoring the two-time intensity-intensity correlation spectrum of the molecule when driven by an electromagnetic field since this correlation is directly reflective of state populations [68].

The theoretical model is described in Section 2.2. In Section 2.3, I analytically show that for a three-level system where the two detunings are not equal, and if the decay rate is small relative to the Rabi frequency, the two-time intensity-intensity correlation spectrum shows a three-peaked structure. I also provide a general method and specific examples of how this can be predicted both numerically and analytically.

Changes in the detunings cause significant and quantifiable changes to the location of the spectral peaks and this only appears when the transitions share a common level and interfere. This suggests a spectroscopic protocol for detecting the connec-

tivity of energy level transitions in complex atoms. This method shares similarities with Raman scattering in that it examines light emission from molecular transitions that may not be directly excited by photons of the same wavelength. However, unlike Raman scattering, this correlation spectrum measures only the time-dependent intensity of photons being emitted from a particular transition.

In Sections 2.4 and 2.5, I use numerical calculations to show that for experimental conditions in typical quantum optics studies [69], where one transition is on resonance and the other detuning is swept through the resonance, the expected three-peaked structure will be degraded by significant decoherence to the point at which only one peak is visible. In Section 2.6, I use this effect to provide experimental limitations that would need to be considered in order to develop this protocol into a practical sensor.

2.2 Theoretical Model

I model the atom/molecule as a three-level quantum system with bare energy eigenstates $|0\rangle$, $|1\rangle$ and $|2\rangle$ as shown in Figure 2.1. This quantum system is driven by electromagnetic waves that excite each transition; they have angular frequency ω_L with amplitudes that vary in time as $E(t) = E_i \cos(\omega_i t)$. I assume that these fields are polarized entirely along the direction of the system's transition dipole. I also assume that the $|0\rangle \rightarrow |2\rangle$ transition is forbidden.

The Hamiltonian of the three-level quantum system, driven by an electromagnetic wave with the field-matter interaction of the system treated in the electric-dipole approximation, is described by $H = H_a + \sum_i \mu_i \cdot \mathbf{E}(t)$, where H_a is the Hamiltonian of a three-level system, μ_i is the transition dipole moment of the transition with ground state $|i\rangle$ and $\mathbf{E}(t)$ is electric field of the wave interacting with the system. By applying the rotating wave approximation (RWA, see Appendix [A]), the matrix form of the

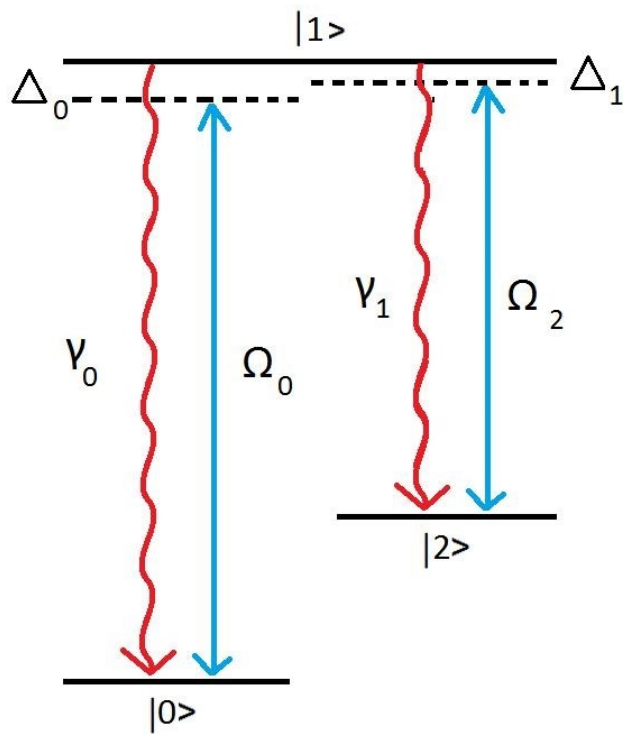


Figure 2.1: Schematic of the model three-level Λ system. The two transitions of the Λ are driven by the fields with Rabi frequencies Ω_0 and Ω_2 respectively.. The detuning of the incident field from each of the transitions (Δ_0 and Δ_1) are not equal in general.

Hamiltonian can be written in the interaction picture as:

$$H_{RWA} = \begin{pmatrix} -\hbar\Delta_0 & \frac{\hbar\Omega_0}{2} & 0 \\ \frac{\hbar\Omega_0}{2} & 0 & \frac{\hbar\Omega_2}{2} \\ 0 & \frac{\hbar\Omega_2}{2} & -\hbar\Delta_1 \end{pmatrix}, \quad (2.1)$$

where Δ_i represents the detuning between the incident field and the state transition frequencies. The Rabi frequency, $\Omega_i = \mu_i E_i$, depends on the amplitude of the incident electric field component parallel (E_i) to the dipole moment of the transition (μ_i).

In order to study the time-dependent response of the system to both the environment and the incident electromagnetic wave, a density matrix representation of the system's state is used. This density matrix ρ_{ij} ($i, j = 0, 1, 2$) evolves in time according to the Lindblad-von Neumann equation which takes the form:

$$\dot{\rho} = -\frac{i}{\hbar}[H_{RWA}, \rho] - L(\rho). \quad (2.2)$$

In this evolution equation, the Lindblad superoperator, $L(\rho)$, models the decoherence in the system. This term is linear in the state density operator and is of the form:

$$L(\rho) = \sum_{d=0,2} \frac{\gamma_d}{2} (\sigma_d^\dagger \sigma_d \rho + \rho \sigma_d^\dagger \sigma_d - 2\sigma_d \rho \sigma_d^\dagger). \quad (2.3)$$

In this equation, σ_d are the Lindblad operators, and I assume that the only decoherence mechanism present is spontaneous emission. γ_d represents the decay or spontaneous emission rate from the excited state to the ground states and therefore $\sigma_0^\dagger = |0\rangle\langle 1|$ and $\sigma_2^\dagger = |2\rangle\langle 1|$. Spontaneous emission between $|0\rangle$ and $|2\rangle$ is not allowed by selection rules.

In the case of general spontaneous emission between levels ($|i\rangle \rightarrow |j\rangle$),

$$\sigma_d = \sigma_{ij} = |j\rangle\langle i|. \quad (2.4)$$

Using this operator, one can evaluate all the terms in the Lindblad superoperator:

$$\sigma_{ij}^\dagger \sigma_{ij} \rho = |i\rangle \langle i| \left[\sum_a \sum_b \rho_{ab} |a\rangle \langle b| \right] = \sum_a \sum_b \rho_{ab} |i\rangle \langle b| \delta_{ia}, \quad (2.5)$$

$$\rho \sigma_{ij}^\dagger \sigma_{ij} = \left[\sum_a \sum_b \rho_{ab} |a\rangle \langle b| \right] |i\rangle \langle i| = \sum_a \sum_b \rho_{ab} |a\rangle \langle i| \delta_{ib}, \quad (2.6)$$

$$\sigma_{ij} \rho \sigma_{ij}^\dagger = |j\rangle \langle i| \left[\sum_a \sum_b \rho_{ab} |a\rangle \langle b| \right] |i\rangle \langle j| = \sum_a \sum_b \rho_{ab} \delta_{ib} \delta_{ia} |j\rangle \langle j|. \quad (2.7)$$

Combining all these terms, one can write down a general expression for matrix element L_{mn} for N total energy levels,

$$\hat{L}_{mn} = \sum_j^N \left(\frac{\gamma_{mj}}{2} + \frac{\gamma_{nj}}{2} \right) \rho_{mn} - 2\delta_{mn} \sum_i^N \frac{\gamma_{in}}{2} \rho_{ii}. \quad (2.8)$$

To determine the fluorescence spectrum, I introduce a two-time correlation function that evaluates the correlation between the intensity being emitted from a transition with lower level $|i\rangle$ at time t , with the intensity being emitted from a transition with lower level $|j\rangle$ at time $t+\tau$. Using the quantum regression theorem [68], this correlation function is expressed in terms of the steady-state populations. A normalized, ensemble-averaged, correlation function is defined [68] as:

$$G_{ij}(\tau) = \frac{\langle : I_i(t) I_j(t+\tau) : \rangle}{\langle |i\rangle \langle i| \rangle \langle |j\rangle \langle j| \rangle}, \quad (2.9)$$

where $\langle : \cdot : \rangle$ denotes time ordering. For the fluorescent transition $|1\rangle \rightarrow |2\rangle$ correlated to itself, this function takes the form [68]:

$$G_{22}(\tau) = \frac{\langle : I_2(t) I_2(t+\tau) : \rangle}{\langle |1\rangle \langle 1| \rangle \langle |1\rangle \langle 1| \rangle} = \frac{P_{2 \rightarrow 1}(\tau)}{P_1}, \quad (2.10)$$

where $P_{2 \rightarrow 1}(\tau)$ represents the matrix element $\rho_{11}(\tau)$ with initial condition $\rho_{22}(\tau = 0) = 1$ and P_1 is the steady state population in $|1\rangle$. Basically, this assumes that at

time t , the system has just emitted a photon from the $|1\rangle \rightarrow |2\rangle$ transition, resulting in $\rho_{22}(\tau = 0) = 1$, and the likelihood of the system to emit another photon in the same transition ($P_{2 \rightarrow 1}(\tau) = \rho_{11}(\tau)$) is tracked. From this correlation function, the correlation spectrum $G_{22}(\omega)$ can be determined via a Fourier transform. The results of these spectra are then scaled to the Rabi frequency [see Appendix B].

2.3 Effect of Detuning on the Correlation Spectrum

When evaluating the time evolution of multi-level quantum systems, the state of the system oscillates with multiple frequencies due to the fact that coupled transitions interfere with one another. Therefore, in order to predict these couplings, one needs to look at the entire matrix interaction. These specific oscillations will only show up if two transitions are coupled by a common energy level.

If the system is in a nearly pure state, these oscillation frequencies can be predicted by looking at the eigenvalues (λ_j) and normalized eigenstates $|\phi_j\rangle$ (dressed states) of the RWA Hamiltonian. This is due to the fact that if the decoherence is low ($\gamma_d \rightarrow 0$) and the state is pure, the density matrix with the wavefunction in the eigenbasis can be expressed as:

$$\rho = |\Psi\rangle\langle\Psi| = \sum_{j,k} c_j c_k^* \exp(-i(\lambda_j - \lambda_k)t/\hbar) |\phi_j(0)\rangle\langle\phi_k(0)|. \quad (2.11)$$

If the RWA Hamiltonian is constant in time, the only possible time-dependent frequencies that can be seen are those that arise from the nonzero differences in the eigenvalues (λ_i) of the RWA Hamiltonian:

$$\omega_{ij} = \sum_{j,k} \frac{(\lambda_j - \lambda_k)}{\hbar}. \quad (2.12)$$

While these are the only frequencies that are possible, it is also possible to not observe these oscillation frequencies if the eigenvector element of $|\phi_j\rangle$ or $|\phi_k\rangle$ is zero. For example if:

$$|\phi_j\rangle = \begin{pmatrix} 0 \\ \frac{1}{\sqrt{2}} \\ \frac{1}{\sqrt{2}} \end{pmatrix}, \quad (2.13)$$

then no Rabi oscillation for frequencies involving λ_j will ever be seen in matrix elements ρ_{0i} or ρ_{i0} due to $|\phi_j\rangle\langle\phi_k|$ having zero amplitude for that density matrix element.

The correlation spectrum of a three-level Λ system that has both transitions on resonance with an incident electromagnetic field will have a single peak observed at $\omega_{\Delta=0} = \sqrt{\Omega_0^2 + \Omega_2^2}$ [68]. This effect is understood by the presence of the zero-energy “dark state” that does not couple to the excited fluorescing level. Thus, the only frequency observed in the correlation spectrum is that of the transition between the other two dressed states of the Hamiltonian. For the same reason, when a three-level Λ system is driven with both transitions at the *same* detuning (the so-called “two-photon resonance condition”), only a single peak will be observed in the correlation spectrum.

When the two detunings are not equal to each other ($\Delta_0 \neq \Delta_1$), there is no dark state in the dressed state picture. Therefore I expect to see three peaks in the correlation spectrum as shown by the numerical calculations in Fig. 2.2. Detuning Δ_0 is kept equal to Ω , while Δ_1 is swept from zero to 2Ω . The three-peaked structure of the correlation spectra changes to a single-peaked structure at the two-photon resonance condition $\Delta_0 = \Delta_1$ in which there is a zero eigenvector element.

For a three-level system with *negligible decay*, the oscillating frequencies of the correlation peaks can be evaluated analytically by finding the eigenvalues of the dressed RWA Hamiltonian:

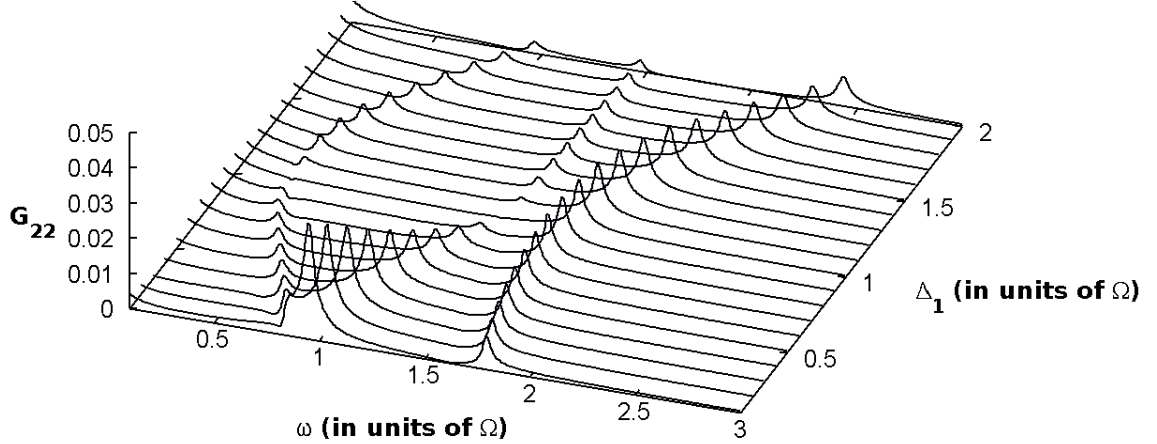


Figure 2.2: Intensity-intensity correlation spectra for varying values of detuning Δ_1 with $\Omega_0 = \Omega_2 = \Omega$. The detuning Δ_0 is kept fixed at a value of 1.0Ω . The spontaneous decay rate from the excited state is low with $\gamma/\Omega = 0.01$.

$$\lambda^3 + (\Delta_0 + \Delta_1)\lambda^2 - \left(\Delta_0 \Delta_1 + \frac{\Omega_0^2}{4} + \frac{\Omega_2^2}{4}\right)\lambda - \frac{1}{4}(\Delta_0\Omega_2^2 + \Delta_1\Omega_0^2) = 0. \quad (2.14)$$

The differences between the eigenvalues of the dressed Hamiltonian determines the location of the peaks in the correlation spectrum. Since the equation is cubic, there are three eigenstates. Transitions between all three pairs of eigenstates are allowed, hence it is possible to observe three peaks if there exists a non-equal detuning of both transitions. In the case of equal detuning, the presence of a dark state (eigenvector with a zero element) prevents the three-peaks from being observed, and only one peak is observed.

The deterministic location of the peaks in the correlation spectra as a function of the two detunings suggests a practical application. If the peak frequencies in the two-time intensity-intensity correlation spectrum are measured, those peak frequencies can be used to infer whether transitions are connected and extract the values of both detunings if one knows the strengths of the Rabi frequencies of each transition.

To illustrate this practical application, I look at a simplified case that assumes

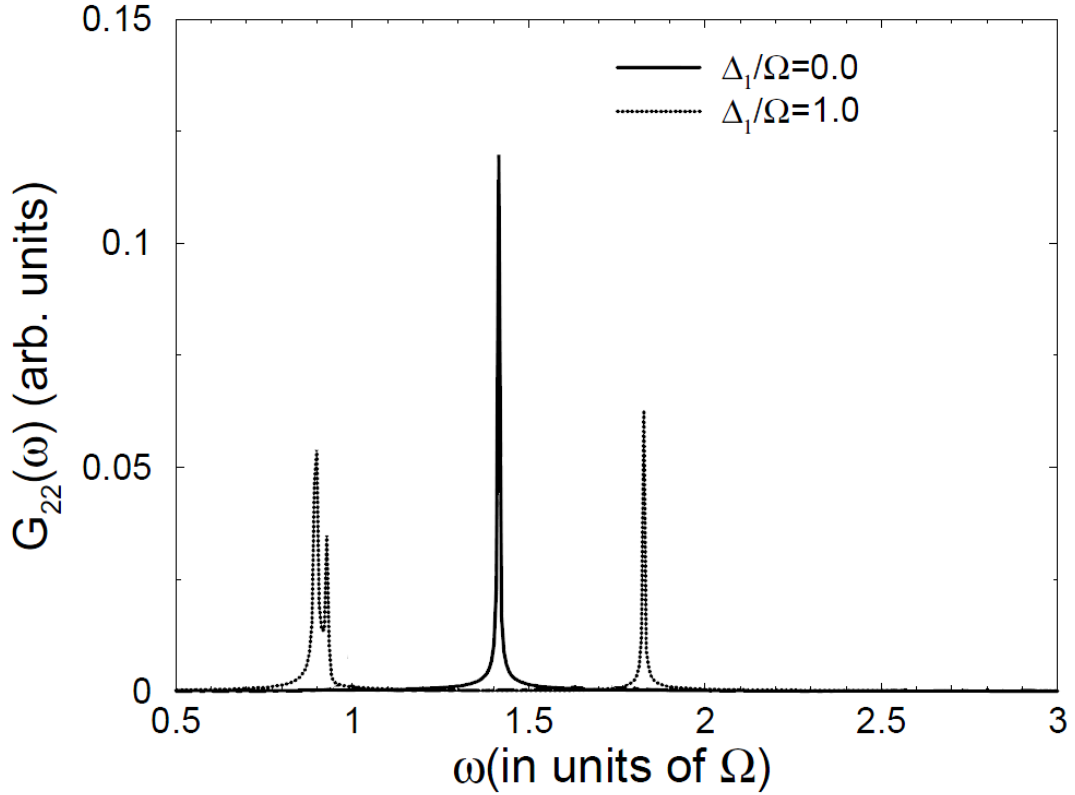


Figure 2.3: Intensity-intensity correlation spectra of a fluorescent transition in a Λ system for various values of Δ_1 for $\Delta_0 = 0$. Both transitions are driven by the same Rabi frequency Ω . The rate of spontaneous decay is low with $\gamma \ll \Omega$.

that $\Omega_0 = \Omega_2 = \Omega$ and $\Delta_0 = 0$, but Δ_1 can change away from 0. If one of the detunings (say Δ_0) is on resonance, and the other detuning (Δ_1) is not, I expect to see the three peaks in the correlation spectrum shown by numerical calculations in Fig. 2.3. To estimate the positions of the spectral peaks, Eq. 2.14 is simplified to:

$$\lambda^3 + (\Delta_1)\lambda^2 - \left(\frac{\Omega^2}{2}\right)\lambda - \frac{\Omega^2}{4}(\Delta_1) = 0 \quad (2.15)$$

and the differences in the dressed state eigenenergies are calculated.

If $\Delta_1 = 0$, then $\lambda_1 = -\frac{\Omega}{\sqrt{2}}$, $\lambda_2 = 0$ and $\lambda_3 = \frac{\Omega}{\sqrt{2}}$ and the corresponding eigenvectors are $|\phi_1\rangle = (1, -\sqrt{2}, 1)$, $|\phi_2\rangle = (-1, 0, 1)$ and $|\phi_3\rangle = (1, -\sqrt{2}, 1)$. Therefore the allowed possible real frequencies are $\omega_{12} = |\lambda_1 - \lambda_2| = \frac{\Omega}{\sqrt{2}}$, $\omega_{23} = |\lambda_2 - \lambda_3| = \frac{\Omega}{\sqrt{2}}$

and $\omega_{13} = |\lambda_1 - \lambda_3| = \sqrt{2}\Omega$. However in $G_{22}(\tau)$, which depends on density matrix element ρ_{11} , ω_{12} and ω_{23} will not show up in the spectrum because $|\phi_2\rangle$ contains a zero component for $|1\rangle$. This yields a single peak in Fig. 2.3.

If $\Delta_1 = 1$, then $\lambda_1 \approx -1.2406\Omega$, $\lambda_2 \approx 0.5850\Omega$ and $\lambda_3 \approx -0.3444\Omega$ and the corresponding eigenvectors are $|\phi_1\rangle \approx (0.1939, -0.4811, 1)$, $|\phi_2\rangle \approx (2.7092, 3.1700, 1)$ and $|\phi_3\rangle \approx (-1.9032, 1.3111, 1)$. Therefore the allowed possible real frequencies are $\omega_{12} = |\lambda_1 - \lambda_2| = 1.8256\Omega$, $\omega_{23} = |\lambda_2 - \lambda_3| = 0.9294\Omega$ and $\omega_{13} = |\lambda_1 - \lambda_3| = 0.8962\Omega$. As none of the eigenvectors contains zero elements, all three interference peaks will be observed. This yields the triple peak structure in Fig. 2.3.

If the time dependence of G_{22} is measured in an experimental system, and the frequencies in the signals extracted, the detuning Δ_1 can then be calculated in units of the Rabi frequency Ω .

2.4 Effect of Spontaneous Emission on the Correlation Spectrum

The above discussion and analytic results are based on the assumption that spontaneous decay processes are small in magnitude relative to the driven Rabi oscillations, and do not contribute significantly to the observed spectra. However, for most real systems, spontaneous decay is present and may impact the spectra that can be observed. Previous work on *resonantly*-driven 3-level *ladder* systems [68] has shown that the presence of significantly strong decay can modify the observed spectra by the inclusion of additional peaks. Therefore I investigate how spontaneous decay can affect the observed intensity spectra in our *non-resonantly* driven, 3-level Λ system.

For the example system in which $\Omega_{01} = \Omega_{12} = \Omega$ and $\Delta_0 = 0$, assuming that both transitions experience the same level of spontaneous decay γ , I find that the inclusion of spontaneous decay does not add new correlation frequencies as it does in

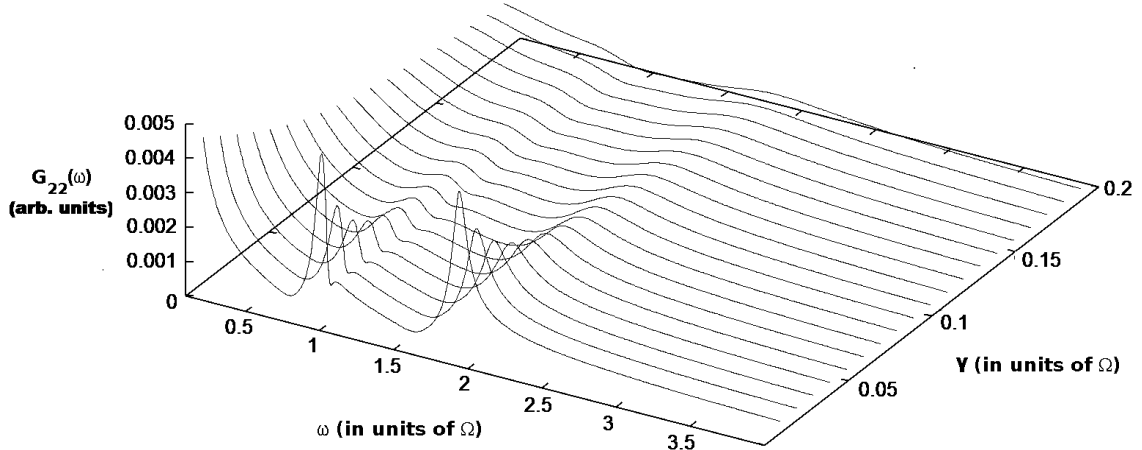


Figure 2.4: Intensity-intensity correlation spectra for increasing amounts of spontaneous decay γ with fixed detuning $\Delta_1 = \frac{\Omega}{2}$, and $\Delta_0 = 0$. As the rate of spontaneous decay increases, the peaks broaden and become less distinguishable.

the three-level ladder system [68]. In fact, under low amounts of spontaneous decay, the transitions observed are the same as those analytically predicted from Eq.2.14. However, when the decay becomes significantly strong, I observe a broadening in the correlation peaks which may obscure or merge some peaks that are closely spaced. In addition, the high rate of spontaneous decay can also obscure correlation peaks that are at low frequencies due to the system quickly reaching a steady state.

These effects can be seen in the plots below in Fig. 2.4 in which the intensity-correlation spectra are plotted for varying amounts of spontaneous decay. In all cases, the presence of significant decay serves to broaden the peaks observed. For the case of fairly high decay ($\gamma/\Omega = 0.10$), the inclusion of this decay broadens the peaks to a point at which only two of the three peaks are visible.

2.5 Effect of Dephasing on the Correlation Spectrum

In order to further examine the effect of realistic experimental conditions on the spectra, I can also examine how finite-line width or dephasing can affect the measured

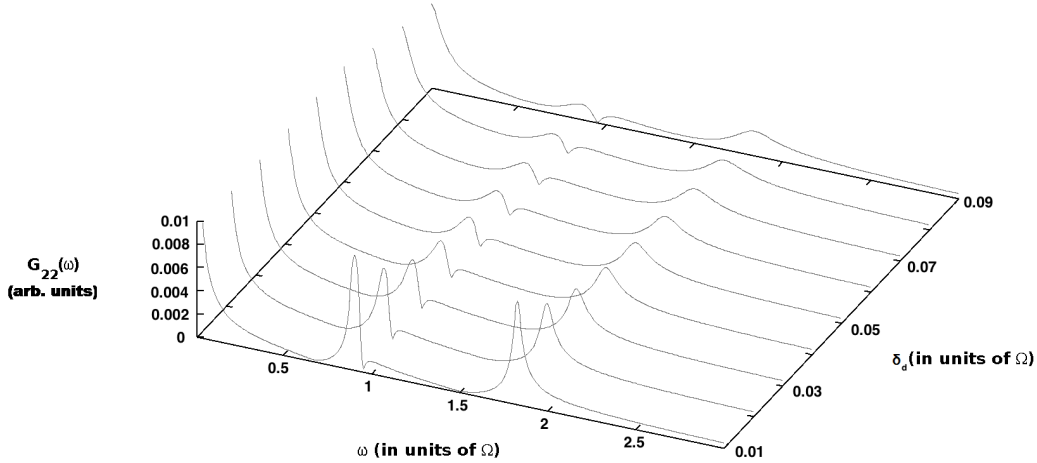


Figure 2.5: Intensity-intensity correlation spectra for increasing amounts of dephasing $\delta_d = \delta_0 = \delta_2$ with fixed detuning $\Delta_1 = \frac{\Omega}{2}$, and $\Delta_0 = 0$ as well as fixed spontaneous decay ($\gamma = 0.01\Omega$). As the rate of spontaneous decay increases, the peaks broaden and become less distinguishable.

two-time correlation spectra. In order to examine this, dephasing elements are added to the Lindblad matrix of the form:

$$L_d = \begin{pmatrix} 0 & \delta_0\rho_{01} & (\delta_0 + \delta_2)\rho_{02} \\ \delta_0\rho_{10} & 0 & \delta_2\rho_{12} \\ (\delta_0 + \delta_2)\rho_{20} & \delta_2\rho_{21} & 0 \end{pmatrix}, \quad (2.16)$$

where δ_i is the dephasing of the transition with ground state $|i\rangle$. If I take a look at the case in which the two dephasings are equal, I observe that the main effect of dephasing is similar to that of high spontaneous decay. By including dephasing in my calculations, the peaks in the spectra are broadened.

2.6 Potential Application of this Method

Since Equations 2.12 and 2.14 are directly dependent on the detuning of the various energy levels and requires the transitions to be optically connected, this indicates that the intensity correlation spectrum can be used to determine the overall energy

level structure of a complex atom directly. If a pair of transitions is driven, quantum interference effects will only be present if the two levels share a common state. This effect is useful as it is an interaction that can be observed experimentally with no need to understand the underlying properties of the states in question.

As the overall process is time-dependent, it could also form the basis for an interaction detection method. If the two-time intensity-intensity correlation spectrum were to be continuously monitored for a target transition in a three-level system, any changes that occur in the spectrum could be used to determine if any of the energy levels have changed in real time. This would indicate that an interaction has taken place, although there are many alternate ways of doing this [70, 71]. The position of the peak frequencies can then be used to extract the detuning/level shift information from the map of the expected peak frequencies in the correlation spectra due to differing amounts of detuning in both levels.

The practical application scheme is limited by the peak broadening/obscuring effect caused by significant spontaneous decay. In order for this method to yield useful quantitative results, the decoherence in the system must remain fairly small and should be driven by an electromagnetic field that is strong relative to the amount of decay. However, by driving this system with a strong electromagnetic field, the frequencies at which correlations are observed in the intensity-intensity spectra also increase. These higher frequencies are much more difficult to measure and could pose a problem experimentally. For example, if a system has a spontaneous decay time on the order of nanoseconds, in order to track these intensity correlations, it would require an experimental apparatus that can accurately measure time-dependent intensities at picosecond time intervals. Therefore, one might look at quantum systems driven by microwaves with upper-level decay rates of the order of a few microseconds to develop the practical application.

2.7 Summary

In this section, I have examined the control of a single open quantum system. For this system, the state of the atom/molecule evolves directly according to the Lindblad-Von Neumann master equation. Although an exact analytic solution for the quantum states is not available, one can analytically predict both the steady-state of these dense systems as well as the oscillating frequencies of the states.

By examining the frequencies in the second-order correlation spectra of three-level systems, I show that the quantum interference effects between transitions could be used to infer the energy level structure by testing whether or not transitions are directly connected. Such a technique may be useful as it requires no previous knowledge of the system and could be used as an ad hoc method of creating energy level diagrams in complicated molecules.

Chapter 3

Quantum Behaviour with a Classical Environment

3.1 Motivation - Improving Qubit Preparation/Cooling Times

The practical implementation of quantum computers [28] places two specific requirements on the lifetime of a quantum bit or a qubit, namely, long relevant decoherence times, and rapid state initialization times. A great deal of recent research has been devoted to proposing solutions that minimize the overall spontaneous emission rate and preserve system purity [29, 30, 31, 32, 33]. These decoherence-minimization processes lead to longer effective qubit operational lifetimes, but decoherence will ultimately render the qubit unusable due to loss of state purity. The simplest way to restore system purity is to wait for the system to cool to a pure state, usually the ground state.

Therefore for practical, reusable qubits, it is useful to design systems in which the time to cool to the ground state is minimized [28]. This time is typically quite long since the quantum state's lifetime is selected to be very large with respect to the

timescales of the control processes; i.e., the spontaneous emission rate is selected to be quite low. Thus, the desires for long operational times and short cooling times of a qubit place contradictory demands on the spontaneous emission rate of the quantum excited state. There is a need for protocols wherein the spontaneous emission rate of a quantum system can be selectively decreased so that long state lifetimes can be maintained during operation, and upon demand, selectively increased so that the cooling time can be drastically shortened in duration when qubit purity needs to be restored.

Recent experiments have increased the spontaneous emission rate of a quantum excited state by coupling the system to a nearby resonant structure such as a cavity [42, 43, 44, 45, 72], photonic crystal [46] or nanoparticle [72] based on the Purcell effect [73]. However, these studies have not been able to toggle a system between a configuration where the spontaneous emission rate is low (for qubit operation) and high (for qubit initialization).

Therefore I wanted to see if an environment could be designed that allows for both high qubit fidelity and rapid state preparation. This necessitates including an environment to dynamically modify the decoherence rates of the system in question. In order to do this, I investigated whether or not a classical environment would be capable of this effect in conjunction with a qubit. In this approach, only the quantum state behaviour of the qubit in question is evaluated with the Lindblad-von Neumann equation; the environment lacks a quantum state and only modifies parameters such as decoherence rates in the evolution of the qubit state. For this type of pure state preparation enhancement, a three-level qubit is required due to limitations inherent in two-level systems (see Appendix C.2).

3.1.1 Description of a Classical Environment

In what I call a classical environment, local structures that modify electromagnetic fields are present, but they interact with electromagnetic fields either as classical dipoles or by having a bulk index of refraction. In this type of environment, one can also assume that the environmental elements have no state memory, and do not display any quantum properties (such as electromagnetically induced transparency, spontaneous emission or quantum interference between levels).

I also assume that the state of the quantum system does not significantly affect local field intensities. This allows for the separation of the overall control calculations into two separate parts: a classical field propagation calculation, and a quantum evolution calculation.

The electromagnetic field calculations involve determining how fields propagate through the environment, and how strongly the dipole transitions present in the quantum system couple to this environment. These couplings allow us to modify our control fields and decoherence rates with constant enhancement factors [34]. As these control parameters are modified by the external environment, the input parameters of the quantum control calculation are also modified. In addition, the specific type of environment I choose to examine (noble metal nanoparticles) acts as a resonator with respect to the quantum system. The specific properties of this resonator depend on its size, shape and composition.

3.1.2 Effect of a Noble-Metal Nanoparticle on a Quantum System

One of the most effective environments for modifying quantum behaviour are nanoplasmonic environments [74]. The simplest of these environments consist of array of noble-metal nanoparticles placed onto a surface [75, 76]. As these nanoparticles are

sub-wavelength in size, the atomic electrons located inside them are able to collectively oscillate in phase with one another. This collective oscillation, referred to as a localized surface plasmon oscillation, leads to greatly enhanced local electric field intensities and strong decay modes being created around the nanoparticles at specific resonance frequencies [77]. Localized surface plasmon resonance (LSPR) is a common detection technique that uses this effect to evaluate adsorption of various objects onto nanoscale surfaces by looking for changes in this resonance [78, 79].

When a noble metal nanoparticle is illuminated by a broadband electromagnetic field, the evanescent field around the metal surface is intensified at the localized surface plasmon wavelength [80]. When a dipole emitter is placed near noble-metal nanoparticle, the rate of dipole emission is enhanced due to the Purcell effect [73, 34, 35]. Thus when a noble-metal nanoparticle is placed near a resonantly-driven quantum system, one expects the control field and the spontaneous emission rate to be enhanced.

Of these two principal types of enhancement, the enhancement to the decoherence rate is much more important in quantum control than the enhancement of the fields. This is due to the fact that field intensities are external to the quantum system itself; field enhancement can always be accounted for by adjusting the incident intensity. However, the decoherence rate enhancement is usually intrinsic to the system itself and is much harder to adjust.

One important thing to emphasize is that most standard methodologies assume that the quantum system acts as a classical dipole emitter with a known driving field intensity and frequency. This method is known to work fairly well for most systems and is largely consistent with experiment [21]. However, it requires making the assumption that the quantum state itself does not affect the coupling between the system and the environment. I will show how the nanoplasmonic modification of the spontaneous emission rate enables the rapid preparation of qubits without

compromising qubit fidelity.

3.2 Theoretical Methodology

3.2.1 Electromagnetic Field Propagation

The propagation of fields through these environmental structures are evaluated by solving Maxwell's equations numerically. Although various techniques exist for solving this problem on the nanoscale, such as the discrete-dipole approximations (DDA) [81], Mie theory [82] and diffraction optics, [83], in the time-domain one directly solves Maxwell's equations. As this solution involves calculating a propagation in time as well as space, this involves concurrently solving the Maxwell-Faraday equation and Ampere's law in differential form,

$$\nabla \times \mathbf{E} = -\mu \frac{\partial \mathbf{H}}{\partial t}, \quad (3.1)$$

and

$$\nabla \times \mathbf{H} = \epsilon \frac{\partial \mathbf{E}}{\partial t} + \sigma \mathbf{E} + \mathbf{J}. \quad (3.2)$$

In this work, a robust commercial solver (Lumerical [84]) has been used to calculate the field evolution; this particular software operates using a finite-difference time domain (FDTD) method. This method uses finite differences to evaluate spatial derivatives.

Since this technique involves numerically modelling the time-evolution of electromagnetic fields in a coarse-grained solution space, it can be easily adapted to fit any source or material inclusions. This simulation benefits from the ability to model arbitrary structures using real-space coordinates but suffers from a strong dependence on the size of the coarse-graining when compared to a basis function method such as

Green's theorem [85, 86, 87] or Mie theory [82].

After the fields have been propagated through the environmental geometry, the electric fields are recorded at various real-space coordinates.

3.2.2 Electromagnetic Field Enhancement Around a Silver Nanoparticle

The LSPR effect can be seen in Figure 3.1. Around noble-metal nanoparticles, there is an enhanced field intensity due to the strong interaction between the incident field and electrons in the metal particles. For these spherical metal nanoparticles, the strongest field enhancement is along the polarization direction of the driving field and exists in a dipole pattern. This enhancement is qualitatively similar to the increased electric field enhancement that can be determined analytically by determining the electric field distribution around a perfectly conducting nanosphere using a method of images and a constant input field [88]. This similarity is due to both the high conductivity of the noble-metals as well as the fact that, at the nanoscale, the entire metal nanosphere experiences roughly the same electric field (i.e., the dipole approximation is valid).

However, unlike the perfectly conducting sphere, a real metal nanosphere has a finite conductance, and is comprised of many oscillating bound electrons with natural oscillating frequencies [56]. This gives the area surrounding the nanoparticle a spatially dependent enhancement profile (with material properties determined by a Drude model [89]) that is tunable by modifying the size and material of the nanosphere [78]. The tunability of electric field enhancement can be seen in Figure 3.2 for Ag nanoparticles of varying radii at a distance of 10 nm from the nanoparticle's surface.

These nanoplasmonic arrays can be further tuned in what frequencies they enhance by changing the arrangement of the nanoparticles [76]. This is due to the fact that not only does each nanoparticle produce its own field enhancement, these enhancement modes are able to interfere with one another if the nanoparticles are close enough

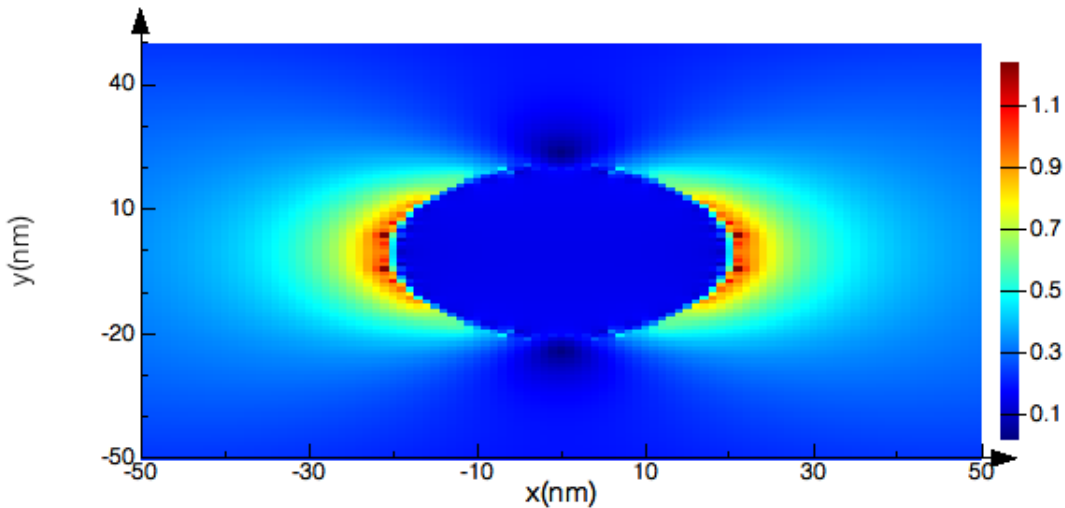


Figure 3.1: An xy plot of electric field intensities ($|E|$) at 475 nm for a \hat{y} polarized wave travelling in the \hat{z} direction around a 20 nm Ag nanoparticle.

together. Tuning such an arrangement could be as simple as placing pairs of particles differing distances apart [75]. Depending on the particle's properties and the pair's inter-particle spacing, this arrangement could have an even greater effect on the field enhancement around the nanoparticle array than a single particle [36].

The relatively high degree of tunability of these nanoplasmonic systems allows them to be easily adopted to enhance most quantum systems that have transitions in the optical range. This enhancement is also well-documented due to the use of nanoplasmonics in enhancing solar cell efficiencies [90] and in surface binding detectors [75].

3.2.3 Decay Rate Enhancement Around a Ag Nanoparticle

Initially, spontaneous emission rates for a single quantum transition are calculated using Fermi's Golden Rule. These rates are used to describe state evolution in the Lindblad-von Neumann equation when the individual quantum system in question is coupled to a photon state [21]. It is proportional to the third power of the transition frequency and is of the form,

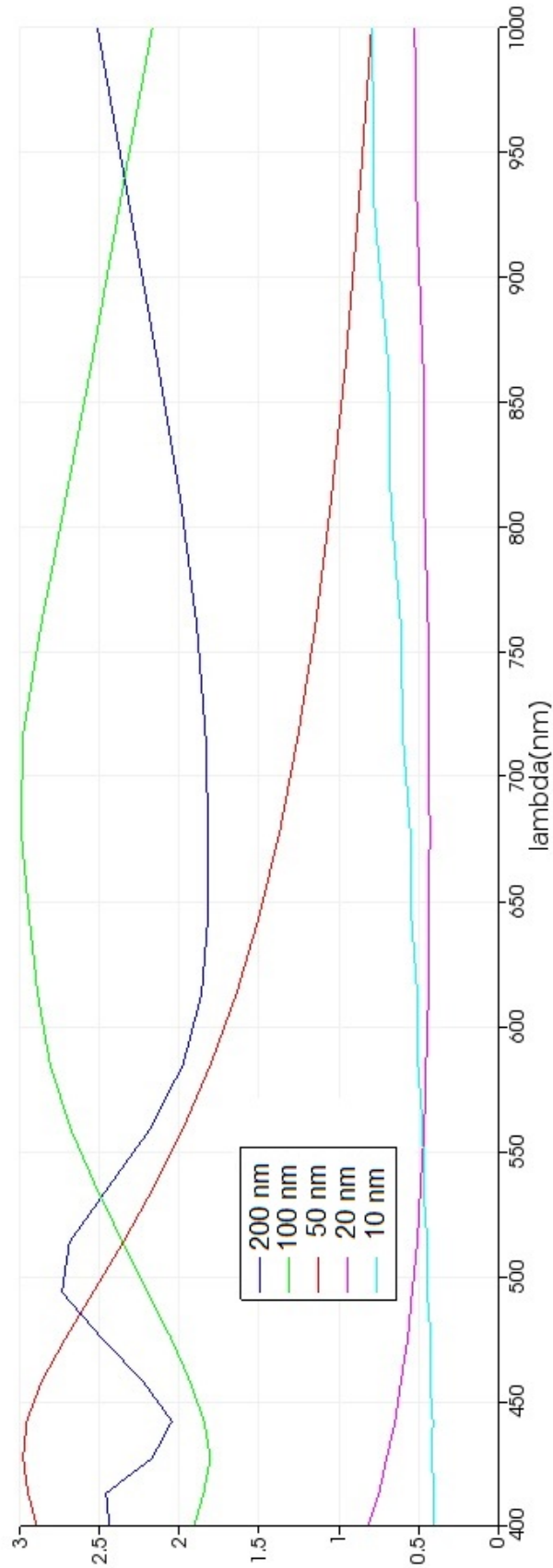


Figure 3.2: A plot of electric field intensity enhancement ($|E|/E_0$) as a function of wavelength for a \hat{y} polarized wave travelling in the \hat{z} direction at distance of 10 nm from the surface of a spherical Ag nanoparticle of radius r .

$$\gamma_{d,free} = \frac{\omega_0^3 |\mu|^2}{3\pi\epsilon_0 \hbar c^3} = \frac{\omega_0^3 |\langle g|\hat{\mu}|e\rangle|^2}{3\pi\epsilon_0 \hbar c^3}, \quad (3.3)$$

where ω_o is the frequency of the transition and μ is transition dipole moment. This equation assumes that the driving fields are on resonance with the transition, the fields and decay rates are constant at all times and that the system is decoupled from its environment.

However, when dealing with a system that can couple to external modes, it is possible to modify this decay by assuming that the transitions in the system behave as radiating electric dipoles. In this case, an approximate modified decay rate can be calculated by comparing the power that is emitted from the system in its environment, as compared to that same system in free space [34, 21]. Thus, the new decay rate can be determined by [21],

$$M_d = \frac{\gamma_d}{\gamma_{d,free}} = \frac{Power}{Power_{free}}. \quad (3.4)$$

In a classical environment, it is assumed that the transitions behave like classical dipoles at all times. In this case, the transition can be modelled as an oscillating electric dipole source, of frequency ω , and placed into the environment. The coupling of this source to nearby environmental objects is then calculated to find the power emitted by the transition [34, 35]. In the FDTD solver, this can be done by defining a 3D surface enclosing just the dipole, and by calculating the Poynting vector along the surface:

$$\mathbf{S}(r, \omega) = \frac{1}{\mu_0} \mathbf{E}(r, \omega) \times \mathbf{B}(r, \omega). \quad (3.5)$$

The power emission leaving through this surface (with a defined area vector \mathbf{A}) is calculated as,

$$Power = \oiint_A \mathbf{S}(r, \omega) \cdot d\mathbf{A}. \quad (3.6)$$

This power emission is then compared to the power emission of a classical dipole to determine the decay enhancement factor, as a function of frequency, using Equation 3.4. This effect of a proximate noble-metal nanoparticle was used to examine the possibility of surface-enhanced state purification with two-level systems and details of that investigation (and its inherent limitations) are included in Appendix C.

The fact that the decay enhancement is dependent on the dot product $(\boldsymbol{\mu} \cdot \mathbf{E})$ indicates that the polarization of the transition dipole of a driven state can be used to selectively enhance its decoherence rate. This effect should allow for polarization control of decoherence if the system is placed next to an asymmetric environment. I will therefore use this to propose a system in which rapid state preparation can be achieved in conjunction with high qubit fidelity.

3.3 Control of a Quantum System between two Silver Nanoparticles

I now propose a scheme to enhance the spontaneous emission rate of a quantum state “on demand”, so that quantum states can be rapidly initialized (so-called “rapid reset”) without shortening their operational lifetimes. In this scheme, a quantum system (such as a quantum dot) is placed in between a pair of noble-metal nanoparticles, and controlled by a linearly polarized electromagnetic wave that propagates perpendicularly to the interparticle axis. The local surface plasmon resonance phenomenon and the accompanying enhancement of the local field around noble-metal nano structures is well-known[80, 75, 76]. It is also well-known that the spontaneous emission rate of a quantum emitter in the middle of two Ag nanoparticles is enhanced and is

strongly frequency dependent, thus applied to surface-enhanced fluorescence [91, 35]. It is less well-known that the modification of the spontaneous emission rate due to the weak coupling to the surface plasmon modes exhibits a strong dependence on the polarization of the incident light [21, 92]. In the scheme I describe below, changing the polarization direction of the electromagnetic wave from perpendicular-to-the-interparticle-axis to parallel-to-the-interparticle-axis changes the spontaneous emission rate of a quantum emitter at a particular wavelength from very low to very high. This effect can be used to develop a protocol wherein one of the arms of a three-level Λ system (3LLS) can be used as a qubit that has a long coherence lifetime during the operational mode, and quickly reset to a pure state when the qubit becomes unusable due to decoherence.

In my calculations, a radiating dipole (modelling a quantum dipole transition in a qubit) is placed equidistantly between two spherical Ag nanoparticles, of radius r and surface-to-surface separation d as shown in the inset in Fig. 3.3a). The resonance spectra of these NPs can be tuned by changing their size and composition [93], allowing for a wide variety of quantum systems to be used as a qubit platform. I assume that the dipole is oriented by the polarization of an electromagnetic wave that illuminates the nanoparticles. I examine two cases — firstly when the dipole is oriented perpendicular to the interparticle axis (\hat{z}), and secondly when the dipole is oriented parallel to the interparticle axis (\hat{x}).

Fig. 3.3 shows the modification of (a) the local electromagnetic field and (b) of the spontaneous emission rate of a quantum emitter placed in between two silver nanoparticles when the electromagnetic wave illuminating the system is \hat{x} -polarized parallel to the interparticle axis (red, dashed line), and \hat{z} -polarized perpendicular to the interparticle axis (blue, solid line). The radius of the nanoparticles is chosen to be 20nm and the inter-particle surface-to-surface spacing as 12nm so that the localized surface plasmon resonance frequency, calculated to be 370 nm, matches the

transition frequency of the qubit. This frequency is similar to transition frequencies found in ultraviolet quantum dots such as ZnO [94] and due to the tunability of both the nanoparticle resonance and the qubit energy level spacing, such a frequency choice serves as a good model to illustrate how polarization control can speed up qubit initialization. I also assume that these systems have no inherent preferred quantization axis.

The local electromagnetic field vector components (E_x, E_y, E_z) at the location of the quantum emitter (halfway in between the nanoparticles on the interparticle axis) due to the driving fields are calculated numerically by solving Maxwell’s equations for different incident field polarizations. A commercial-grade simulator based on the finite-difference time domain method was used to perform the calculations [84]. The optical response of the material is determined by fitting the Drude model using experimental constants [89]. The magnitude of the incident electric field is assumed to be E_0 in both polarizations. I define a “field enhancement factor” $M_{E,i} = |E_i|/E_0$, distinct from the intensity magnification factors usually reported in studies of surface-enhanced processes. Figure 3.3(a) shows the field enhancement factors in the \hat{z} (blue, solid line) and \hat{x} (red, dashed line) components of the field when the incident light is polarized in the same (\hat{z} or \hat{x}) direction. These two curves show that the presence of the nanoparticles greatly enhances the field strength in the direction of polarization of the incident light. Thus, the driven qubit is driven much harder (or the Rabi frequency increases) due to the presence of the proximate nanoparticles.

The rate of spontaneous emission of the quantum emitter changes when placed in between the two AgNPs. This change in the rate of spontaneous emission is calculated by modelling the quantum emitter as a point oscillating dipole source. I compare the power emitted by the point dipole source with (P_{NP}) , and without the nanoparticles (P_{NoNP}) [34] by solving Maxwell’s equations numerically [84]. The decay enhancement factor M_d is calculated as a ratio of P_{NP} to P_{NoNP} immediately

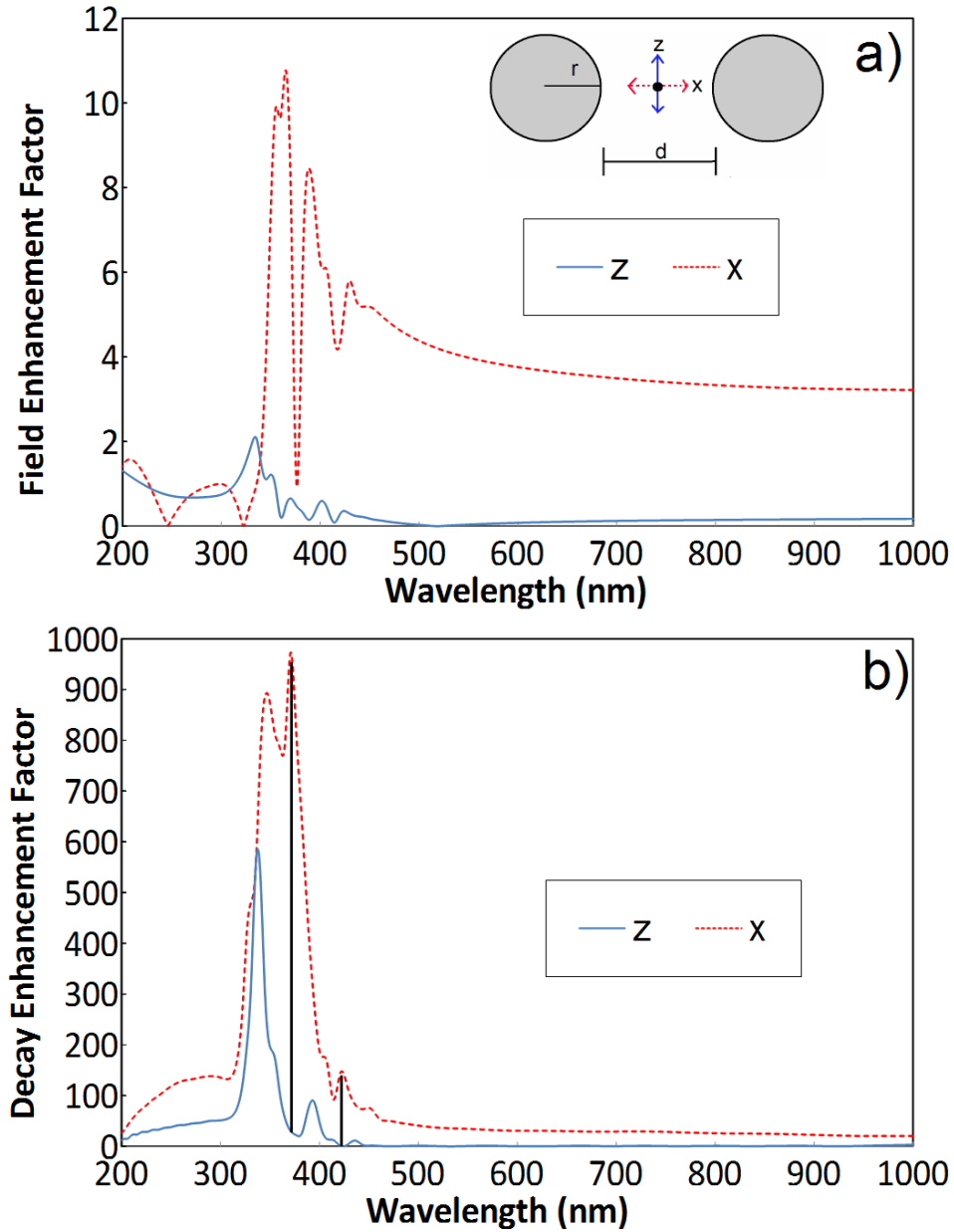


Figure 3.3: (a) Field enhancements ($M_{E,i} = |E_i|/E_0$) and (b) decay rate modification ($M_d = \gamma/\gamma_0$) of the quantum emitter placed halfway in between two silver NPs with $r = 20$ nm and $d = 12$ nm surface-to-surface separation for two different incident polarizations. The blue, solid (red, dashed) curves corresponds to when the incident field is perpendicular (parallel) to the interparticle axis. The two solid vertical lines in (b) correspond to the maximum decay rate enhancement for the \hat{x} orientation (370 nm) and the largest relative ratio of decay rate enhancement, \hat{x}/\hat{z} (≈ 420 nm).

around the dipole source. This decay enhancement factor is also the ratio of the spontaneous emission rate of the dipole emitter with the nanoparticles γ to the vacuum spontaneous emission rate γ_0 [21]. The decay enhancement factor as a function of wavelength is evaluated for two different orientations of the dipole; one in which the dipole is perpendicular to the interparticle axis (\hat{z}) and the other in which it is parallel to the interparticle axis (\hat{x}), and presented in Fig.3.3(b). I see that at wavelengths near the qubit resonance, the rate of spontaneous emission of the quantum emitter can be increased by switching from z to x polarization.

Thus the polarization of the driving field both modifies the Rabi frequency and the spontaneous decay rate of the qubit transition parallel to it. Based on the above analysis, the wavelength of the incident electromagnetic wave is chosen so that the ratio of parallel decay rate (γ_x) to the perpendicular decay rate (γ_z) is maximized (≈ 420 nm).

For a practical qubit implementation, I offer the following protocol:

Step 1: Consider a three-level quantum system in the ‘lambda’-configuration (3LLS), with both ground states $|g\rangle$ and $|c\rangle$ being somewhat close in energy though not degenerate. The lifetime of the excited state $|e\rangle$ is long enough for the quantum system to be a good candidate for quantum information processing. This system can then be placed in between two silver nanoparticles. The two ground states, $|g\rangle$ and $|c\rangle$, are chosen as the qubit, and gate operations are carried out by a near-resonant electromagnetic wave polarized in the \hat{z} -direction — perpendicular to the interparticle axis. This allows the rate of spontaneous emission from the excited states, $\gamma_{ge,z}$ and $\gamma_{ce,z}$, to remain fairly low. Without loss of generality, one can assume that the ground states are angular momentum $j = 0$ states, and the excited state is a $j = 1$ state, thus the applied linearly polarized field transitively connects the $|g, j = 0, m = 0\rangle$ state with the $|e, j = 1, m = 0\rangle$ state.

Step 2: When the qubit becomes unusable due to decoherence, and the state needs

to be initialized, the polarization of the incident electromagnetic wave is rotated by 45° to excite both along the \hat{z} and \hat{x} directions. Polarization selection rules create a five-level system transitively connected as shown in Fig. 3.4. The z -polarized components continue to connect the $|g, j = 0, m = 0\rangle$ and $|c, j = 0, m = 0\rangle$ states with the $|e, j = 1, m = 0\rangle$ state, and the spontaneous emission stays low (blue, solid lines). The x -polarized components connect the $|g, j = 0, m = 0\rangle$ state and $|c, j = 0, m = 0\rangle$ with the $|e, j = 1, m = \pm 1\rangle$ states, and the spontaneous emission from the latter states are high (red, dashed lines).

If the detunings of both transitions are kept equal $\Delta_{ge} = \Delta_{ce}$, a Morris-Shore [95, 96] transformation shows that these transition dipole couplings put the 3LLS into a dark state [97, 98], i.e., a superposition of the two ground states of the five-level system, which is a pure state. Thus, regardless of the initial quantum state of the system, the state can be rapidly reset into a pure state, i.e. the dark state.

Step 3: The rest of the qubit initialization can be completed by rotating the polarizations of the two electromagnetic waves perpendicular to the interparticle axis. In this configuration, the spontaneous emission from the excited state $|e\rangle$ is low, and population can be transferred coherently to the qubit ground state $|g\rangle$.

The speed of state initialization is determined by the time that it takes the system to reach a steady state (the dark state) in Step 2. Although there are six different decay rates (one for each transition in Fig.3.4), the overall time taken to reach the dark state depends mostly on the *fastest* spontaneous decay constant, especially if that decay time is much faster than the others. This means that if, due to the presence of a plasmonic nanostructure, only one decay rate is enhanced greatly, the entire preparation time will be reduced. In order to demonstrate this numerically, I use the Hamiltonian (assuming that the upper levels are degenerate) in the rotating

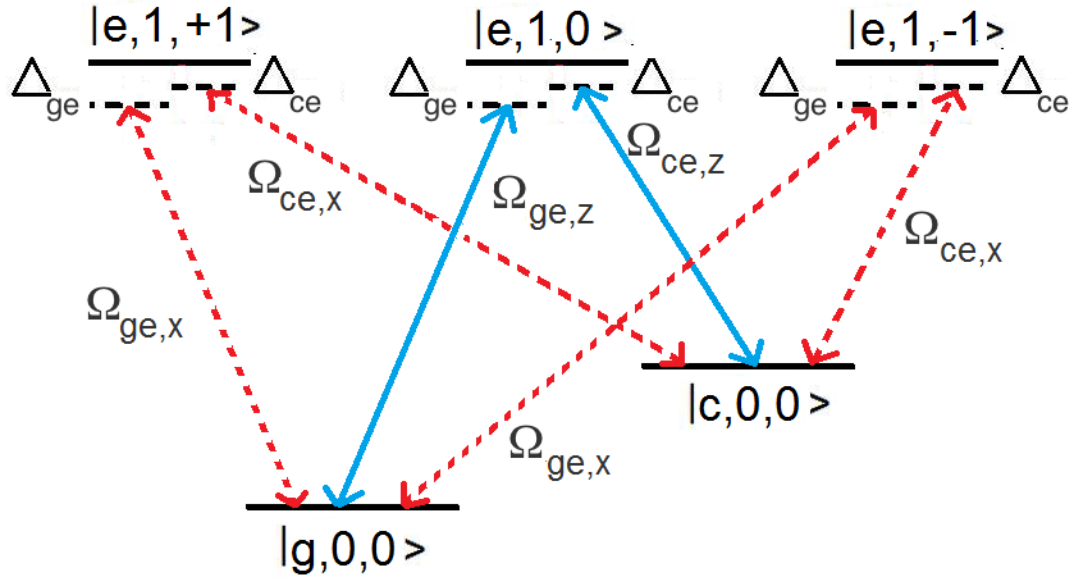


Figure 3.4: Polarization control scheme for rapid qubit initialization. Two applied fields near resonant with the $|g\rangle - |e\rangle$ and $|c\rangle - |e\rangle$ transitions are linearly polarized in the $x - z$ plane. The z components of the field excite the blue (solid) transitions, while the x components of the field excite the red (dashed) transitions. For preparation, the Rabi frequencies of all transitions are high with respect to spontaneous decay rates. The spontaneous emission rates of the operational (blue, solid) transitions, $\gamma_{ge,z}$ and $\gamma_{ce,z}$, stay low, whereas those of the preparation transitions (red, dashed), $\gamma_{ge,x}$, and $\gamma_{ce,x}$, are greatly enhanced. The detunings are chosen to coherently trap the system in a dark state.

wave approximation:

$$H_{RWA} = \begin{pmatrix} -\hbar\Delta_{ge} & \frac{\hbar\Omega_{ge,z}}{2} & \frac{\hbar\Omega_{ge,x}}{2} & \frac{\hbar\Omega_{ge,x}}{2} & 0 \\ \frac{\hbar\Omega_{ge,z}^*}{2} & 0 & 0 & 0 & \frac{\hbar\Omega_{ce,z}}{2} \\ \frac{\hbar\Omega_{ge,x}^*}{2} & 0 & 0 & 0 & \frac{\hbar\Omega_{ce,x}}{2} \\ \frac{\hbar\Omega_{ge,x}^*}{2} & 0 & 0 & 0 & \frac{\hbar\Omega_{ce,x}}{2} \\ 0 & \frac{\hbar\Omega_{ce,z}^*}{2} & \frac{\hbar\Omega_{ce,x}^*}{2} & \frac{\hbar\Omega_{ce,x}^*}{2} & -\hbar\Delta_{ce} \end{pmatrix}; \quad (3.7)$$

If the detunings of the applied fields from the two transitions are equal to each other ($\Delta_{ge} = \Delta_{ce}$), the population will be coherently trapped in the dark state. I assume that ratio of the Rabi frequencies of the driven transitions are equal to each other, i.e., $\frac{\Omega_{e,x}}{\Omega_{e,z}} = \frac{\Omega_{c,x}}{\Omega_{c,z}}$. The rapidity with which the system reaches a ground state is determined by the relative magnitudes of the Rabi frequencies versus the decay rates of the transitions. If the Rabi frequencies are much greater than the decay rates, the system will rapidly reach the dark state.

As an example, I look at a 3LLS that, under the influence of decoherence in Step 1, has evolved into a completely mixed state ($\rho_{gg} = \rho_{(e,0)(e,0)} = \rho_{cc} = \frac{1}{3}$). The time needed to reach the dark state (with calculated $Purity = Tr(\rho^2) > 0.999999$) as a function of increasing spontaneous emission rate can be seen in Fig. 3.5 for varying driving field strengths. As the spontaneous emission rate of a transition increases, the time to reach the dark state decreases linearly. This happens until the time that the spontaneous emission rate is comparable to the Rabi frequency, and further increase in the spontaneous emission rate *increases* the time to reach the dark state. I see that the time needed for the system to reach the pure dark state decreases linearly with respect to the higher decay rate enhancement, even if that enhancement affects only a single transition and the system is initially in a state that is unaffected by that increased decay rate. However, once the highest decay rate becomes greater than the driving Rabi frequency, this time reduction is lost as the fields are unable to drive

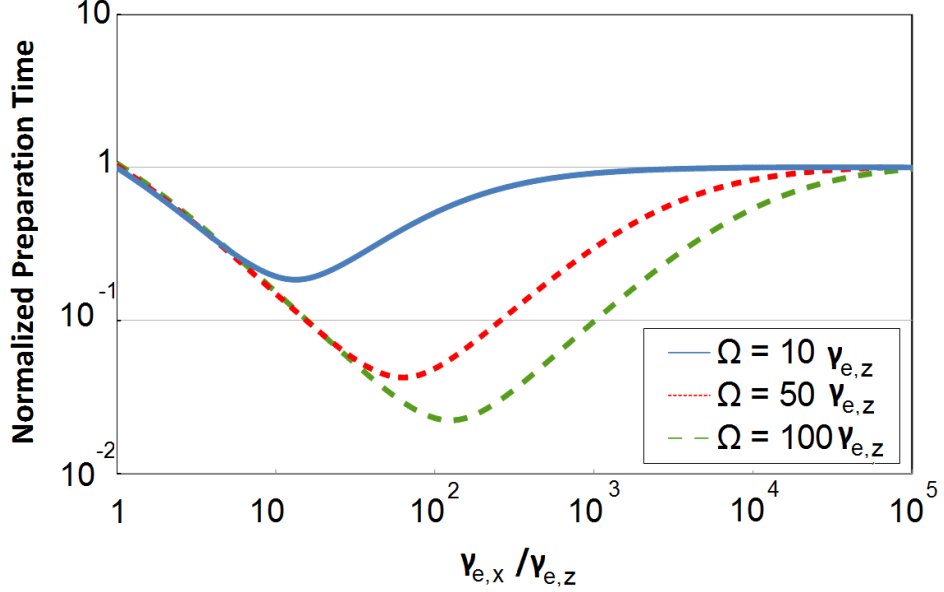


Figure 3.5: The time required to reach a final, pure state is plotted with respect to the ratio of spontaneous decay rates ($\gamma_{ge,x}/\gamma_{ge,z} = \gamma_{ce,x}/\gamma_{ce,z}$) for various driving field strengths. The effective five level system is initially driven from an operational, completely mixed state ($\rho_{gg} = \rho_{(e,0)(e,0)} = \rho_{cc} = \frac{1}{3}$). The calculation parameters are $\Omega_{ce,x} = \Omega_{ge,x} = \Omega_{ce,z} = \Omega_{ge,z}$, $\gamma_{ge,x} = \gamma_{ce,x} = \gamma_{e,x}$ and $\gamma_{ge,z} = \gamma_{ce,z} = \gamma_{e,z}$. The preparation time is normalized to the time taken for an equivalent three-level λ system to reach a steady state.

significant population into these high decay states faster. This also indicates that this state initialization effect will only show up when the red (dashed) transitions are strongly driven. This allows for the preservation of low decoherence rates when the fields are only z -polarized.

For the practical implementation of this protocol, some additional considerations may need to be accounted for. Firstly, in these calculations, I have assumed that the quantum emitter is a point dipole with no preferred quantization axis. This is not true in general for systems such as quantum dots; however, the protocol will succeed as long as the spontaneous emission rate of the system is asymmetric, i.e. significantly different for two orthogonal polarizations of the incident field. Secondly, I assumed that the incident field is a plane wave, whereas in experiments, the field is likely to be a strongly focussed beam for qubit addressing. The latter introduces an

additional polarization (in the y-direction); however, as the effects of the y-polarized components are similar to those of the z-polarized components due to the symmetry of the system, this will not substantially alter the ability to selectively enhance the preparation rate.

3.4 Summary

In this chapter, I have examined the behaviour of a single quantum system interacting with a classical environment. For this system, the state of the atom/molecule evolves according to the Lindblad-Von Neumann equation. However, the intensity and decoherence experienced by the system is modified due to the environment. The effect of the environment is calculated separately from the state of the quantum system using standard techniques and tools from computational electrodynamics.

By examining the effect that a nanoplasmonic environment has on a nearby quantum system, I showed how this interaction can change the spontaneous emission and decoherence rates of the system. I also examined this effect in more detail by looking at the directional dependence of this decay enhancement. I showed that even for a simple dimer of Ag nanoparticles, the decay enhancement is highly asymmetric.

I then showed that this asymmetry can be used to selectively enhance the spontaneous emission rate of a nearby quantum system. This increase allows for rapid state preparation without greatly compromising useful state lifetimes. The above results have been published in *Phys. Rev. A* [99].

Chapter 4

Quantum Behaviour in Dense Ensembles

This study was motivated by a desire to enhance silicon solar cell efficiencies. In these solar cells, electricity is only produced by photons with $\lambda < 1100nm$ due to the band gap in silicon; however, the spectrum of sunlight includes much higher wavelengths that are wasted [100]. If one were to design a hybrid quantum-nanoplasmonic system that allowed for significant amounts of infrared photons to be blueshifted, one could recoup some of this under-utilized energy.

The Lorentz-Lorenz model [56], detailed in Appendix D, of an atomic electron driven by an incident electromagnetic field predicts that the induced polarization has a frequency that is blueshifted. It can be expected that the induced electric field will also be at a blueshifted frequency compared to the incident field. For example, a neodymium-like emitter, for which the ground to excited state transition energy is ≈ 1 eV, when placed onto silicon that has a bandgap of just above 1 eV, could theoretically blueshift wavelengths and increase the silicon's absorption.

I speculate that a dense arrangement of these types of emitters on the silicon would be able to amplify this blueshifting effect. Therefore I consider a dense ensemble of

Nd atoms and try to extract the macroscopic/collective effects from the microscopic dynamics.

In dense quantum ensembles, there are strong inter-particle interactions that both scatter, emit and absorb incoming electromagnetic radiation. This causes the ensemble to effectively serve as its own environment. Unlike in the classical environment, the states of the individual quantum systems significantly affect local field intensities. This requires that both the field propagation and the density matrix evolutions be done concurrently.

In order to study this effect, one would need to solve both Maxwell's equations and the Liouville-Von Neumann equation concurrently. This is due to the fact that there is both a quantum evolution of states occurring in the system, and this evolution of states in turn changes the electromagnetic field propagation. This study is conducted by modelling the evolution of a dense quantum ensemble that serves as a "nanoparticle" and comparing the classical effects to the macroscopic behaviour of the quantum ensemble.

In typical scattering and field enhancement simulations [47, 49, 84, 34], broadband pulse methodologies are used to determine scattering off of nanostructures. In these methodologies, a broadband short pulse illuminates the system and the scattered field is tracked and Fourier-transformed to yield an appropriate intensity spectrum. It is then assumed that this spectrum can be used to determine the overall scattering of incident waves as a function of frequency. This further assumes that the scattered field is always of the same frequency of the incident field. I will show that these assumptions are inadequate for studying a driven, dense quantum ensemble.

4.1 Theory and Implementation

I model a dense ensemble of quantum emitters and drive it with a linearly polarized external field. Though the driving field is polarized in one direction, spontaneous emission from each quantum system excites transitions in nearby quantum systems in other directions. Each of the quantum emitters contributes to a “mean field” that mediates the interactions between various quantum emitters. This mean field in the ensemble is a spatially varying, 3D vector. Therefore, the dynamics of an individual quantum system involves a ground state and three excited states, one for each Cartesian direction of the atomic dipole interacting with the mean field.

4.1.1 Evolution of the Electromagnetic Field and the Quantum State

In this study, Maxwell’s equations are solved numerically in time for a coarse-grained grid using a pseudo-spectral time domain method (PSTD) [101, 102] detailed in Appendix E. The choice of using a PSTD method over the FDTD method is largely due to the fact that the PSTD method is computationally faster and more stable than the FDTD method [101, 102]. It also has the added benefit of using a single lattice grid as opposed to the staggered grid required of the FDTD method [103].

While the field propagation is similar to that in Chapter 3, the implementation of the quantum evolution changes significantly. This is due to the fact that:

- the direction of each atomic transition dipoles becomes relevant, requiring basis states for all three directional orientations, and
- the states no longer interact with fields with single frequencies due to the creation of local, time-dependent fields from nearby quantum elements.

Both these effects are accounted for by modifying the choice of density matrix

basis, and by not including the rotating wave approximation.

4.1.2 Generalized Directional State Basis

In the quantum control of a two-level atom by an incident monochromatic field, one typically views the atom as having states $|g\rangle$ and $|e\rangle$. One then treats the transition as an interaction of the field with the dipole oscillator; the strength of the transition coupling is proportional to the potential energy interaction between the atomic dipole and the electric field vector ($\boldsymbol{\mu} \cdot \mathbf{E}(\mathbf{r})$). For a single atom interacting with a single field, the quantization axis is assumed to be along the direction of polarization and only two atomic levels are coupled by the field .

This assumption is not universally applicable. When radiating dipole are in proximity to either noble-metal nanoparticles, or to other dipoles that they can interact with, $\boldsymbol{\mu} \cdot \mathbf{E}(\mathbf{r})$ is no longer equal to $\mu E(\mathbf{r})$. This requires one to take into account all components of the dipole moment operator.

Typically, one works in the angular momentum basis and uses the Wigner-Eckert theorem to find the transition matrix elements for coupling between various quantum states. For transitions between states with large angular moments, this becomes a large problem.

A simpler way to approach this problem is to introduce a “directional” state basis. These “directional” states are those accessed by transitions that are driven by a single field polarization [104]. In this type of structure, the transitions are analogous to those from an $l = 0$ ground state to an $l = 1$ excited state. For these states,

$$|g\rangle = |l = 0, m = 0\rangle, \quad (4.1)$$

$$|e_z\rangle = |l = 1, m = 0\rangle, \quad (4.2)$$

$$|e_x\rangle = \frac{1}{\sqrt{2}}[|l = 1, m = -1\rangle + |l = 1, m = +1\rangle], \quad (4.3)$$

$$|e_y\rangle = \frac{i}{\sqrt{2}}[|l=1, m=-1\rangle - |l=1, m=+1\rangle] \quad (4.4)$$

The Hamiltonian in this directional basis is:

$$H = \begin{pmatrix} 0 & \hbar\Omega_{e_x,g} & \hbar\Omega_{e_y,g} & \hbar\Omega_{e_z,g} \\ \hbar\Omega_{e_x,g}^* & E & 0 & 0 \\ \hbar\Omega_{e_y,g}^* & 0 & E & 0 \\ \hbar\Omega_{e_z,g}^* & 0 & 0 & E \end{pmatrix}. \quad (4.5)$$

with degenerate energy levels, E , and with the dipole-field interaction taking the form $\Omega_{e_\eta,g} = \mu_{e_\eta,g}E_\eta$ where $\eta = (x, y, z)$.

To summarize, in the case of a two-level system with a well-defined ground state $|g\rangle$ and excited state $|e\rangle$, if the control field defines the quantization axis, the atomic state can be represented with a density matrix based on a singular ground state, $|g\rangle$, and a single excited state, $|e\rangle$. In the case of the control field not being parallel to the quantization axis, the density matrix requires three excited states ($|e_x\rangle, |e_y\rangle, |e_z\rangle$), one for each transition direction. This change in state-structure is depicted in Figure 4.1. This results in an effective four-level system which can display quantum interference.

4.1.3 Mean-field Environmental Interaction

A microscopic representation of a large number of open quantum systems interacting with one another would be too computationally intensive to be feasible. Since the Lindblad-Von Neumann equation involves matrix multiplication, this computation becomes onerous for large number of quantum systems in the ensemble; even the most modern, optimal methods scale more slowly than M^2 [105], where M is the total number of states (for N systems, $M = 4N$ for the atomic structure in Fig. 4.1).

Therefore I describe the interaction between the members of the ensemble using

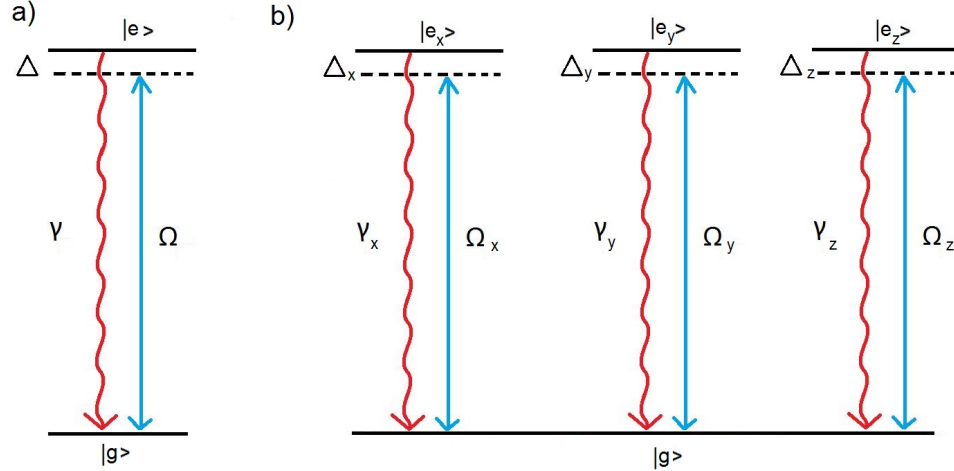


Figure 4.1: a) When the polarization of an electromagnetic field sets the quantization axis of an atom, the effective quantum system is a two-level system with the direction of the transition dipole oriented along that polarization direction. b) When the polarization of an incident control field is different from the quantization axis, the effective quantum system is a four-level system with a dipole transition oriented along each field component.

a mean-field method. In this method, spatially separated quantum systems do not directly interact with one another through the Hamiltonian or Lindblad operators. Instead each quantum system interacts with and contributes to a local, mean field and sees the behaviour of other systems through this mean field. This method of using a mean-field interaction shows up in numerous areas in computational physics, such as in polymer self-consistent field theory [106] and other computational electrodynamics [107]. For clarity, the “mean” in the mean field refers to a mean of the interactions between molecules and not a spatial mean of the fields themselves.

This mean field is a sum of the external incident field that excites the system and a local field created by the driven and spontaneously emitting quantum elements (quantum emitters) in the ensemble:

$$\mathbf{E}(\mathbf{r}, t) = \mathbf{E}_{inc}(\mathbf{r}, t) + \mathbf{E}_{local}(\mathbf{r}, t). \quad (4.6)$$

This simplification allows the overall quantum state space to remain relatively

small. For a system consisting of N four-level systems, the total directional state space ($M = 4N$) is reduced to $4N$ quantum states and $3N$ local quantum interactions. This greatly simplifies the overall problem and allows us to evaluate the problem by evolving the density matrices locally with an efficient parallel implementation (see Appendix E.1.3). With the ensemble state basis reduced to a more manageable size, one now needs to determine how the quantum elements can create the local fields.

4.1.4 Electromagnetic Field Generation From Quantum Elements

In classical simulations, the response of microscopic elements to the local field are analytically defined since the elements are classical objects. In order to determine the response of quantum elements to the local field, one needs to know the current state they are in. This state is then related a physical observable, the local dipole moment, using a dipole moment operator. The directional components of this operator can be found by [47]),

$$\hat{\mu}_\eta = -\frac{\partial \hat{H}}{\partial E_\eta}, \quad (4.7)$$

where $\eta = (x, y, z)$. The instantaneous, local, expectation value of this operator is,

$$\langle \hat{\mu}_\eta(\mathbf{r}) \rangle = Tr(\rho(\mathbf{r})\hat{\mu}_\eta), \quad (4.8)$$

where $\rho(\mathbf{r})$ is the instantaneous density matrix of an individual emitter.

This procedure can be modified to find the components of local, instantaneous free current that enters into Maxwell's equations (see Appendix E.1),

$$J_\eta(\mathbf{r}) = \left\langle \frac{\partial}{\partial t} \hat{\mu}_\eta(\mathbf{r}) \right\rangle = Tr(\dot{\rho}(\mathbf{r})\hat{\mu}_\eta). \quad (4.9)$$

In this formalism, I assume that the dipole moment operator of the system is constant ($\hat{\mu}$ for each transition is constant) and I evaluate $\rho(\mathbf{r})$ using the Lindblad-Von Neumann equation for the density matrix at each spatial location.

This dependence of the local free current on the density matrix is what differentiates this quantum system from the classical system. This methodology allows us to investigate more complex phenomena and allows us to examine where assumptions in standard computational methods break down.

4.1.5 Summary of Evolution Methodology

The evolution of the electromagnetic fields and the state of the quantum ensemble is carried out using the following procedure [47]. The simulation space is broken into a 3D computational grid, with each cell having associated with it an electric and magnetic field.

- The source cells (plane wave source) fields are updated analytically.
- Maxwell's equations are updated using a PSTD method for the H field.
- If there is a quantum emitter present in a cell, the density matrix of that cell is evolved using the Lindblad equation and the electric fields at the previous time-step.
- The free current in each cell is determined for cells containing a quantum emitter.
- The free current is used to modify the local E field using Maxwell's equations.
- The process is repeated and items of interest are recorded..

This order of operations avoids self-interactions in a single lattice cell [47].

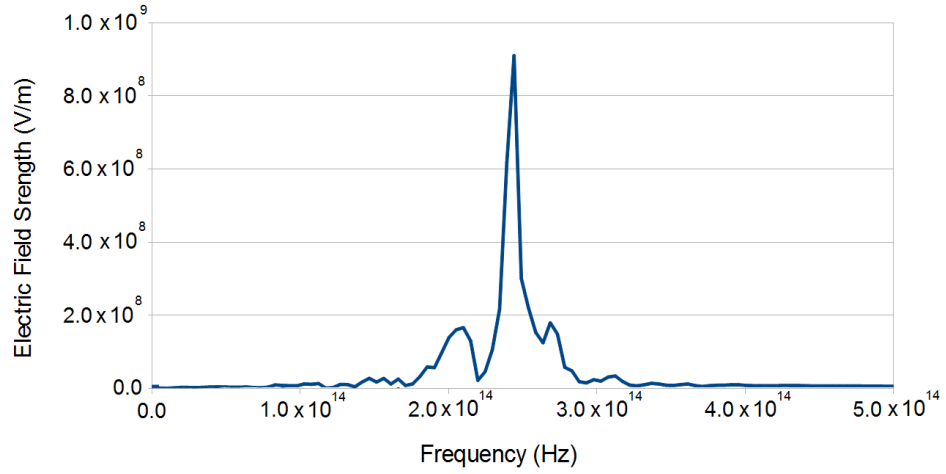
4.2 Spectrum of the Electric Field Outside a Driven Nanosphere

With this methodology in place, I simulate the response of a dense quantum ensemble to incident continuous-wave, monochromatic light in order to examine whether or not the frequency of the evanescent field around the ensemble can be blueshifted.

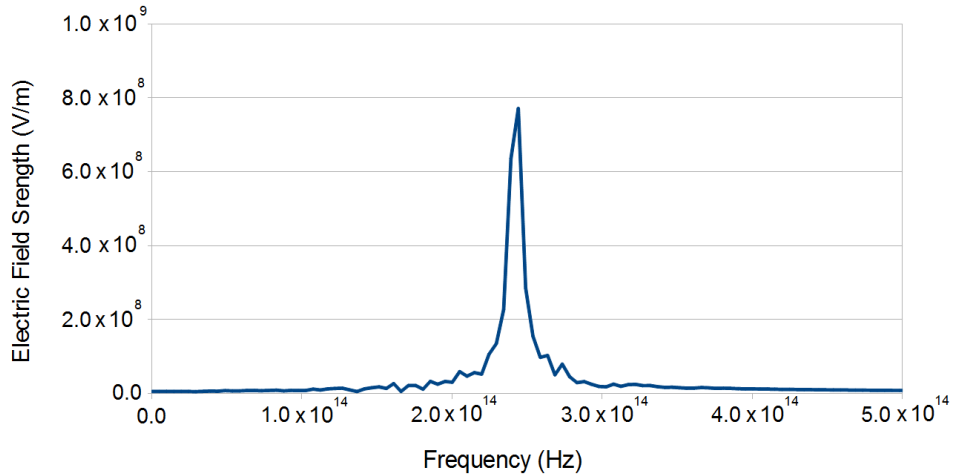
I investigate a collection of dense quantum emitters, arranged in the form of a 10 nm nanosphere. I illuminated the nanosphere with a monochromatic, plane wave polarized in the \hat{y} direction and track the field amplitude a short-distance (3 nm) outside the nanosphere for 200 fs (0 fs to 200 fs). By Fourier-transforming this field amplitude into a spectrum, I can see that the electromagnetic field around the nanosphere is no longer purely monochromatic (Fig 4.2(a)) even if the input is. There is a blueshifted component that appears.

While this investigation appears on the surface to be successful, I found that in reality, it is not. This is due to the fact that, although frequency-shifted photons are present, they die out over time. If I continue the evolution and take a Fourier transform of the field for the window from 100-300 fs, the spectrum transforms to that depicted in Figure 4.2(b). The blueshifted peak has disappeared.

This loss of shifted frequencies at long times indicate that a collection of general quantum emitters is not suitable for enhancing solar cells. The time dependence of these effects also seem to suggest that certain computational techniques that are used, such as the short-pulse method [47], may not be valid for all types of scattering calculations when examining quantum systems. This is due to the fact that the short-pulse method assumes that the field-matter interaction of a short (< 1 fs) pulse can be used to approximate the continuous field-matter interaction of quantum elements. Clearly, the short-pulse excitation method is not adequate to reproduce all the physics of this process.



(a) 0-200 fs



(b) 100-300 fs

Figure 4.2: Electric field spectra for different time windows outside a 10 nm radius nanosphere of atoms with on-resonant excitation located at a spatial position $y=3$ nm outside the nanosphere. Surface plasmons are created by illumination with a monochromatic field of $f=2.41 \times 10^{14}$ Hz and $E = 1.5 \times 10^9$ V/m. The system has degenerate energy level spacings in the x, y and z direction of 1 eV and a number density of 4×10^{27} atoms per cubic metre. (a) Frequency components that appear in the time window 0 - 200fs after the start of excitation. (b) Frequency components that appear in the time window 100 - 300fs after the start of excitation. Notice that the blue-shifted frequency components die out.

The process in which the blue shifted frequency components disappear may prove useful from a quantum control perspective. By taking these same calculations and examining the free currents and state evolution of the quantum elements as an ensemble, I find that the reason that these shifted surface plasmons died out is due to the fact that the system as a whole undergoes strong disordering due to the inter-atomic interactions present in the system. These interactions, which are neglected in many theoretical investigations [61, 48, 47], can create “directional state leakage” and can explain certain experiments, as we will see in Chapter 5.

4.3 Disorder and Directional State Leakage in Dense Quantum Ensembles

By examining the spatial distribution of free current density components ($J_\eta(\mathbf{r})$) of the previous calculation as a function of time, depicted in Fig 4.3, it becomes immediately apparent that the free currents become disordered as time goes on. This disorder appears to have an effect that is very similar to mixing and order-to-disorder phase transitions in condensed matter systems. Significant entropy in the free currents is introduced and over time, this entropy prevents the individual quantum emitters from oscillating collectively. The time-scale of this entropic onset is also much faster than what one would expect the normal spontaneous emission rates of the individual emitters ($1/\gamma_0$).

Initially, the ensemble starts off responding to the incident field in what is effectively an ordered phase; all the individual systems respond to the field by oscillating in a uniform manner. This phase is characterized by a near-uniform free current in the principle polarization direction that is anti-aligned with the incident field polarization. The spatial distribution of the free currents in directions perpendicular to the incident field polarization are characterized by weak, quadrupolar patterns. As

all the individual systems are oscillating coherently, there is a strong overall optical response that leads to the shifted spectral peaks depicted in Figure 4.2.

However, due to the build-up of electric field components perpendicular to the incident polarization, the system is quickly pushed into a disordered phase. The overall ordered pattern is lost when the system transitions into this phase; small instantaneous domains are formed that do not move in phase with one another. These two phases correspond to the two time windows; one that has a blueshifted frequency and one that does not.

Another interesting thing to note is that, regardless of the level of order, the free currents in the principle polarization direction are all anti-aligned with the polarization incident field (in Figure 4.3 they are all positive). This creates a non-zero sum in the total polarization that allows the system, even when disordered, to respond to the incident field with a net dipole. This behaviour shows that in the steady-state limit, this type of system can act like a classical material with an internal net dipole moment. This is the expected macroscopic behaviour of a classical dielectric material.

This directional state leakage and the onset of the disordered phase creates three effective regimes (order, transition and disordered) for the scattering behaviour of these systems. This can lead to very different scattering behaviour between pulsed excitations and continuous wave excitation situations. Fig 4.4 illustrates this regime change qualitatively.

Furthermore, we can look at the spatially-averaged ensemble density matrix ($\bar{\rho} = \frac{1}{V} \int d^3\mathbf{r} \rho(\mathbf{r}) = \frac{1}{N} \sum_n^N \rho_n$) to get a deeper understanding about the root causes and effects of this process. By looking at the ensemble-averaged state populations for varying number densities and detunings, I see that not only does the system quickly become disordered, but also non-directly-driven states ($|e_x\rangle$ and $|e_z\rangle$) gain and retain state population. This directly shows that strong inter-atomic interactions (mediated through a mean field) with intense fields lead to a mixing of states. As all of

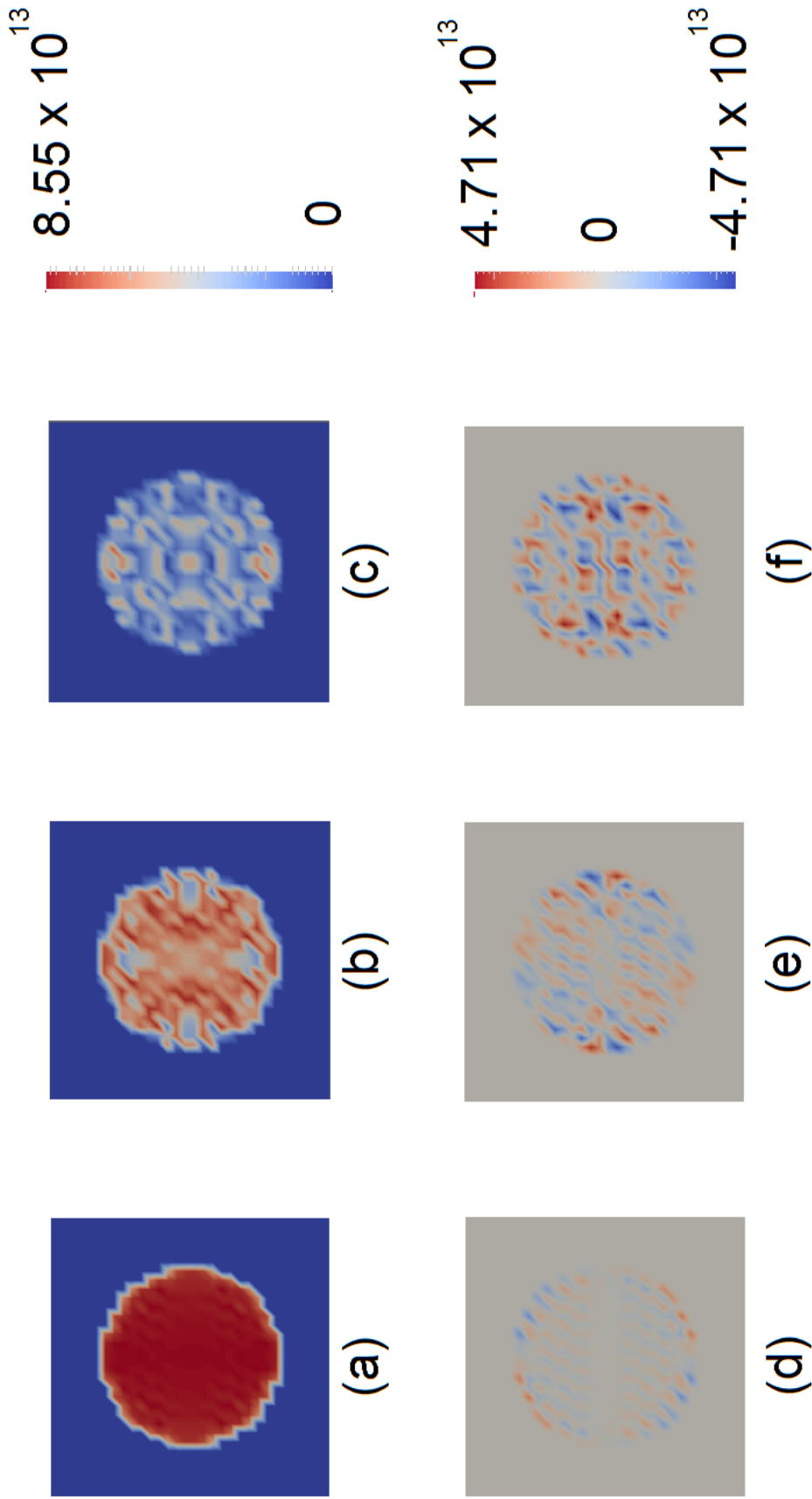


Figure 4.3: Snapshots of \hat{y} and \hat{x} direction free currents (in A/m^2) showing the ordered and disordered phases in both the incident field polarization direction (a, b, c - \hat{y}) and a non-principle direction (d, e, f - \hat{x}) in a 10 nm nanosphere of atoms at times (a/d) 10 fs, (b/e) 100 fs and (c/f) 250 fs. Populations are evaluated using a 1 nm grid and are illuminated with a constant field intensity of $E=1.5 \times 10^9$ V/m. The system has degenerate energy level spacings in the x, y and z direction of 1 eV and a number density of 4×10^{27} atoms per cubic metre. The beam is polarized in the \hat{z} direction and the snapshot bisects the nanosphere in the xy plane.

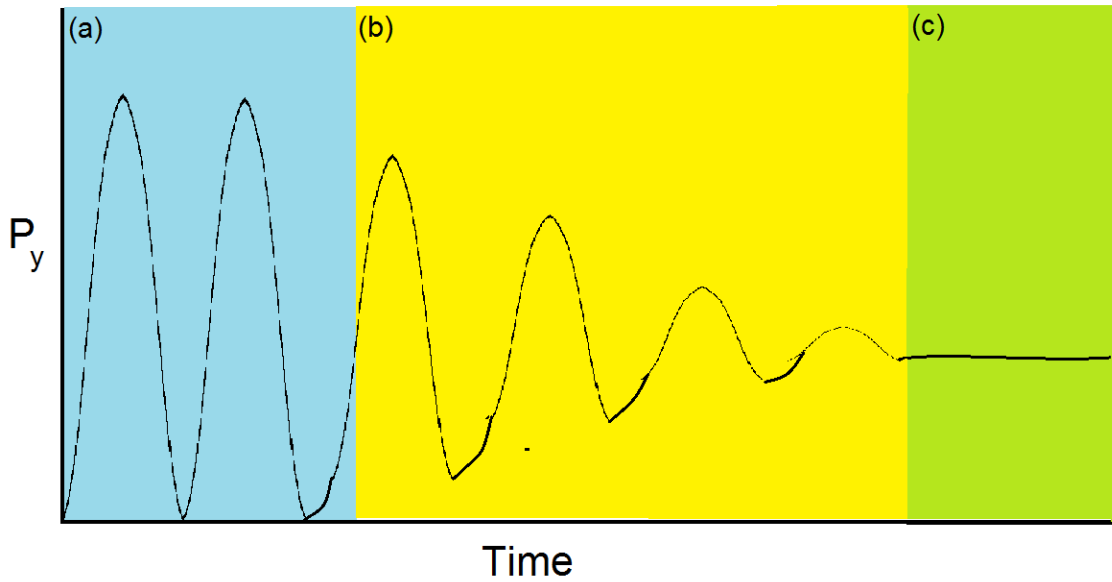


Figure 4.4: Schematic of different regimes in the evolution of a dense quantum ensemble excited principally along the \hat{y} direction. (a) In the short time regimes, the ensemble behaves in a similar fashion to a single quantum element - all individual components are in phase and display a uniform oscillation. (b) Entropy is introduced to the system, transitioning it from a uniform ordered phase to a disordered phase with multi-directional excited states. (c) This system is in a disordered phase and has all directional states excited to some degree. In this phase it operates in a similar fashion to a classical discrete dipole system as the coherent oscillations are suppressed by directional state leakage.

the ensemble state populations rapidly reach a steady-state, the ensemble-averaged coherences reduce to zero (as they represent the rate of change of the excited state populations) for all frequency components except for a small net coherence oscillating in the incident field polarization direction with the incident field frequency.

4.3.1 Effect of Increasing Ensemble Density

Figure 4.5 shows the ensemble-averaged excited state populations as a function of increasing number density. I see that increasing the overall density of atoms in the ensemble increases the rate at which disorder is added to the system. This is not unexpected as increasing the number density of quantum emitters increases the amount of inter-atomic interactions.

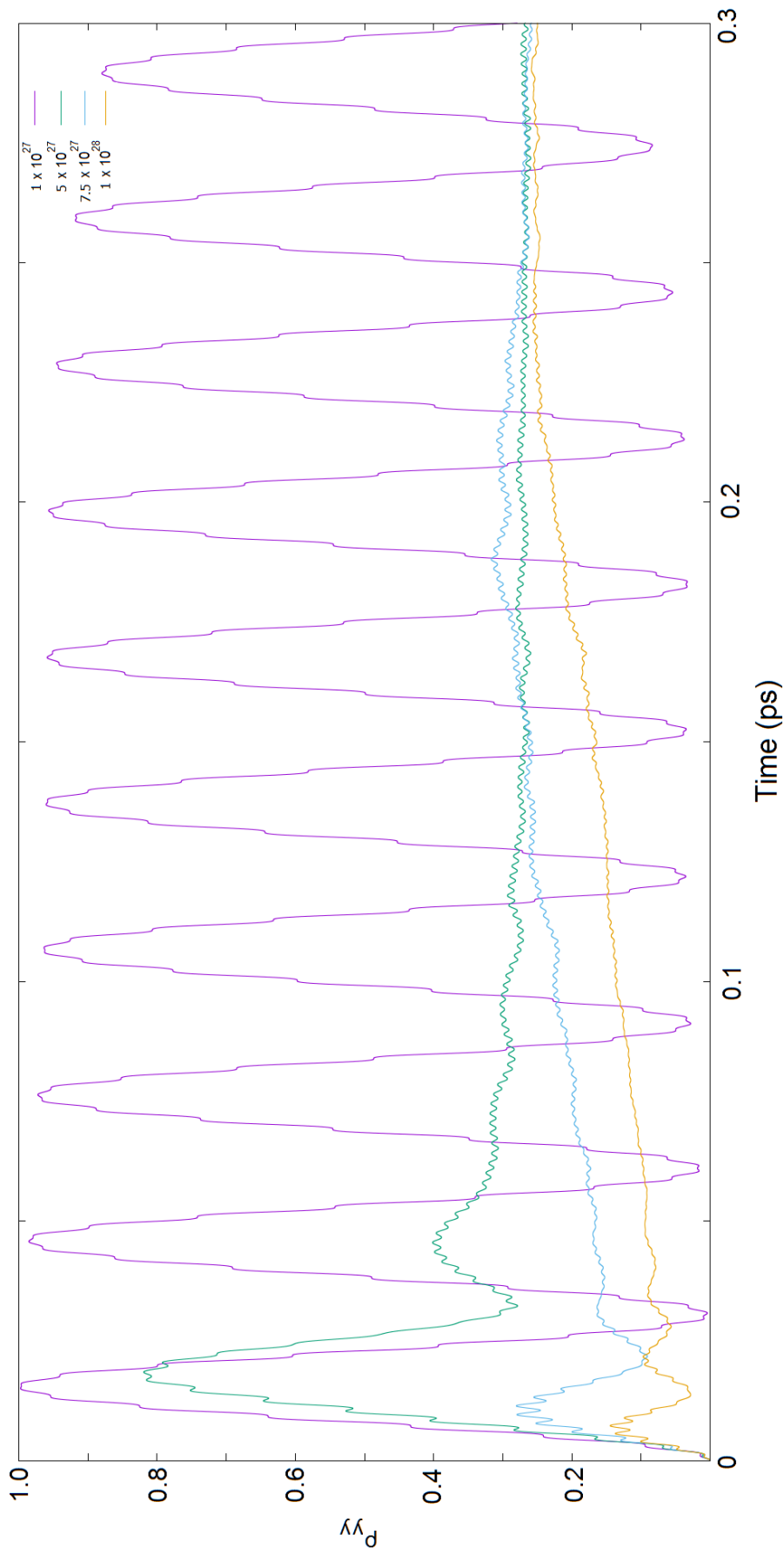
4.3.2 Effect of Changing the Incident Field Frequency

Figures 4.6, and 4.7 show that changing the incident frequency also does not affect this phenomenon much. It is interesting to note that changing the detuning does not symmetrically affect the amount of state population that reaches the excited state. This asymmetry is most likely related to the shift in local field frequencies predicted by the Lorentz-Lorenz shift.

4.3.3 Consequences of the Onset of the Disordered State

Regardless, this disorder-onset and state leakage effect demonstrates the insufficiency of uni-directional state-bases when dealing with dense quantum systems. Treating these systems as confined to excite along certain directions, such as in [48] and [47], can lead to overestimates in their long-term coherent behaviours at high densities.

If the inter-atomic interactions are strong enough (the rate of inter-atomic interactions significantly exceeds the spontaneous decay rates), state population will be



$$(a) P_x = |e_{y'}\rangle \langle e_{y'}|$$

Figure 4.5: Spatially averaged excited state populations in the \hat{x} , \hat{y} and \hat{z} directions for a 10 nm radius nanosphere of atoms with various number densities. Populations are evaluated using a 1 nm grid and are illuminated with a constant field intensity of $E=1.5 \times 10^9$ V/m. The system has degenerate energy level spacings in the x, y and z direction of 1 eV.

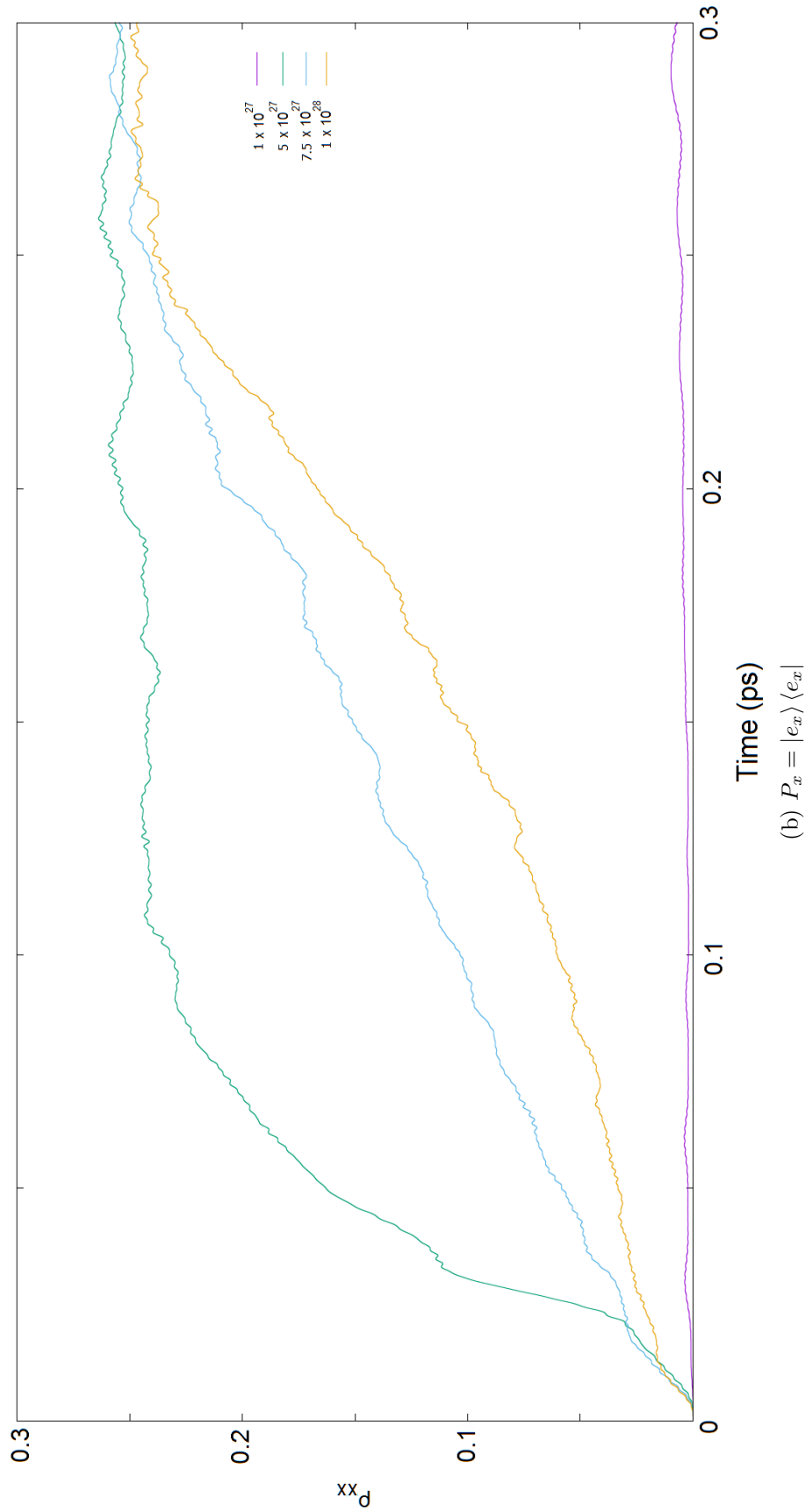


Figure 4.5: Spatially averaged excited state populations in the \hat{x} , \hat{y} and \hat{z} directions for a 10 nm radius nanosphere of atoms with various number densities. Populations are evaluated using a 1 nm grid and are illuminated with a constant field intensity of $E=1.5 \times 10^9$ V/m. The system has degenerate energy level spacings in the x, y and z direction of 1 eV.

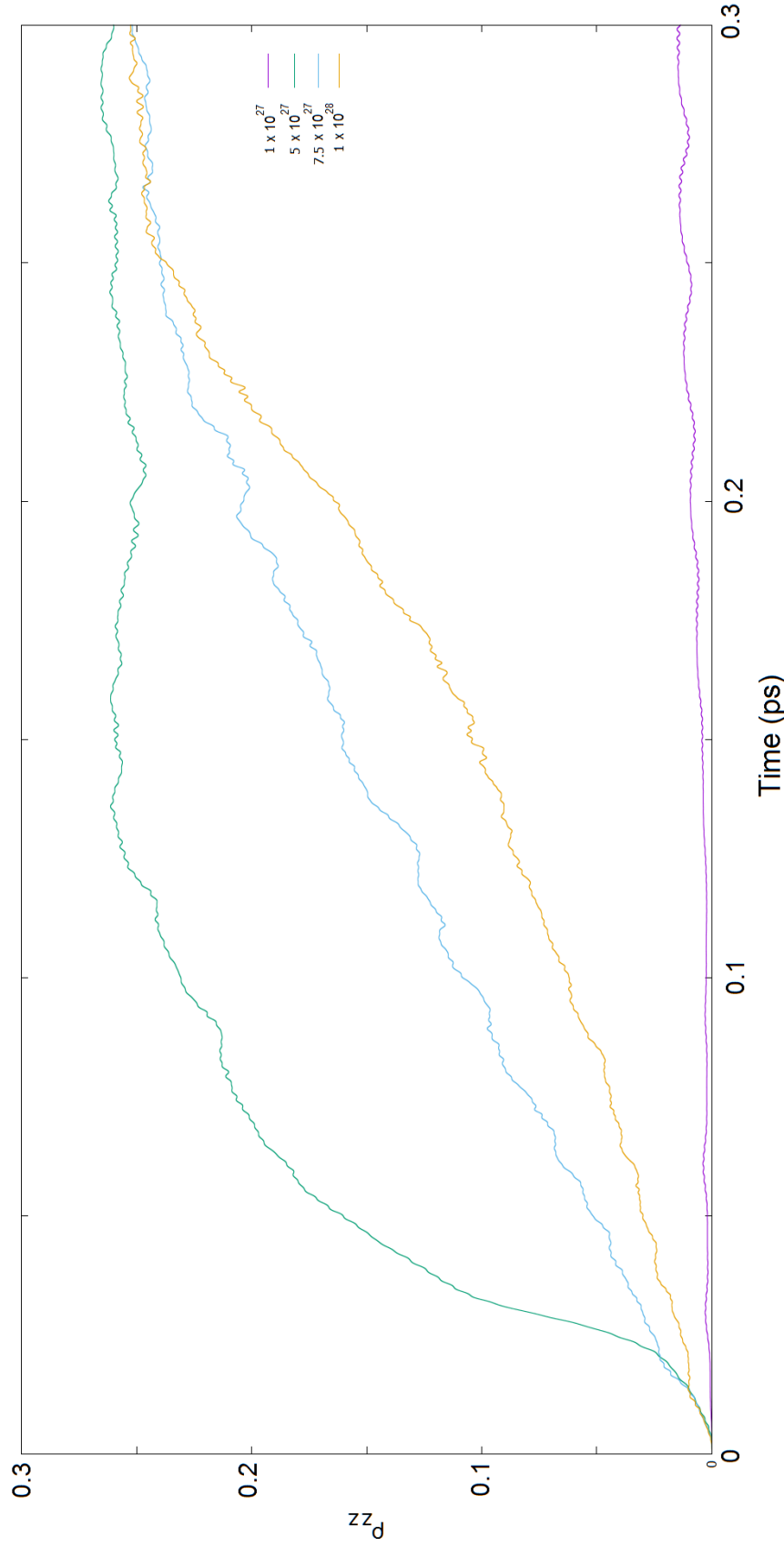
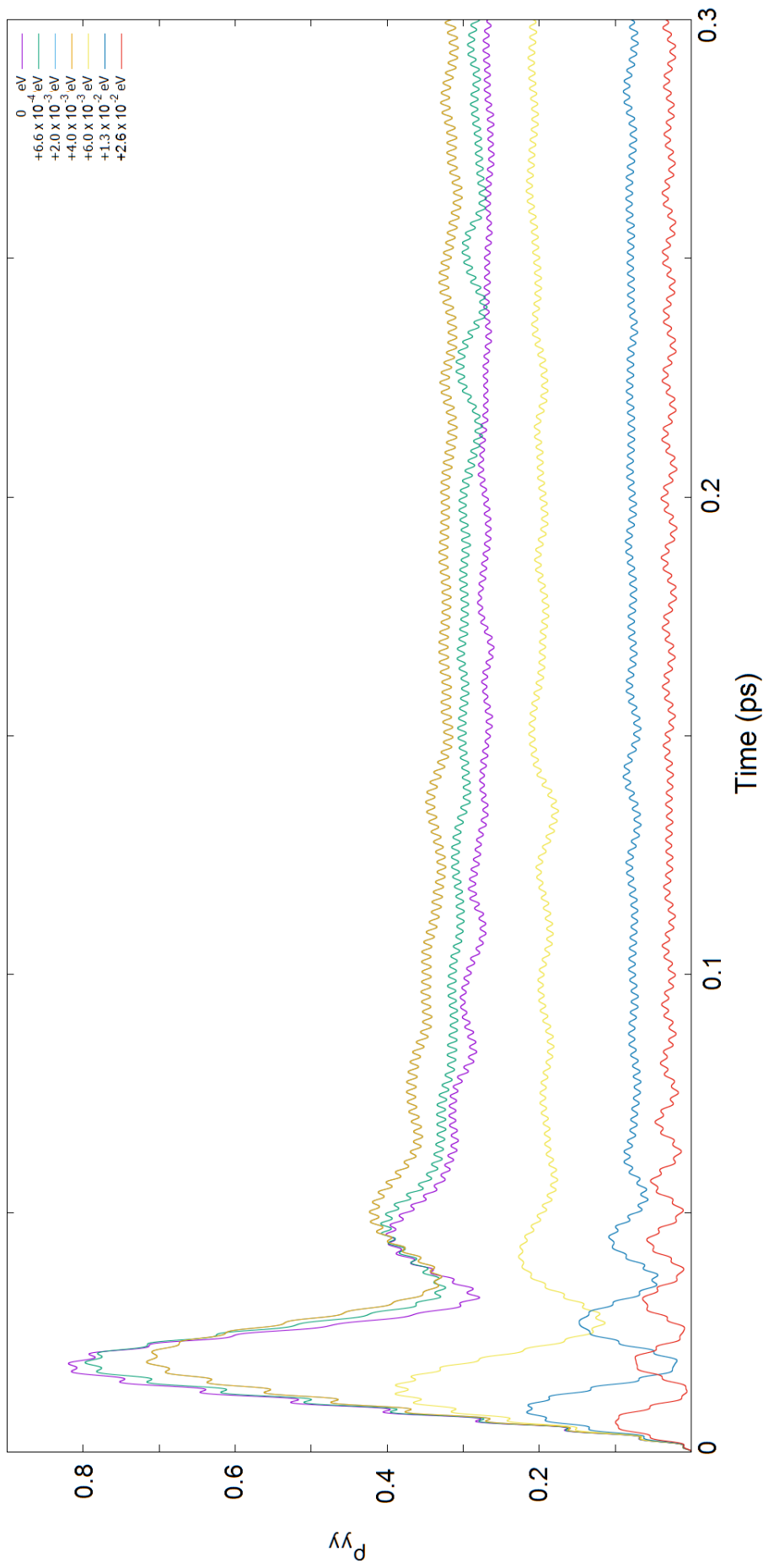


Figure 4.5: Spatially averaged excited state populations in the \hat{x} , \hat{y} and \hat{z} directions for a 10 nm radius nanosphere of atoms with various number densities. Populations are evaluated using a 1 nm grid and are illuminated with a constant field intensity of $E=1.5 \times 10^9$ V/m. The system has degenerate energy level spacings in the x, y and z direction of 1 eV.



$$(a) P_x = |e_y\rangle \langle e_y|$$

Figure 4.6: Spatially averaged excited state populations in the \hat{x} , \hat{y} and \hat{z} directions for a 10 nm radius nanosphere of atoms with lower energy off-resonant excitation. Populations are evaluated using a 1 nm grid and are illuminated with a constant field intensity of $E=1.5 \times 10^9$ V/m. The system has degenerate energy level spacings in the x, y and z direction of 1 eV and a number density of 5×10^{27} atoms per cubic metre.

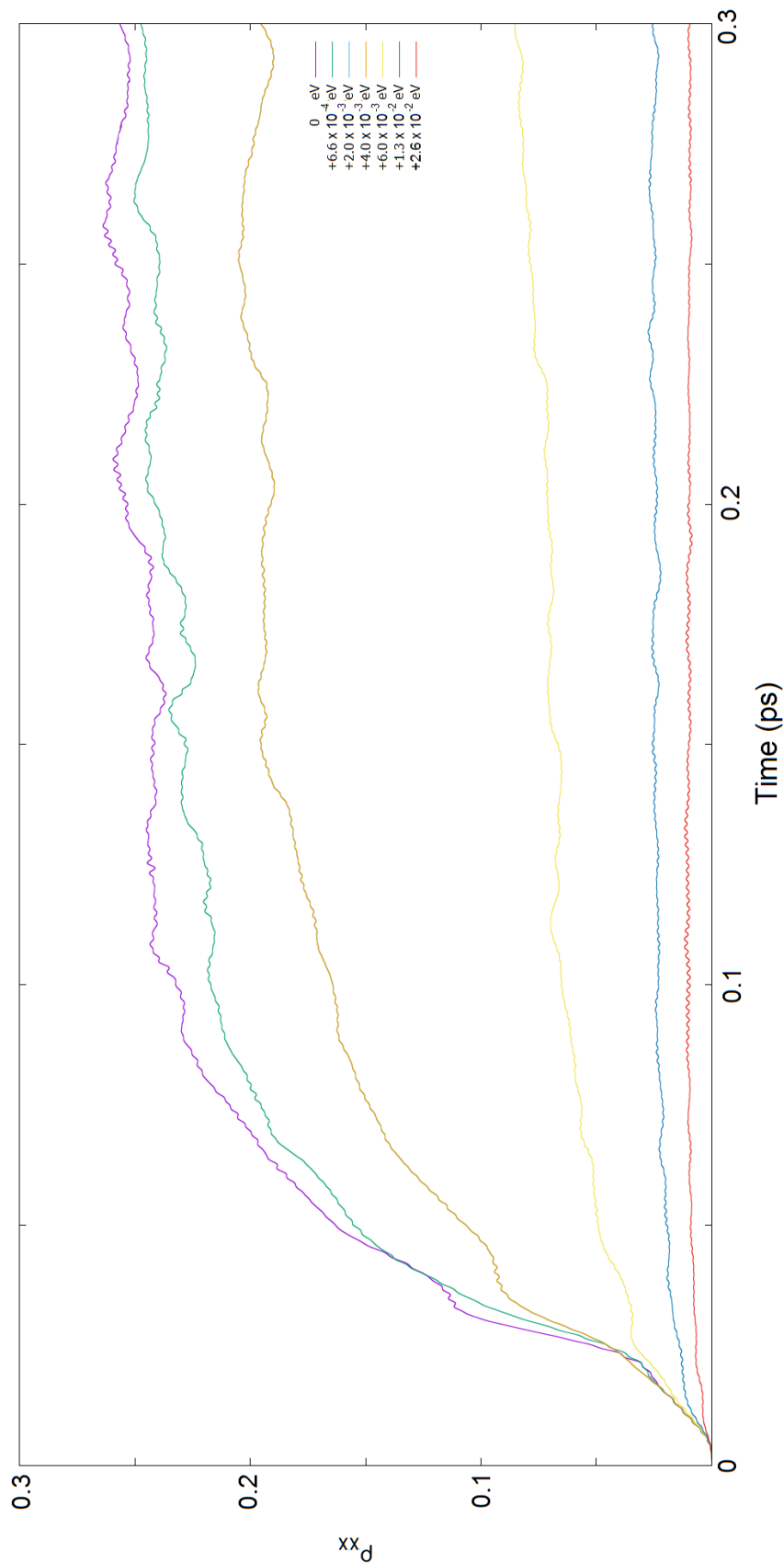


Figure 4.6: Spatially averaged excited state populations in the \hat{x} , \hat{y} and \hat{z} directions for a 10 nm radius nanosphere of atoms with lower energy off-resonant excitation. Populations are evaluated using a 1 nm grid and are illuminated with a constant field intensity of $E=1.5 \times 10^9$ V/m. The system has degenerate energy level spacings in the x, y and z direction of 1 eV and a number density of 5×10^{27} atoms per cubic metre.

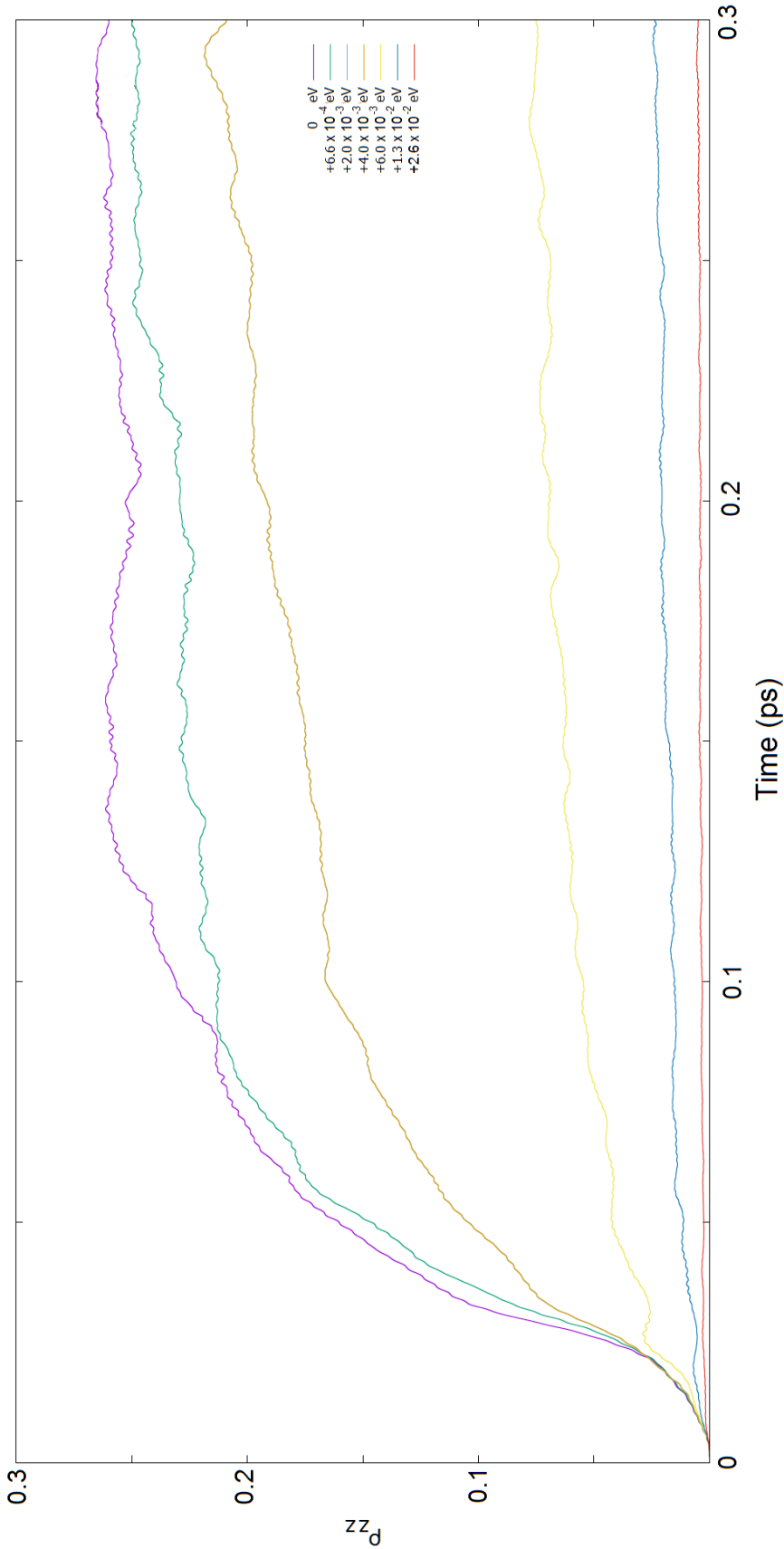


Figure 4.6: Spatially averaged excited state populations in the \hat{x} , \hat{y} and \hat{z} directions for a 10 nm radius nanosphere of atoms with lower energy off-resonant excitation. Populations are evaluated using a 1 nm grid and are illuminated with a constant field intensity of $E=1.5 \times 10^9$ V/m. The system has degenerate energy level spacings in the x, y and z direction of 1 eV and a number density of 5×10^{27} atoms per cubic metre.

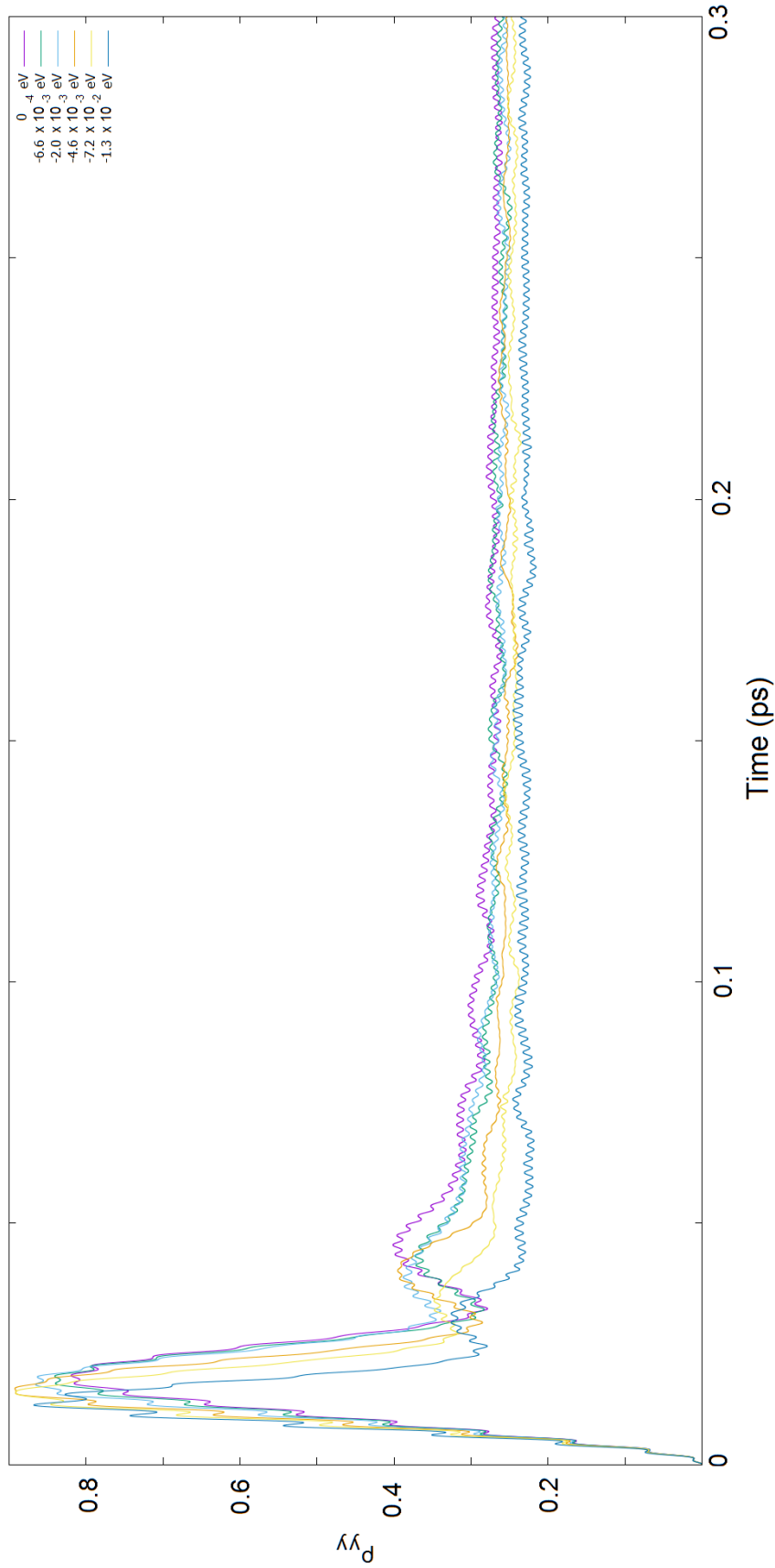


Figure 4.7: Spatially averaged excited state populations in the \hat{x} , \hat{y} and \hat{z} directions for a 10 nm radius nanosphere of atoms with higher energy off-resonant excitation. Populations are evaluated using a 1 nm grid and are illuminated with a constant field intensity of $E=1.5 \times 10^9$ V/m. The system has degenerate energy level spacings in the x, y and z direction of 1 eV and a number density of 5×10^{27} atoms per cubic metre.

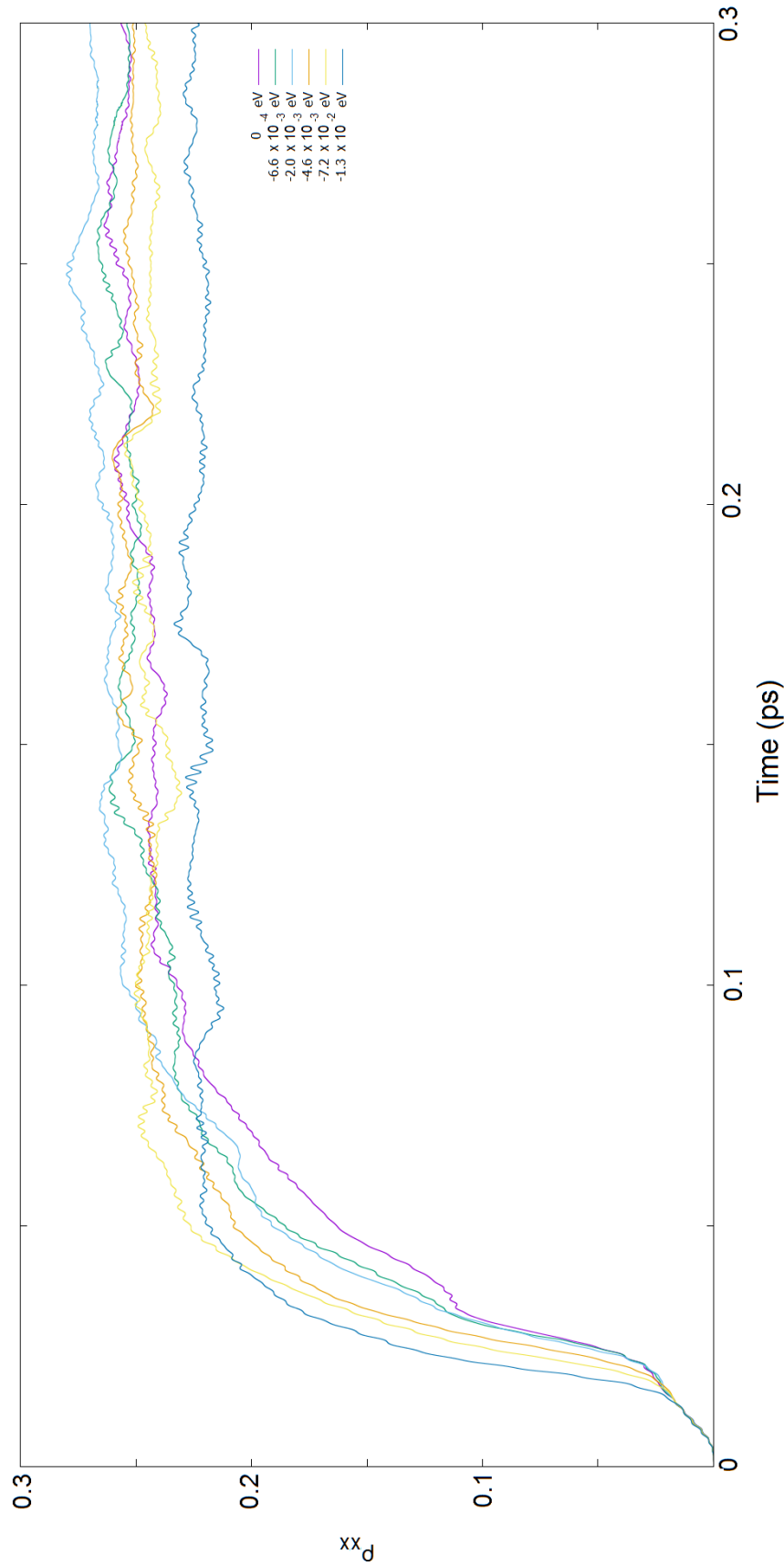
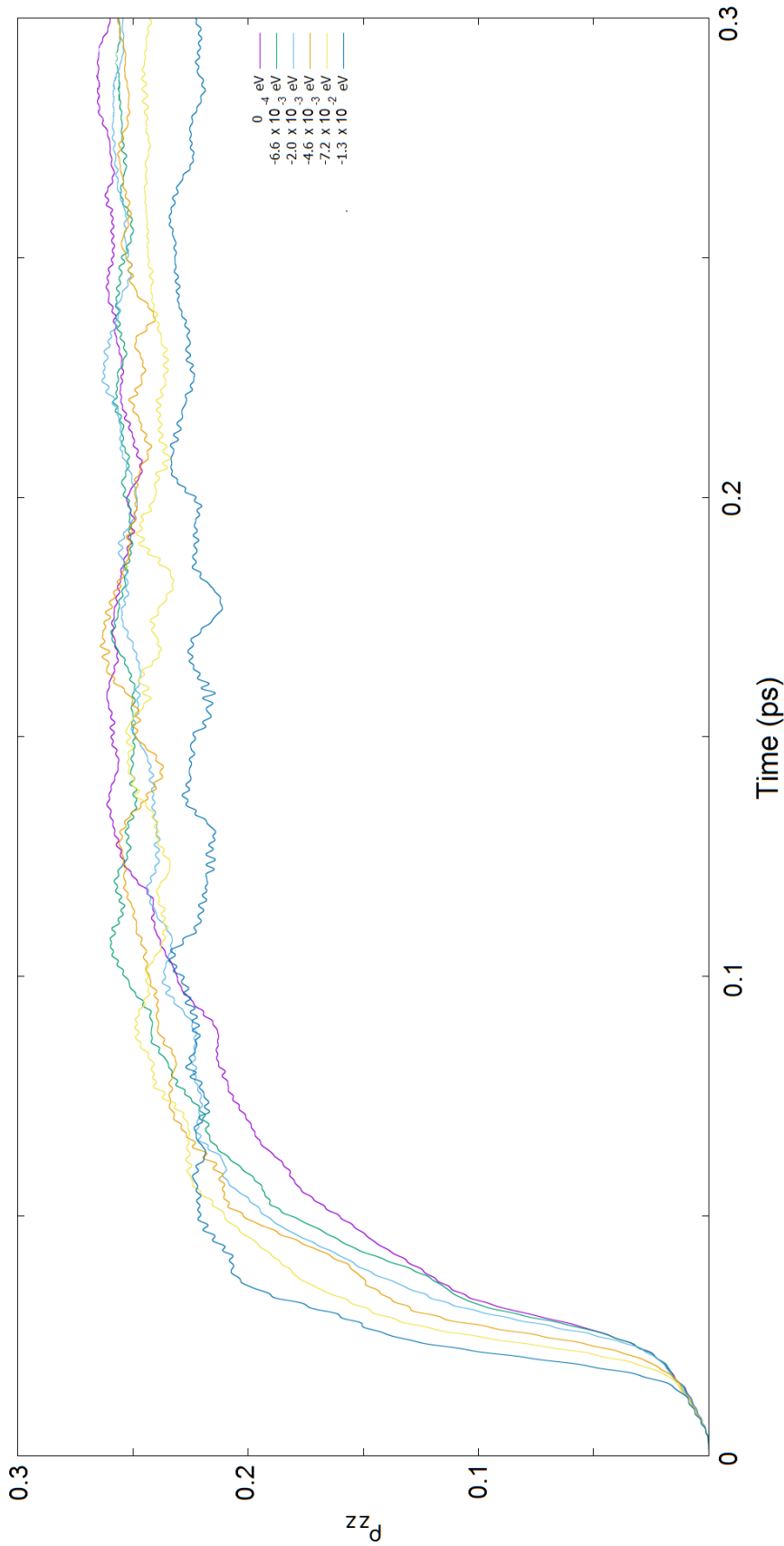


Figure 4.7: Spatially averaged excited state populations in the \hat{x} , \hat{y} and \hat{z} directions for a 10 nm radius nanosphere of atoms with higher energy off-resonant excitation. Populations are evaluated using a 1 nm grid and are illuminated with a constant field intensity of $E=1.5 \times 10^9$ V/m. The system has degenerate energy level spacings in the x, y and z direction of 1 eV and a number density of 5×10^{27} atoms per cubic metre.



$$(c) P_x = |e_z\rangle \langle e_z|$$

Figure 4.7: Spatially averaged excited state populations in the \hat{x} , \hat{y} and \hat{z} directions for a 10 nm radius nanosphere of atoms with higher energy off-resonant excitation. Populations are evaluated using a 1 nm grid and are illuminated with a constant field intensity of $E=1.5 \times 10^9$ V/m. The system has degenerate energy level spacings in the x, y and z direction of 1 eV and a number density of 5×10^{27} atoms per cubic metre.

constantly built up in non-principal directional states. This eventually leads to a significant amount of state population being retained in all direction states regardless of incident field intensities.

This retention has the effect of creating a strong “effective ensemble disorder-onset rate” in a similar fashion to that of spontaneous decay in a single quantum system. When examining the excited state population that lies along the incident polarization axis, it appears to quickly reach a steady-state. Once this happens, the incident field no longer significantly excites net changes in the average state populations and the system behaves like a classical dipole. This disorder is purely an ensemble effect; the local purity of individual coarse grains remains close to unity on this time-scale as the individual spontaneous emission rate is low (2.95×10^6 Hz).

For most cases, the final steady, disordered state that the ensemble reaches is close to the maximally entropic state. This disordered state has an approximate ensemble density matrix,

$$\begin{pmatrix} \bar{\rho}_{gg} & \bar{\rho}_{gx} & \bar{\rho}_{gy} & \bar{\rho}_{gz} \\ \bar{\rho}_{xg} & \bar{\rho}_{xx} & \bar{\rho}_{xy} & \bar{\rho}_{xz} \\ \bar{\rho}_{yg} & \bar{\rho}_{yx} & \bar{\rho}_{yy} & \bar{\rho}_{yz} \\ \bar{\rho}_{zg} & \bar{\rho}_{zx} & \bar{\rho}_{zy} & \bar{\rho}_{zz} \end{pmatrix} \approx \begin{pmatrix} \frac{1}{4} & 0 & 0 & 0 \\ 0 & \frac{1}{4} & 0 & 0 \\ 0 & 0 & \frac{1}{4} & 0 \\ 0 & 0 & 0 & \frac{1}{4} \end{pmatrix}, \quad (4.10)$$

which has a very low overall purity ($\approx \frac{1}{4}$).

4.3.4 Quantifying Disorder and Directional State Leakage in Dense Quantum Systems

Upon cursory inspection, this state leakage and disorder appears to affect the ensemble in a similar fashion to typical spontaneous decay and decoherence in single quantum systems. This is not surprising because both single-system decay/decoherence and disorder/state leakage prevent us from determining the exact state of the overall

system in question.

Just as the spontaneous emission rate of an individual quantum system tells us how long the system can remain viable as a qubit, the effective disorder-onset rate of the system tells us how long true quantum behaviour stays relevant in the ensemble. Such a measure can provide us with a lot of insight of how these systems behave and their suitability for quantum information and optical processes. This rate may be an effective way to quickly identify suitable candidate materials for nanoscale, solid-state qubits. This disorder-onset rate also allows us to assess unusual properties that can arise in bulk materials when they interact with high intensity, pulsed fields.

For the simplest interpretation, I approximated this effective disorder-onset (loss of ability to control the quantum state) by monitoring ρ_{yy} , the ensemble-averaged excited state density in the incident field polarization direction as a function of time. I then compared this population oscillation to the expected functional form of a single driven two-level quantum system and extracted the effective damping rate as a fitting parameter. While this method does not explicitly explain any of the specific, underlying physical processes involved, it provides a reasonably accurate measure of the approximate total disorder-onset rate.

Under continuous excitation, a single two-level system with spontaneous emission should just show a damped Rabi oscillation, if the high frequency, incident field frequency terms are ignored as they are in the rotating-wave approximation. This gives the driven excited state population the form:

$$\rho_{ee} = a \exp(-\gamma_{ens}t) \cos(\Omega t) + b, \quad (4.11)$$

where a and b are dimensionless constants, γ_{ens} is the damping rate of the driven excited state (\hat{y}) and Ω is the Rabi frequency that is proportional to the electric field amplitude.

For a system consisting of an ensemble of quantum systems driven by a \hat{y} polarized

Table 4.1: Disorder-Onset Rate Coefficients

Density (m^{-3})	γ_{ens} (Hz)	g (Hz)
1×10^{27}	6.243×10^{11}	8.983×10^{11}
2.5×10^{27}	1.455×10^{13}	6.173×10^{12}
4×10^{27}	3.555×10^{13}	1.845×10^{13}
5×10^{27}	5.072×10^{13}	2.637×10^{13}
7.5×10^{27}	5.305×10^{13}	9.193×10^{12}
1×10^{28}	5.194×10^{13}	1.475×10^{12}

field, the excited state density is fit better by the function,

$$\rho_{ey,ey} = a \exp(-\gamma_{ens}t) \cos(\Omega t) + b + c \exp(-gt). \quad (4.12)$$

For this function, the extra term ($c \exp(-gt)$) has been included to account for the loss of population from the excited state $|e_y\rangle$ due to the non-zero steady-state population that is built up in the \hat{z} and \hat{x} directional states. That is, g represents the rate at which state population “leaks” from the $|e_y\rangle$ state to $|e_x\rangle$ and $|e_z\rangle$ excited states. At very high number density, the damping rate γ_{ens} becomes so large that the $|e_y\rangle$ state cannot be significantly populated, so the “leakage” starts to disappear. A table summarizing the disorder-onset and state leakage fitted frequencies can be found in Table 4.1 and the full fits for all constants with errors can be found in Appendix F.

By fitting these parameters, I first noticed that in dense ensembles, the onset of disorder in denser systems is largely dominated by γ_{ens} . Therefore I chose to focus on the behaviour of γ_{ens} as a function of number density (N_a). This relationship is plotted below in Figure 4.8 for a dense ensemble driven with high intensity fields ($\Omega \gg \gamma_0$). From this figure it is fairly clear that a strongly driven, dense ensemble experiences a fast (compared to normal spontaneous emission $\gamma_0 = 2.95 \times 10^6$ Hz) onset of disorder as the density of atoms approaches solid density ($1 \times 10^{28} m^{-3}$). This indicates that any quantum control schemes that deal with dense collections of atoms

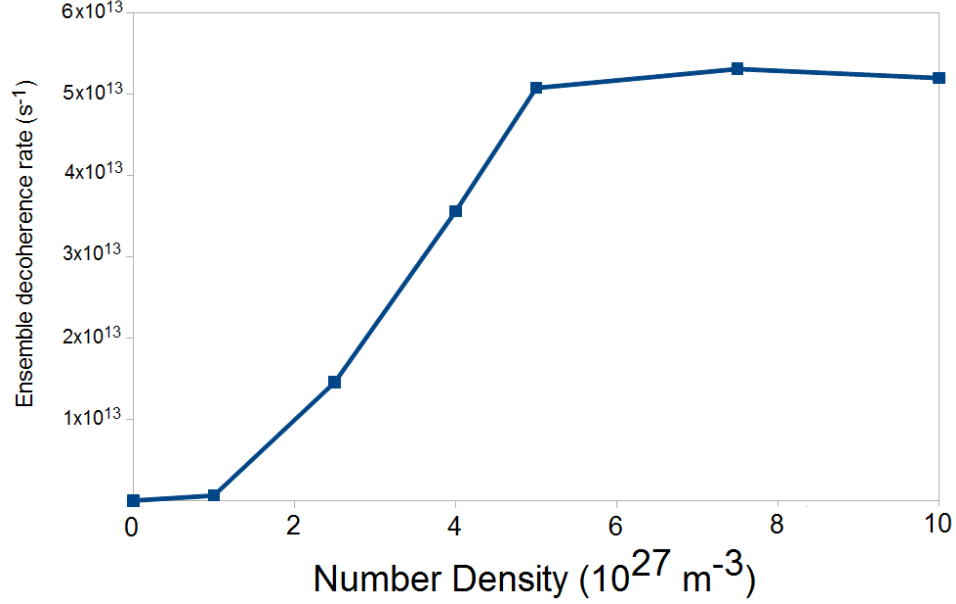


Figure 4.8: Effective ensemble decay rates (γ_{ens}) for a 10 nm radius nanosphere of atoms with varying number density (N_a). Populations are evaluated using a 1 nm grid and are illuminated with a constant field intensity of $E=1.5 \times 10^9 \text{ V/m}$. The system has degenerate energy level spacings in the x, y and z direction of 1 eV. The base decay rate for the individual quantum systems is $2.6 \times 10^6 \text{ s}^{-1}$

should not use short pulse methods and/or reduced basis sets that ignore directional states unless they are driven by extremely rapid pulses or have a low number density.

The overall shape of these dependencies is nonlinear and although it increases at low densities, the disorder-onset rate slows down at high intensities and converges to a saturation value. This behaviour appears to be best described by a saturation curve, similar to that in Fermi statistics. This takes the form of the logistic function [108] with:

$$\gamma_{ens} = \frac{L}{1 + \exp(-k(x - a))} \quad (4.13)$$

where L is the saturation point, k is a rate constant, x is the number density and a is the inflection point. This saturation curve is typically used in evolutionary systems in which there is a competition between different processes. In this particular ensemble system, there is a competition in which the incident field frequency is trying to force

Table 4.2: Saturation Curve Parameters for Varying Intensity

Intensity (V/m)	L (Hz)	a (m^{-3})	k (m^3)
1.5×10^9	5.316×10^{13}	3.337×10^{27}	1.353×10^{-27}
7.5×10^8	3.055×10^{13}	1.762×10^{27}	2.286×10^{-27}

the ensemble to oscillate coherently and the disordering (i.e. the mean field mediated inter-atomic interactions) is trying to prevent this coherent oscillation.

An example of this fit can be seen below in Figure 4.9 for the same system as in Figure 4.8 but driven at a reduced intensity. By comparing it to the situation in Fig. 4.8, one conclusion that can be easily drawn from such a fit is that, as the intensity of the incident light is reduced, the saturation point (L) of the disorder-onset rate also decreases. This is due to the fact that at lower intensities, the quantum dipoles do not have as strong of an inter-atomic interaction since they are unable to populate their excited states as well as they could at higher intensities. Therefore the disordered state is reached at lower number densities.

A table of these fitting parameters for both intensities can be found in Table 4.2 and the full fits for all constants with errors can be found in Appendix F.

This dependence of the overall disorder-onset rate on the incident driving intensity indicates that for strongly-driven, dense quantum systems, the disorder-onset rate is dependent on the density matrix and therefore is time-dependent. For dense collections of systems, it is necessary to determine a new system model with ensemble decoherence rates that are determined by using the state of the system itself.

4.4 Summary

In this chapter, I have examined the behaviour of a dense ensemble of quantum emitters interacting with each other. The state of each quantum emitter evolves according to the Lindblad-Von Neumann equation. However, the evolution of the ensemble reflects not only the driving field but also the individual interactions between

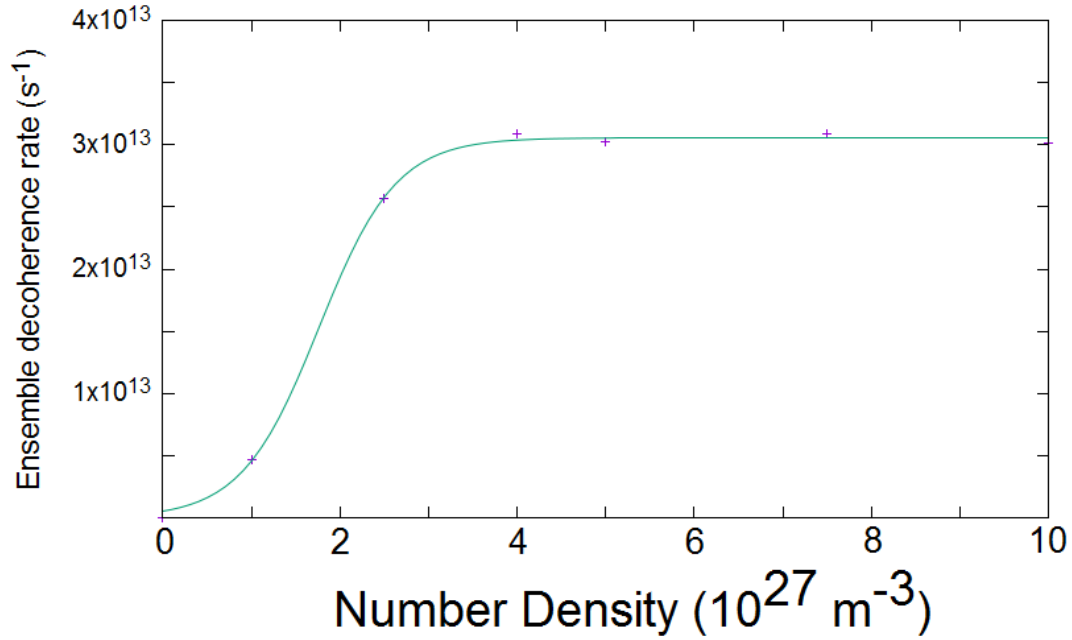


Figure 4.9: Effective ensemble decay rates (γ_{ens}) for a 10 nm radius nanosphere of atoms with varying number density (N_a). Populations are evaluated using a 1 nm grid and are illuminated with a constant field intensity of $E=7.5 \times 10^8 \text{ V/m}$. The system has degenerate energy level spacings in the x, y and z direction of 1 eV. The base decay rate for the individual quantum systems is $2.6 \times 10^6 \text{ s}^{-1}$ and a logistic function is fit to the data.

constituent elements. In this simulation, the quantum elements serve as each others' environment.

To study this system, I have implemented a coarse-grained, mean field method in which the Lindblad-Von Neumann equation is used in conjunction with a numerical solution to Maxwell's equations. In addition to combining these two well-known methodologies together, I have also modified the typical calculation for decay enhancement to work in a time-domain picture as opposed to a frequency-domain picture. In order to correctly model the excitation of the quantum elements in 3D due to spontaneous emission from nearby neighbours, I have implemented a multi-directional basis for the quantum state of each emitter.

When evaluating a simple collection of quantum systems undergoing continuous excitation, I noticed that there was an additional type of disorder introduced into the ensemble averaged states. This ensemble disorder-onset rate reflects the effect of interactions between atoms and, as such, was relatively rapid for dense, strongly-interacting systems.

The presence of this disorder is immediately significant as it set an effective time limit for quantum optical effects. It also serves as a limit for theoretical techniques such as the short-pulse method and simplified basis sets; assuming these techniques are valid over a large time-scale may lead to overestimates of coherent effects. I have quantified this time limit as an empirical "effective disorder-onset rate" for strongly driven systems as a function of number density (which directly correlates to the interaction strength between quantum emitters).

Chapter 5

Modelling Dense Ensemble

Dynamics with Single Particle

Techniques

The appearance of an effective overall disorder-onset rate in dense quantum ensembles complicates understanding their behaviour. Although I have provided an estimate of the severity of this disorder on dense ensemble dynamics, the overall empirical fitting parameters in the previous chapter do not provide a clear enough picture of the underlying physical processes involved. Therefore, I felt it would be beneficial to see if I could find a model that described the dense ensemble behaviour with a modified single-particle evolution scheme. If such a method were to exist, it would greatly reduce the computational time involved in investigating these systems and it would also provide further understanding to what underlying processes cause this evolution. Understanding these processes would then allow one to predict how these systems will behave without needing a full, complicated numerical solution.

Examining the dynamics of a driven, nanoscale ensemble of quantum systems, one notable observation is that the evolution of the ensemble state population in the

incident field polarization direction is qualitatively similar to that of a driven two-level system with two competing decoherence mechanisms; spontaneous emission and a loss of population from the excited state parallel to the incident field polarization. Therefore I explored the possibility of modelling the behaviour of a dense ensemble with a modified, single, four-level quantum system calculation.

5.1 Dense Ensemble Quantum Control with Single Particle Dynamic Decoherence

As one views the ensemble as a single particle with directional states, the Hamiltonian is straightforward to evaluate. The ensemble-averaged excited state population in the incident field polarization direction (\hat{y}) initially has a Rabi-like oscillation and for the first peak (where there is low decoherence) this frequency is nearly identical to that of a single particle system driven at the same intensity.

The Hamiltonian of this four-level system with a ground state $|g\rangle$ and three directional excited states, $|e_x\rangle$, $|e_y\rangle$ and $|e_z\rangle$, excited by a plane wave after making the rotating wave approximation is:

$$H = \begin{pmatrix} 0 & \frac{\hbar\Omega_x}{2} & \frac{\hbar\Omega_y}{2} & \frac{\hbar\Omega_z}{2} \\ \frac{\hbar\Omega_x^*}{2} & -\Delta & 0 & 0 \\ \frac{\hbar\Omega_y^*}{2} & 0 & -\Delta & 0 \\ \frac{\hbar\Omega_z^*}{2} & 0 & 0 & -\Delta \end{pmatrix}. \quad (5.1)$$

For this Hamiltonian, the only electric field terms included is the external incident field (E_y) and a perpendicular internally scattered that is much smaller than the incident field. For the perpendicular scattered field, I assume it arises from the field of a dipole with $E_{x,z} \approx E_y \frac{\mu}{\epsilon r} \sin(\theta) \hat{\theta}$ [109]. In this case $r = \sqrt[3]{\frac{3\sqrt{8}}{4N_a\pi}}$ is the separation between diagonal nearest neighbours, $\theta = \pi/4$ is the angle between them, e is the

charge of an electron and μ is the transition dipole moment; for dense systems, this scattering magnitude is about 1-2 orders of magnitude less than the incident field.

In the ensemble, an individual quantum system can spontaneously emit radiation from the $|e_x\rangle$, $|e_y\rangle$ and $|e_z\rangle$ excited basis states. This emitted radiation can then excite either the $|g\rangle \rightarrow |e_x\rangle$, $|g\rangle \rightarrow |e_x\rangle$, or $|g\rangle \rightarrow |e_z\rangle$ transitions in nearby atoms. This process is similar to the Forster-Resonance Energy Transfer (FRET) process commonly seen in biophysics systems [21]. To model this process, decoherence couplings are added that look like optically forbidden transitions as shown in Figure 5.1.

Although these transitions look similar to spontaneous emission, they do not represent the net emission of a photon. Instead they represent the emission of a photon and the reabsorption of that photon by another transition in an adjacent atom. This makes them behave more like dephasings (δ_{ij}), as they do not emit energy from the system. A diagram of all the decoherence processes in the two-level directional state basis is provided below in Figure 5.1.

The magnitude of these decoherence rates depend on the excitation transfer between atoms, therefore, they are determined by the following process [21]. For spontaneous emission from an excited to ground state, one can define the enhancement factor,

$$M_d = \frac{\gamma_d}{\gamma_{d,free}} = \frac{Power}{Power_{free}} = \frac{Re(\mathbf{j}_d^* \cdot \mathbf{E}_{local})}{Re(\mathbf{j}_d^* \cdot \mathbf{E}_d)} = 1 + \frac{Re(\mathbf{j}_d^* \cdot \mathbf{E}_{ext})}{Re(\mathbf{j}_d^* \cdot \mathbf{E}_d)}, \quad (5.2)$$

where \mathbf{j}_d is the free current of the transition, \mathbf{E}_d is the field driving the system, \mathbf{E}_{local} is the local field at the location of the system and \mathbf{E}_{ext} is the field coming from scattering by external sources. It is important to note that $\mathbf{E}_{local} = \mathbf{E}_{ext} + \mathbf{E}_d$ and that, in the limit of a single isolated system, the decay rate will remain unchanged from the vacuum value since $\mathbf{E}_{ext} = 0$.

If the system contains many strongly interacting quantum elements, the decay rate enhancement in various directions will be a complicated function of time and

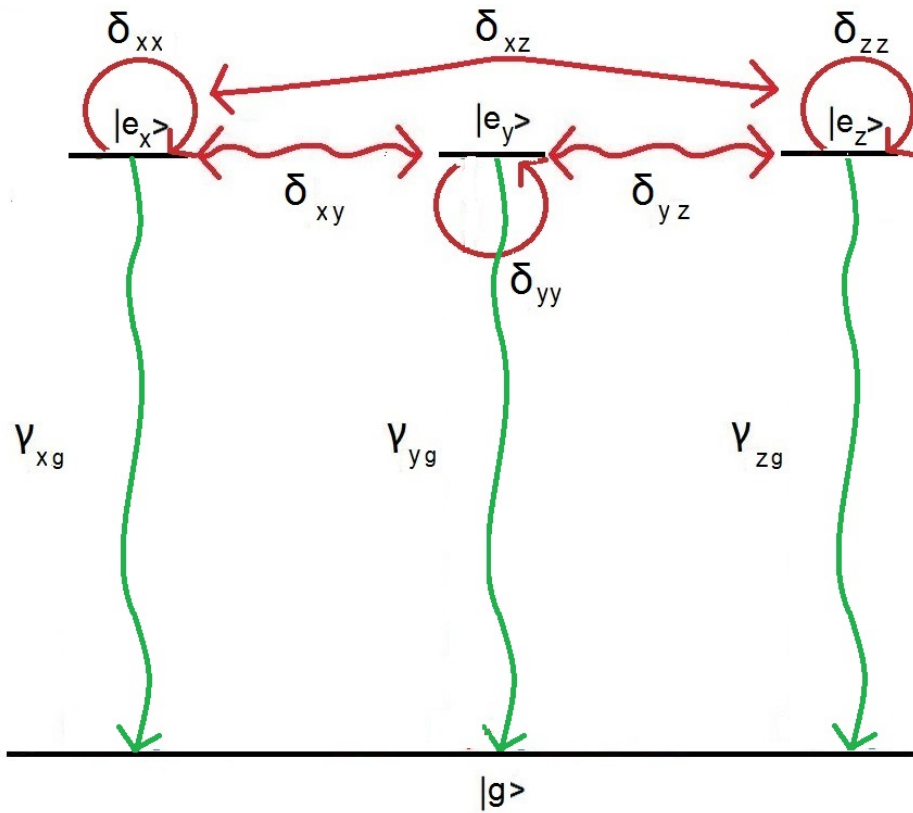


Figure 5.1: When significant dipole-dipole interactions are present in an ensemble system, it becomes possible for spontaneous emission from one excited state to excite state population from the ground state to another excited state. This allows for “spontaneous-emission” to occur between optically forbidden transitions using emission followed by absorption (δ 's in green). This results in a modified Lindblad decay scheme when examining ensemble populations. δ_{xx} , δ_{yy} and δ_{zz} reflect “parallel” transitions, whereas δ_{xy} , δ_{yz} , and δ_{xz} reflect “perpendicular” transitions. These dephasing rates do not affect the total state population, it only reduces the overall coherence of the ensemble state.

therefore cannot be easily evaluated with a single, constant, enhancement. If the transitions are viewed to acts as dipoles; however, Equation 5.2 can be simplified to,

$$\begin{aligned}\frac{\gamma}{\gamma_{free}} &= \frac{Power}{Power_{free}} = 1 + \frac{6\pi\epsilon_0}{|\mu_0|^2} \frac{1}{k^3} Im(\mu_0^* \cdot \mathbf{E}_{ext}), \\ &= 1 - \frac{6\pi\epsilon_0}{|\mu_0|^2} \frac{c^3}{\omega^4} Re(\mathbf{j}^* \cdot \mathbf{E}_{ext}).\end{aligned}\tag{5.3}$$

In a similar fashion, the decoherence rates associated with energy transfer between atomic transitions (δ_{ij}) can also be calculated. At different spatial locations these decoherences can be quantified by,

$$\frac{\delta_{i \rightarrow j}}{\gamma_0} = \frac{P_{i \rightarrow j}}{P_0},\tag{5.4}$$

where $\delta_{i \rightarrow j}$ is the rate of energy transfer from transition i in one atom to transition j in a neighbouring atom, γ_0 is the spontaneous emission rate (2.95×10^6 Hz for 1 eV) of an individual quantum emitter, $P_{i \rightarrow j}$ is the power received by the ‘‘acceptor’’ transition (j) from the field created by the ‘‘donor’’ transition (i), and P_0 is the power radiated by the acceptor atom in free space, calculated by the Larmor formula. $P_{i \rightarrow j}$ is computed by,

$$P_{i \rightarrow j} = \frac{1}{2} Re(\mathbf{j}_j^*(\mathbf{r}_j) \cdot \mathbf{E}_i(\mathbf{r}_i)),\tag{5.5}$$

where $\mathbf{j}_j^*(\mathbf{r}_j)$ is the free current of the acceptor and $\mathbf{E}_i(\mathbf{r}_i)$ is the field created by the donor.

In the limit in which there exists multiple quantum transitions in a single lattice cell, the rate of energy transfer that occurs inside sites could be analytically approximated using Equation 5.5 and the fact that the near-field contribution of a dipole is dependant on its polarization[56]:

$$\mathbf{E}_i = \frac{1}{3\epsilon_0} N_a \mu_i.\tag{5.6}$$

With these two equations in mind, if there are two, non-optically connected, degenerate transitions (i and j) then,

$$\begin{aligned}
\frac{\delta_{i \rightarrow j}}{\gamma_0} &= \frac{P_{i \rightarrow j}}{P_0} = \frac{N_a}{2P_0} \text{Re}(\mathbf{j}_j^* \cdot \frac{1}{3\epsilon_0} \boldsymbol{\mu}_i) \\
&= N_a \frac{6\pi\epsilon_0}{|\boldsymbol{\mu}_i|^2} \frac{c^3}{\omega_i^4} \text{Re}(\mathbf{j}_j^* \cdot \frac{1}{3\epsilon_0} \boldsymbol{\mu}_i) \\
&= N_a \frac{2\pi}{|\boldsymbol{\mu}_i|^2} \frac{c^3}{\omega_i^4} \text{Re}(\mathbf{j}_j^* \cdot \boldsymbol{\mu}_i)
\end{aligned} \tag{5.7}$$

The electric fields of the donor transitions are calculated as if they are dipoles with classical radiated fields [110],

$$\mathbf{E}_i(\mathbf{r}) = \frac{1}{4\pi\epsilon_0} \left(\frac{3(\mathbf{u}_i \cdot \hat{r})\hat{r} - \mathbf{u}_i}{r^3} \right). \tag{5.8}$$

Assuming that the atoms are spherically distributed two radii apart ($1/r^3 = \frac{1}{8} \frac{4\pi}{3} N_a$, for nearest neighbours) and with number density N_a this simplifies to,

$$\mathbf{E}_i(\mathbf{r}) = \frac{N_a}{24\epsilon_0} (3|\hat{u}_i|(\hat{u}_i \cdot \hat{r})\hat{r} - \hat{u}_i). \tag{5.9}$$

Combining these equations and normalizing to the power emission of a dipole this yields,

$$\frac{\delta_{i \rightarrow j}}{\gamma_0} = \frac{N_a \pi c^3}{4\omega^3} (3(\hat{u}_i \cdot \hat{r}_i)(\hat{u}_j \cdot \hat{r}_i) - \hat{u}_j \cdot \hat{u}_i) (\sqrt{\rho_{ii}\rho_{gg}}\sqrt{\rho_{jj}\rho_{gg}}), \tag{5.10}$$

where $\sqrt{\rho_{ii}\rho_{gg}}\sqrt{\rho_{jj}\rho_{gg}}$ serves as an estimate of the fraction of atoms in the ensemble that experience the $|i\rangle \rightarrow |j\rangle$ energy transfer. This term is necessary in determining the strength of \mathbf{j}_j and \mathbf{E}_i as they both depend on the how many systems in the ensemble currently experience these dipole moments. This term, $\sqrt{\rho_{ii}\rho_{gg}}\sqrt{\rho_{jj}\rho_{gg}}$, gives the decoherence rate the intensity-dependence seen in the previous chapter since the density matrix elements depend directly on the driving intensity.

For the ‘‘parallel’’ transitions (for example δ_{xx}), I use Equation 5.10 and normalize

to the power of a radiating dipole of the transition frequency ω ,

$$\frac{\delta_{i \rightarrow j}}{\gamma_0} = \frac{N_a \pi c^3}{2\omega^3} (\sqrt{\rho_{ii} \rho_{gg}} \sqrt{\rho_{jj} \rho_{gg}}). \quad (5.11)$$

For the transitions that are “perpendicular” (for example δ_{xy}), I need to use the nearest diagonal neighbour, instead of the nearest neighbour, as this diagonal neighbour is the closest lattice site in which a dipole can produce radiated fields in a perpendicular direction to its dipole moment. This involves dividing Equation 5.10 by $\frac{1}{\sqrt{8}}$ since $r' = \sqrt{2}r$ and therefore $\theta = \pi/4$. The dephasing rate of these perpendicular transitions is calculated as,

$$\frac{\gamma_{i \rightarrow j}}{\gamma_0} = \frac{3N_a \pi c^3}{16\sqrt{2}\omega^3} (\sqrt{\rho_{ii} \rho_{gg}} \sqrt{\rho_{jj} \rho_{gg}}). \quad (5.12)$$

Placing these decoherence parameters into a single particle evolution calculation yields excited state populations depicted in Figures 5.2 and 5.3. The single particle state calculation is overlaid with the ensemble-averaged calculation described in the previous chapter. When I compare the results of the single particle approximation to the full ensemble calculation, I see that there is relatively good agreement between the two methods. The two methods are not identical to within floating point error; however they are close enough to suggest that this single particle, modified-decoherence scheme captures a significant amount of the underlying physical processes involved.

The success of the effective single particle model shows that a FRET-like decoherence process takes place in a dense, driven ensemble. The full calculation required ≈ 16 cpu days of runtime; in comparison the single particle calculation required ≈ 2 cpu minutes of runtime. The strength of applying this effective model is demonstrated in the next Section.

One major limitation of this single particle model is that it assumes that the Hamiltonian can be determined by an constant incident field/dipole interaction and

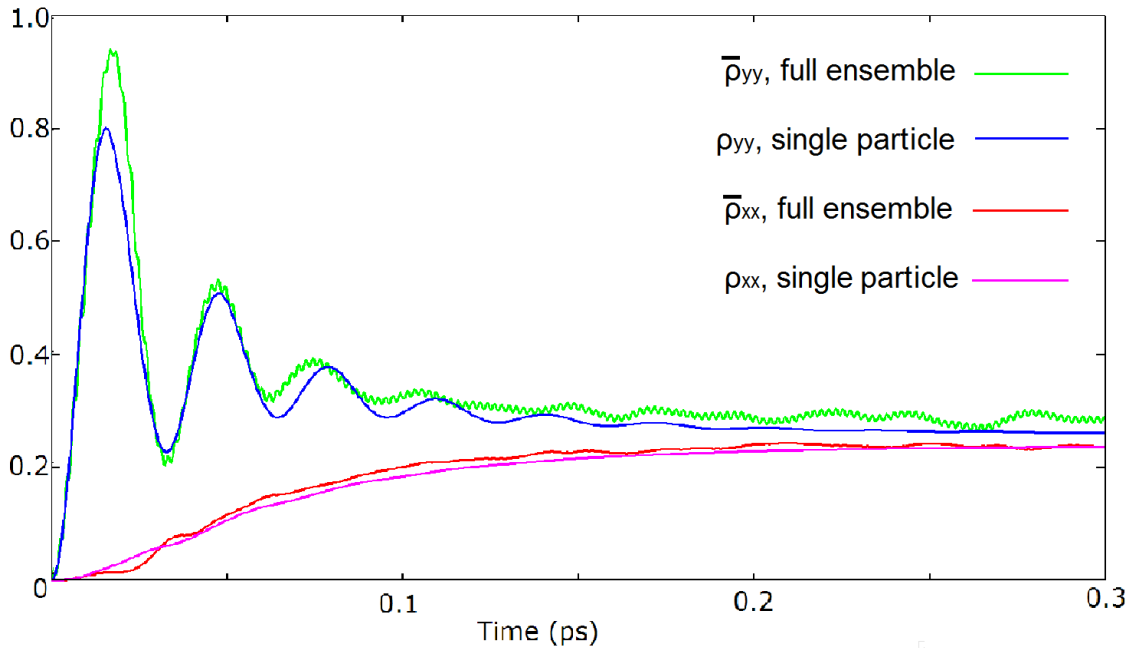


Figure 5.2: Spatially averaged excited state populations for a 10 nm radius nanosphere of atoms. Populations are evaluated using a 1 nm grid and are illuminated with a constant field intensity of $E=1.5 \times 10^9$ V/m. The system has degenerate energy level spacings in the x, y and z direction of 1 eV and a number density of 4×10^{27} atoms per cubic metre. A single particle calculation in the RWA approximation is overlaid to compare the two models.

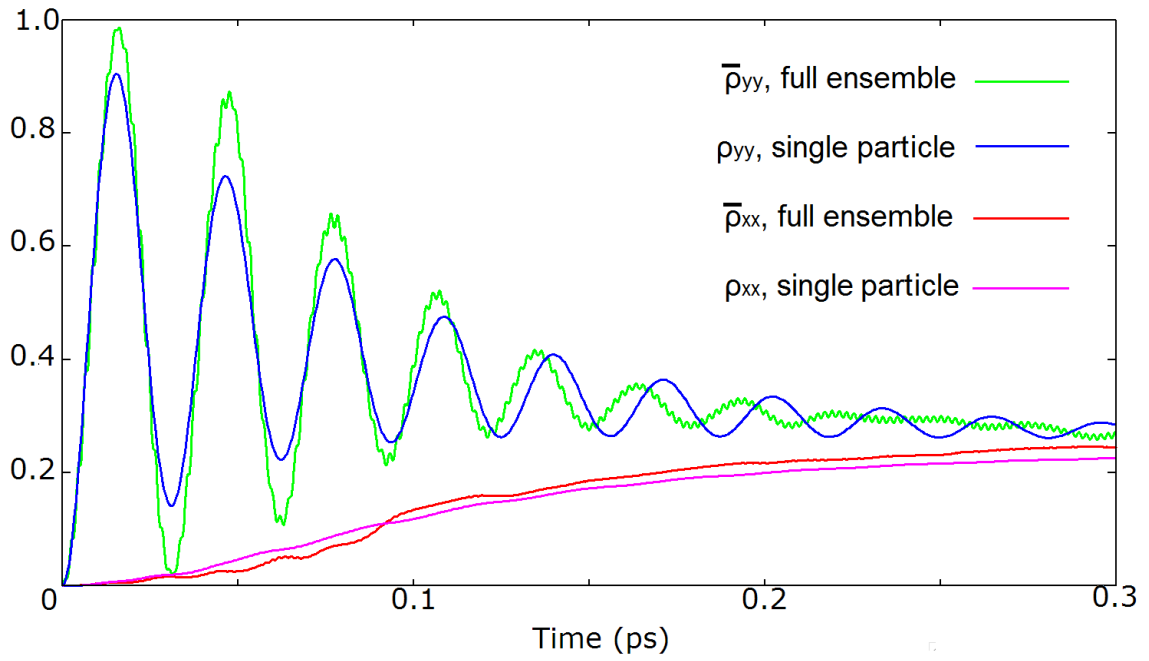


Figure 5.3: Spatially averaged excited state populations for a 10 nm radius nanosphere of atoms. Populations are evaluated using a 1 nm grid and are illuminated with a constant field intensity of $E = 1.5 \times 10^9$ V/m. The system has degenerate energy level spacings in the x, y and z direction of 1 eV and a number density of 2.5×10^{27} atoms per cubic metre. A single particle calculation in the RWA approximation is overlaid to compare the two models.

therefore does not include coherent, scattering of a field emitted by one emitter from another emitter. In reality, this Hamiltonian should also depend on the instantaneous state and overall geometry of the ensemble. Another limitation of this model is that it assumes that only the single, nearest neighbour interactions are relevant to the couplings; in truth, farther couplings and interference effects between atoms are required to increase the model’s accuracy. In future work, one could improve this model by adopting a more robust coupling geometry to account for scattered driving fields and further neighbours.

5.2 Pulsed Excitations in Dense Quantum Systems and Magnetic-Dipole Scattering

My effective single atom model that incorporates “leakage” to directional states and strong FRET-like decoherence also successfully models experiments involving ultra-fast pulsed-excitations in dense quantum systems.

In one such scattering experiment [60, 61], high-intensity, short-duration, electromagnetic pulses are scattered off water and carbon tetrachloride. The observed pattern of the scattered light led the authors to propose a theory, based on single particle, classical electromagnetic scattering, that there was magnetic dipole radiation generated. They called this phenomenon “transverse optical magnetism”.

This explanation has been challenged in the literature [63, 64, 65, 66, 67, 62] since strong magnetic interactions can be assumed to be negligible in classical electromagnetic scattering. Additionally, the fact that this effect is observed in a variety of liquids, including the highly symmetric CCl_4 (that lacks an electric dipole and quadrupole moment) leads one to look for alternative explanations for the observations.

I propose that these experiments are examples of dense quantum ensembles driven

by short pulses. Applying my effective single particle model to this problem, both the effects of the driving field as well as the spontaneously emitted fields are modelled.

In a similar fashion to the experiment in [61], a dense system ($N_a = 1E27m^{-3}$) is excited with a \hat{y} -polarized short pulse (20 fs width) propagating along the \hat{z} direction. The pulse to be intense enough to excite the system into a the \hat{y} excited state and allow it to decay. Initially the full ensemble calculation is performed for 300 fs.

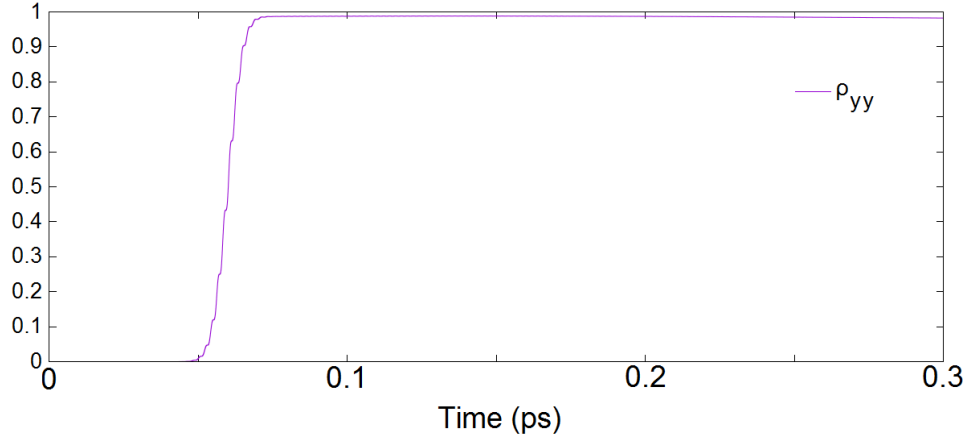
The evolution of the ensemble-averaged excited state populations for the full calculation can be seen below in Figure 5.4. Initially the system is excited by the pulse and reaches a nearly pure $|e_y\rangle$ state ($\rho_{yy} = 1$). After the pulse leaves the ensemble, the dynamics are driven by only the decoherent processes. After the pulse ends, spontaneous emission in the $|e_y\rangle$ state will populate some amount of both \hat{x} and \hat{z} excited states due to the decoherent coupling between excited states (δ 's).

These excitations are an effect that will not be seen in single particle cases as it arises purely due to atom-atom energy transfer (it disappears as $N_a \rightarrow 0$). My calculation does not involve magnetic dipole free currents since the density matrices in the directional-state representation are excited by only electric fields.

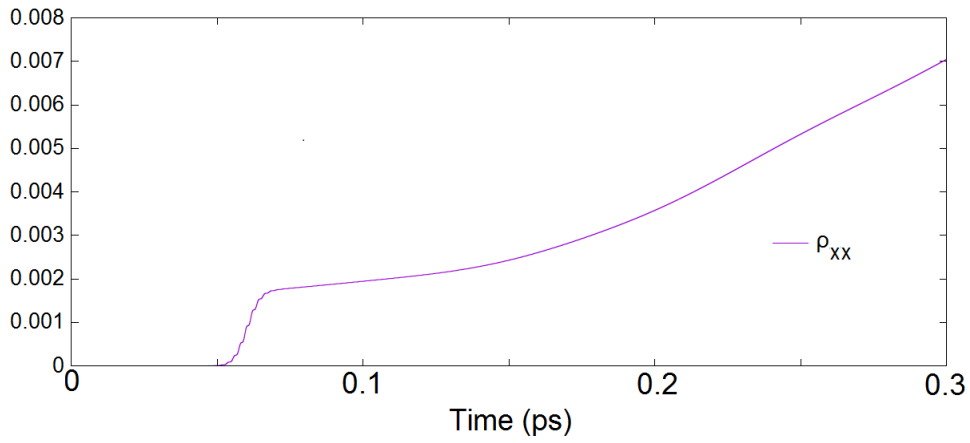
Continuing the full calculation beyond 300 fs would take a prohibitively expensive amount of computational time as the rate of change in excited state densities is lower than in previous analyses. However, if I treat the ensemble as a single particle using my model, I can estimate the behaviour of the ensemble over this longer time-scale much more efficiently. If I examine my system after the pulse, it is a purely dissipative system (with only the Lindblad term, L when in the rotating wave approximation). Therefore, I can write down the single particle evolution equations with just the dissipative FRET terms from my previous analysis. The operators take the form,

$$\sigma_{i,j}^\dagger = |j\rangle \langle i|, i \neq 0. \quad (5.13)$$

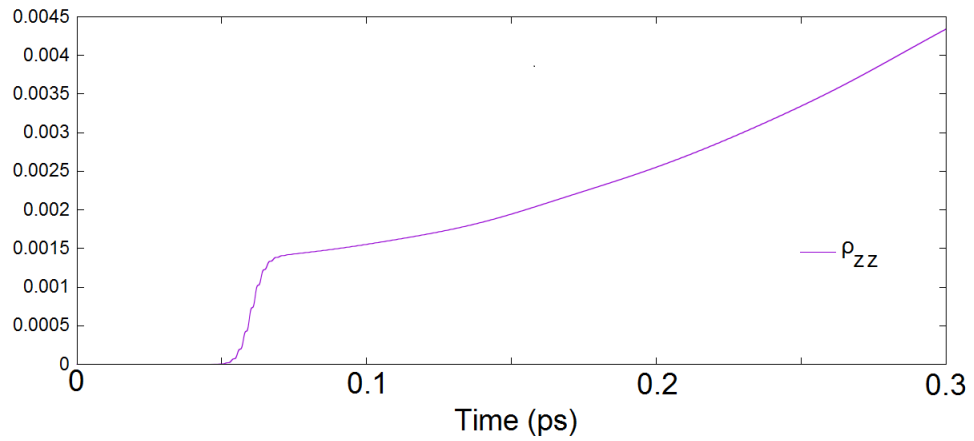
Placing this into the Lindblad superoperator,



(a) $P_y = |e_y\rangle \langle e_y|$



(b) $P_x = |e_x\rangle \langle e_x|$



(c) $P_z = |e_z\rangle \langle e_z|$

Figure 5.4: Full Ensemble Calculation: Spatially averaged excited state populations for a 10 nm radius nanosphere of an atoms with various number densities. Populations are evaluated using a 1 nm grid and are illuminated with a 20 fs width Gaussian pulse. The system has degenerate energy level spacings of 1 eV and a number density of 1×10^{27} atoms per cubic metre.

$$L(\rho) = \sum_{i,j} \frac{\gamma_{i,j}}{2} (\sigma_{i,j}^\dagger \sigma_{i,j} \rho + \rho \sigma_{i,j}^\dagger \sigma_{i,j} - 2\sigma_{i,j} \rho \sigma_{i,j}^\dagger), \quad (5.14)$$

yields, for the state populations,

$$\dot{\rho}_{xx} = -(\gamma_{xg} + \delta_{xy} + \delta_{xz})\rho_{xx} + \delta_{yx}\rho_{yy} + \delta_{zx}\rho_{zz}, \quad (5.15)$$

$$\dot{\rho}_{yy} = -(\gamma_{yg} + \delta_{yx} + \delta_{yz})\rho_{yy} + \delta_{xy}\rho_{xx} + \delta_{zy}\rho_{zz}, \quad (5.16)$$

$$\dot{\rho}_{zz} = -(\gamma_{zg} + \delta_{zy} + \delta_{zz})\rho_{zz} + \delta_{yz}\rho_{yy} + \delta_{xz}\rho_{xx}. \quad (5.17)$$

If I take these evolution equations and make the further assumption that the decay coupling between the “optically-forbidden” states is symmetric ($\delta_{ij} = \delta_{ji}$),

$$\dot{\rho}_{xx} = -\gamma_{xg}\rho_{xx} + \delta_{xy}(\rho_{yy} - \rho_{xx}) + \delta_{xz}(\rho_{zz} - \rho_{xx}), \quad (5.18)$$

$$\dot{\rho}_{yy} = -\gamma_{yg}\rho_{yy} + \delta_{xy}(\rho_{xx} - \rho_{yy}) + \delta_{yz}(\rho_{zz} - \rho_{yy}), \quad (5.19)$$

$$\dot{\rho}_{zz} = -\gamma_{zg}\rho_{zz} + \delta_{yz}(\rho_{yy} - \rho_{zz}) + \delta_{xz}(\rho_{xx} - \rho_{zz}). \quad (5.20)$$

Note that the coupling between excited states largely depends on which state currently has more state population. Using this single model, I can evaluate the long term dissipation in an ensemble of atoms.

5.2.1 Case: Decoherence Rates are Independent of State Populations

Now the simplest assumption that one can make is that these coupled decay rates are constant in time. Making this assumption, and examining the system after the pulse when it is largely in a $|e_y\rangle$ excited state ($\rho_{yy} = 1$), we are left with,

$$\dot{\rho}_{xx} = \delta_{xy}, \quad (5.21)$$

$$\dot{\rho}_{yy} = -(\gamma_{yg} + \delta_{xy} + \delta_{yz}), \quad (5.22)$$

$$\dot{\rho}_{zz} = \delta_{yz}. \quad (5.23)$$

By finding the average rate of change of excited state population in Figure 5.4 over the duration of the full ensemble calculation, I estimate the strength of the overall decay couplings. These estimates are input into the full update equations, Eq. 5.18-5.20, to predict the evolution of the ensemble state over a much larger time-scale. This results in the evolution of state populations depicted in Fig. 5.5. The overall behaviour of this system is very simple; initially the system starts in the \hat{y} excited state and decays. As ρ_{yy} is much larger than ρ_{xx} or ρ_{zz} , ρ_{xx} and ρ_{zz} quickly build up state population by absorbing energy from the spontaneous decay from state $|e_y\rangle$. Eventually ρ_{xx} and ρ_{zz} reach a steady state.

5.2.2 Case: Decoherence Rates are Modified by Excited State Populations

In addition, instead of constant couplings, I could implement the time-dependent coupling coefficients (that scale with elements of the density matrix) discussed in Section 5.1 (Eq. 5.11 and 5.12). This evolution is displayed in Figure 5.6 and is relatively similar to the constant coupling case.

One interesting thing about these simple models is that if we take the evolution shown in Fig 5.5 and find the time-averaged amount of excited state population in the ρ_{xx} , ρ_{yy} and ρ_{zz} states, we find that $\langle \rho_{xx} \rangle \approx \frac{1}{2} \langle \rho_{yy} \rangle$ and $\langle \rho_{zz} \rangle \approx \frac{1}{2} \langle \rho_{yy} \rangle$. These average excited state ratios should reflect the average amount of time-integrated free current that each excited state will emit as it decays. For a single excited state ($|e_\eta\rangle$)

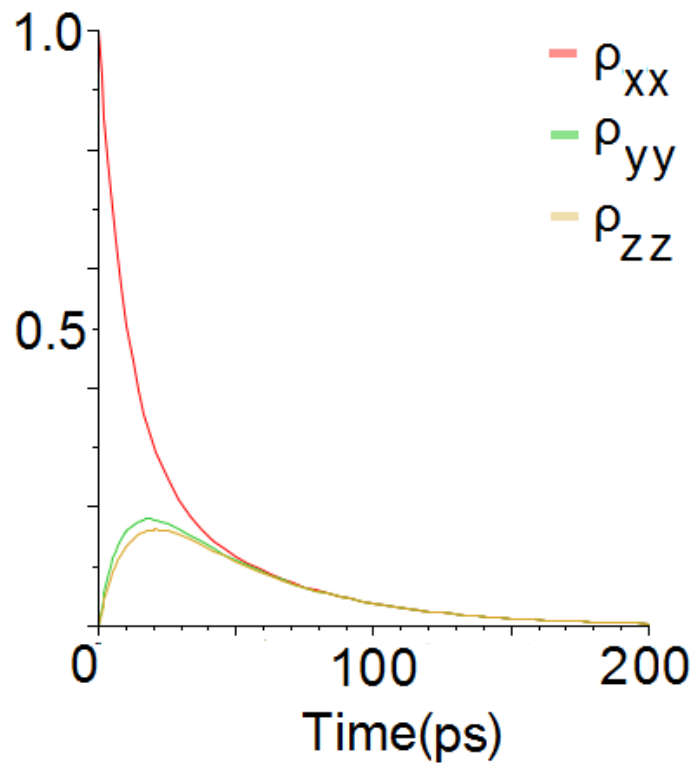


Figure 5.5: Excited state populations for a Lindblad dissipation evolution scheme with decay coupling parameters found by examining state evolution in Fig 5.4. The system evolves from an almost pure excited state and spontaneous emission from this state is able to excite other transitions. For this case coupling parameters are assumed to be constant.

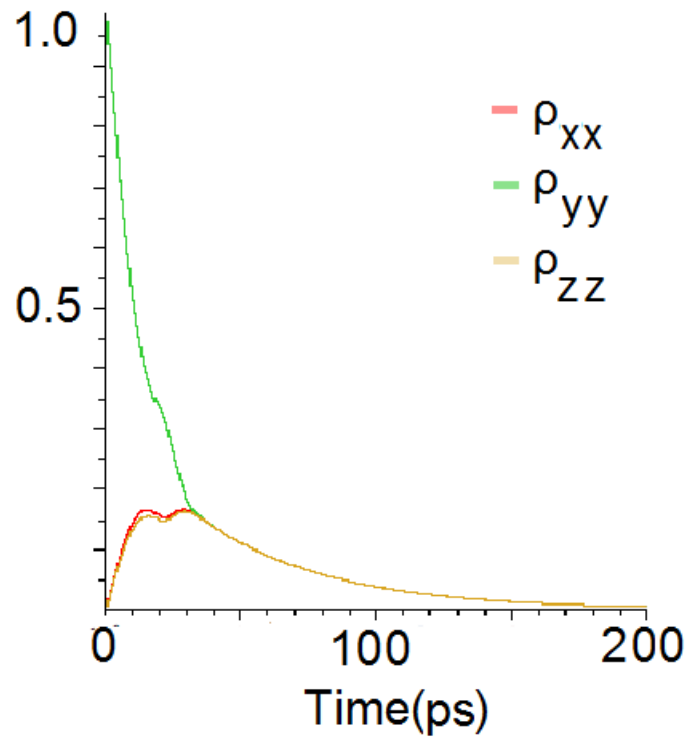


Figure 5.6: Excited state populations for a Lindblad dissipation evolution scheme with decay coupling parameters found by examining state evolution in Fig 5.4. The system evolves from an almost pure excited state and spontaneous emission from this state is able to excite other transitions. For this case, coupling parameters follow the dependence on the density matrix outlined in Section 5.1.

decaying to a ground state ($|g\rangle$), the amplitude of the time-integrated free current can be approximated by

$$\langle J_{ig} \rangle \propto \int |\rho_{ii}| dt. \quad (5.24)$$

In the experimental paper [61], the ratio of instantaneous free currents in perpendicular directions required to observe “transverse optical magnetism” is 0.5 ($J_z = \frac{1}{2} J_y$). In my computational work, I find almost the same ratio for the time averaged free currents in Fig. 5.5. For this particular figure,

$$\frac{J_z}{J_y} \approx \frac{\int |\rho_{zz}| dt}{\int |\rho_{yy}| dt} = 0.55, \quad (5.25)$$

which is a ratio of time-averaged free currents that is very similar to that predicted by ‘magnetic dipole’ scattering (0.5). The key difference between my model and the one presented in [61] is that in my model, there is no magnetic interaction present. All quantum elements interact with each other solely due to electric fields and the ratio of free currents which causes this scattering effect are due to the dipole-dipole coupling between quantum emitters in a dense ensemble.

5.3 Summary

In this chapter, I have provided a method in which the disorder created in the evolution of an ensemble of quantum emitters can be modelled as a single particle decoherence. I have used this to model the state evolution of a dense quantum ensemble using an effective single-particle density matrix. This method works by allowing for FRET-like coupling between multiple quantum emitters in the ensemble. While not as accurate as the full simulation, this method provides a pretty close approximation in significantly less computational time than a full simulation.

Lastly, I briefly show that this overall decoherence can be used to explain the so-called “transverse optical magnetism” phenomenon. In this analysis, I demonstrate that this unusual scattering effect is simply a consequence of inter-particle interactions in a dense quantum ensemble.

Chapter 6

Conclusion

Throughout this thesis, I have examined how the light-matter interaction of open quantum systems can be used to control and assess how these systems behave. These control processes are essential for both understanding of, and searching for applications for these systems. Open quantum systems exhibit novel behaviours that classical systems do not, and this opens up the development of novel materials and new techniques.

By studying the control of single, open quantum systems, I have shown that second-order intensity-intensity correlations allow for the direct observation of analytically-predictable, quantum interference phenomena. While more difficult to observe than traditional spectra (as it is a time-dependent effect) it provides us with more specific information than absorption or emission spectra. Since quantum interference effects occur only in systems in which transitions share common levels, we could use these effects to assess the connectivity of complex quantum systems as well as time-dependent changes in energy levels. These processes could easily serve as the basis of new sensor methods and would allow us to construct energy level diagrams without needing any prior knowledge of the structure of the quantum systems examined. Both of these effects are at their most useful when dealing with atoms or molecules with

complicated energy-level diagrams.

In addition to quantum systems differing greatly in behaviour from their classical analogues, they are also strongly affected by environmental interactions. These environmental interactions are often simplified due to the fact that they are theoretically more difficult to handle. However, the addition of a nearby system (such as a classical metal nanoparticle dimer, or a quantum mechanical cluster of similar atoms) allows the control space of the open quantum system to be expanded with pre-designed environmental interactions serving as additional axes of control. Most noticeably, these environments can affect terms in the Lindblad superoperator in the master equation, which is useful when dealing with systems whose fidelity is purity limited. This is especially useful for modifying properties which are otherwise difficult or impossible to change by control fields.

Specifically, we have shown that by using the Purcell effect in asymmetric nanoplasmonic systems, we can modify and control the overall spontaneous emission rate of a qubit excited state by changing the polarization of the incident control fields. This effect is significant for two reasons. Firstly it represents modifying a process (loss of purity) that cannot normally be affected by control fields. Secondly it allows for the rapid state initialization without reducing the effective lifetime of the qubit. As state initialization and qubit lifetime rely on the same parameter (the spontaneous emission rate), it is very difficult to have both a rapid preparation time and a long operational lifetime. By constructing an appropriate environment relative to our control scheme, we show that these differing goals can be realized concurrently with polarization control.

Evaluating the dynamics of more than a handful of quantum systems is both analytically and computationally intensive. However due to the recent availability of large-scale, fast computation resources, we can begin to examine the overall quantum behaviour of large collections of systems. In these systems, we evaluate quantum

behaviour without the need for restricted basis sets or enforced symmetries to simplify the calculations. It is through these general calculations that one comes to a number of conclusions about the behaviour of statistically large, self-interacting quantum ensembles. I noticed that, over the course of less than a picosecond, dense collections of quantum systems undergo an order-disorder phase transition. When examining the ensemble averaged state populations of the system, the transition acts similar to decoherence due to spontaneous emission. This transition occurs even when the ensemble dimensions are small enough that almost all atoms/molecules experience the same incident field. The decoherence prevented me from initially using this behaviour to design quantum mechanical enhancement for solar cell surfaces. However, this effective decoherence rate is physically significant in its own right as it sets the lifetime for true quantum optical effects. It also explains why classical techniques, such as the discrete dipole approximation, are applicable in most solid-state optics applications — the quantum ensemble rapidly becomes disordered and quantum effects are washed out.

In addition to having a physical consequence, the effective rate of this disorder-induced decoherence also affects theoretical calculation techniques that are commonly applied to ensemble systems in quantum optics. Firstly, the order-disorder transition restricts the applicability of uni-directional basis sets in which the quantum system is assumed to only have a single excited state along the incident field polarization direction. By neglecting the excited states that are perpendicular to the incident polarization direction, simulations and calculations may be artificially neglecting this decoherence and overestimating quantum effects on optical properties. Secondly, the time-dependence of this order-disorder transition also indicates that the short-pulse excitation method, a common-used technique in classical optics, may be limited since the short-pulses typically used do not last long enough to capture the interactions between quantum emitters. This could also lead to overestimates of quantum contri-

butions to the optical properties of advanced materials.

I have also discussed how this decoherence in an ensemble can be approximated by an effective single particle model. My analysis indicates that the inclusion of multiple, energy-neutral, FRET-like decoherence terms enables the single particle model to match results of the large-scale numerical model. This analysis also indicates that the overall decoherence behaves similarly to the FRET process. I used the results of this analysis to provide an elegant explanation for the so called “magnetic-dipole scattering” with ultrafast-sources in dense liquids. My model also explains the intensity and pulse duration dependence of the experiment which is not explained by classical theory.

6.1 Summary of Original Contributions

I expect four peer-reviewed publications that will summarize my research results.

- A manuscript based on results of Chapter 2 entitled “Detection of molecular energy level connectivity using intensity-intensity correlation spectra” is complete, and will be submitted for publication shortly.
- A manuscript based on results of Chapter 3 entitled “Polarization control of spontaneous emission for rapid quantum state initialization” is currently under review in *Phys. Rev. A*.
- A manuscript containing the single particle approximation to the dense ensemble is under preparation (Chapters 4 and 5).
- A manuscript containing the explanation for “transverse optical magnetism” is under preparation (Chapter 5).

I developed the following theoretical models and numerical methodology in the course of my investigations.

- A computational program was written to numerically model the Lindblad-Von Neumann equations. This program is capable of handling large quantum systems of arbitrary dimension; elements such as the Hamiltonian and Lindblad matrices are generated dynamically. New quantum system transitions can be entered by simply specifying which transitions/processes are allowed. The time evolution is executed using a 4th order Runge-Kutta method.
- For the study of an open quantum system interacting with a gold nanoparticle dimer, I refined the methodology developed by a previous graduate student, and extended the analysis to open quantum systems with more than two energy levels. The Lindblad-Von Neumann master equation was solved as described above, and Maxwell's equations were solved by a commercial implementation of the finite-difference time-domain method [84].
- For the study of dense quantum ensembles, a new methodology was developed in order to solve the coupled Maxwell-Lindblad equations. This methodology extended the unidirectional basis states on individuals in the ensembles to three dimensions. A mean field methodology was adapted specifically for this problem, taking care to avoid self-interacting terms. A computational program was written to numerically model the coupled Maxwell-Lindblad equations. This program is capable of handling a variety of field sources and several models of quantum systems. A parallel implementation of the code was developed for execution on SHARCNet. Each calculation took 10-16 CPU days to run on SHARCNet.
- An effective single particle model was proposed to describe the results of the numerical calculation described above. This model included a multi-directional basis set, and adapted the FRET process in biophysics to use dephasing terms to model energy transfer between the quantum systems in the ensemble. An

original hypothesis in this model is that the dephasing rates depend on the excited state populations, and therefore on time. The idea of time-dependent dephasing rates is a novel addition to the thesis.

- Not included in this thesis is the development of a steady-state model of atomic population trapped in a magneto-optical trap. In current models, there is an inconsistency [111, 112] between experiments and theory. My new model resolves this inconsistency. More experiments need to be done before this work can be published.

6.2 Future Directions

For open quantum systems interacting with a classical system, we have already shown that polarization and asymmetric responses can be used to selectively modify the spontaneous emission rate. However, we have limited ourselves to a simple nanoparticle dimer and a general qubit. In reality, any system could be able to utilize this effect to allow for rapid state preparation. Choosing a specific qubit and finding the most optimal environment for that qubit would represent the next direction for investigation. Most noticeably, a nanoplasmonic environment does not represent the only environment that can lead to this decay enhancement. A similar process involving an asymmetric cavity and cavity QED [113, 114, 115] could also be used to implement this process and it may apply to more systems, including those that utilize trapped ions and Rydberg molecules.

For the results on dense quantum ensembles, one important direction this work can take is in evaluating and modifying time-dependent dephasing rates. In most analyses, this emission modification is assumed to be constant and always-on. However, from a Markovian standpoint, that cannot be true as individual systems are only affected by the instantaneous field and quantum state. This indicates that the decay rate

enhancement should be time-dependent and the constant enhancement approximation is probably only valid in systems undergoing continuous excitation.

One particular direction this might take is in refining the model of how interactions between quantum systems can be quantified through these dynamic dephasing rates. While I have shown that this dephasing appears to occur through Forster resonance energy transfer and I have provided a “back-of-the-envelope” estimation of how strong these processes are, the model is far from robust. Refining this model with more accurate ways of determining the strength of the time-dependent couplings would allow for true ensemble control.

A second effect that might be also worth investigating further would be if more complex quantum elements (such as Λ systems) would be able to use quantum interference effects to minimize this large decoherence we see in the numerical simulations. If so, it would pave the way for large-scale quantum optics/quantum control.

Appendix A

Rotating-Wave Approximation Hamiltonian

In a time-dependent density matrix of a quantum system excited by an external field, the oscillations associated with the frequency of the incident field dominate the dynamics of the quantum system. In order to see the slower dynamics, such as Rabi oscillations and quantum interference, it is beneficial to examine the system in a frame that rotates with the incident field frequency.

The general procedure for utilizing this approximation for an N-level quantum system is to first determine a unitary NxN rotation matrix (U_0) that will rotate the system into this frame. One can then determine the rotated Hamiltonian by making the unitary transformation:

$$H' = U_0^{-1} H U_0 - i\hbar U_0^{-1} \dot{U}_0. \quad (\text{A.1})$$

In certain cases, one can set all rapidly oscillating terms to zero and assume that all transitions are near resonance. This is known as the rotating wave approximation [12] and has the effect of slowing the time dependence of the Hamiltonian.

A.1 RWA for Optically-Linked Chains of States Using an Intuitive Representation

In determining the proper RWA equation to use for a system, the main challenge is always in determining U_0 . For the two level and three-level atoms, this choice is well known [12] but for multi-level systems, it can become quite challenging due to having various non-degenerate energy levels. Here, I provide a prescription to determine the unitary matrix U_0 that is best suited to generate the RWA Hamiltonian. If we examine the rotation matrices used for the two and three level systems, we will notice that the transformation consists of two terms, each that has a specific effect on the system when applied. These terms are:

- $\exp(-i\frac{E_j}{\hbar}t)$: This term introduces a reference energy level for the system and helps to introduce detunings.
- $\exp(\pm i\omega_{i,j}t)$: This term rotates out the fast rotation of the system due to the transition frequency $\omega_{i,j}$

Now if one visualizes the system as a graph, with each edge representing a transition, and nodes, representing the energy levels, the system in the non-RWA picture consists of a collection of these edges and nodes oscillating with various frequencies. The goal of the RWA is to first get this system into a picture in which the frequencies of all oscillations are minimized. This requires that the oscillations be split into high and low frequency terms. In this view, the high frequency terms are ignored and the system is left in a slowly varying state.

Now in order to do this, one first sets a reference node, using one of the energy levels (E_r), by introducing a unitary matrix of the form,

$$U_{ref} = \exp(-i\frac{E_r}{\hbar}t)I, \tag{A.2}$$

where I is the identity matrix. Now, with level $|r\rangle$ serving as a fixed reference point, one then introduces a number of rotational corrections (R^n), that minimize for the relative oscillations of the next connected energy levels in either direction ($|r-1\rangle$ and $|r+1\rangle$). Subsequent connections later on in the chain have their connection corrected by introducing additional relative rotations. Mathematically, for all possible n the rotations take the form,

$$R_{jj}^n = \exp(i\omega_{r-n,r-n-1}t)T(j < r-n) + \exp(i\omega_{r+n,r+n+1}t)T(j > r+n), \quad (\text{A.3})$$

where $T(x) = 1$ if the x is true and $T(x) = 0$ if x is false or there are no more states present. Lastly U_0 is constructed by applying these transformations in order ($U_0 = (\prod_n R^n)U_{rot}$). This overall process is pictorially represented in Figure A.1 for a five-level chain.

A.1.1 Two-level System

For a two-level system interacting with a continuous-wave field, the Hamiltonian can be written as

$$H = \begin{pmatrix} E_1 & \frac{\hbar\Omega}{2}(\exp(i\omega t) + \exp(-i\omega t)) \\ \frac{\hbar\Omega}{2}(\exp(i\omega t) + \exp(-i\omega t)) & E_2 \end{pmatrix}. \quad (\text{A.4})$$

One can then rotate this matrix using

$$U_0 = \begin{pmatrix} \exp(-i\frac{E_1}{\hbar}t) & 0 \\ 0 & \exp(i\omega t) \exp(-i\frac{E_1}{\hbar}t) \end{pmatrix}, \quad (\text{A.5})$$

and set all high frequency terms to zero. This leaves us with the RWA Hamiltonian,

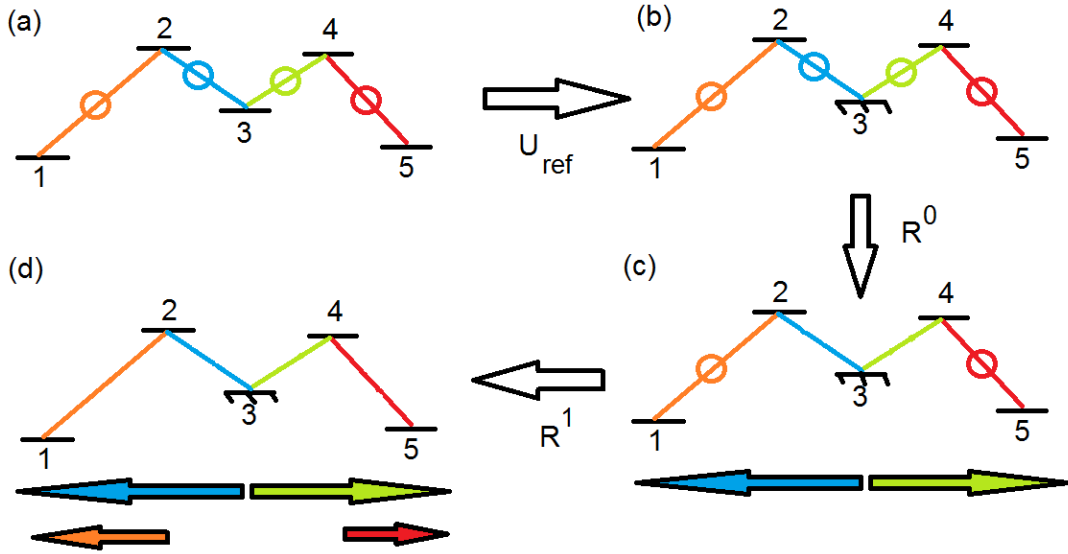


Figure A.1: Pictorial representation of the process of determining the unitary transformation matrix in a 5 level chain. (A) Each transition connects two levels and all edges oscillate at some fast frequency (this oscillation is represented by a circle). A reference level ($|3\rangle$) is chosen and U_{ref} is applied. (b) With $|3\rangle$ serving as a reference level (indicated by diagonal lines under the energy level), the nearest left ($|3\rangle \rightarrow |2\rangle$) and right ($|3\rangle \rightarrow |4\rangle$) transitions are selected for minimization using rotation R^0 . (c) The previous rotation, R^0 which affects all nodes to the left (blue arrow) and to the right (green arrow) removes the oscillation in $|3\rangle \rightarrow |2\rangle$ and $|3\rangle \rightarrow |4\rangle$. The next nearest left ($|2\rangle \rightarrow |1\rangle$) and right ($|4\rangle \rightarrow |5\rangle$) transitions are then selected for minimization using rotation R^1 . (d) Applying R^1 (orange/red arrows) minimizes all rotations and the process is complete.

$$H'_{RWA} = \begin{pmatrix} 0 & \frac{\hbar\Omega}{2} \\ \frac{\hbar\Omega}{2} & -\hbar\Delta \end{pmatrix}, \quad (\text{A.6})$$

where Δ is the detuning between the incident field frequency and the transition frequency.

A.1.2 Three-level System

For a three-level system, such as a ladder, Λ , or V, with a shared middle level and with each transition excited by a near-resonance field, the Hamiltonian can be written as,

$$H = \begin{pmatrix} E_0 & \frac{\hbar\Omega_{01}}{2}(\exp(iw_p t) + \exp(-iw_p t)) & 0 \\ \frac{\hbar\Omega_{10}}{2}(\exp(iw_p t) + \exp(-iw_p t)) & E_1 & \frac{\hbar\Omega_{12}}{2}(\exp(iw_s t) + \exp(-iw_s t)) \\ 0 & \frac{\hbar\Omega_{21}}{2}(\exp(iw_s t) + \exp(-iw_s t)) & E_2 \end{pmatrix}. \quad (\text{A.7})$$

One can then rotate this matrix using the middle state as a reference level,

$$U_0 = \begin{pmatrix} \exp(-i\frac{E_1}{\hbar}t) \exp(iw_p t) & 0 & 0 \\ 0 & \exp(-i\frac{E_1}{\hbar}t) & 0 \\ 0 & 0 & \exp(-i\frac{E_1}{\hbar}t) \exp(iw_s t) \end{pmatrix}. \quad (\text{A.8})$$

Making the RWA leaves us with,

$$H'_{RWA} = \begin{pmatrix} -\hbar\Delta_0 & \frac{\hbar\Omega_{01}}{2} & 0 \\ \frac{\hbar\Omega_{10}}{2} & 0 & \frac{\hbar\Omega_{12}}{2} \\ 0 & \frac{\hbar\Omega_{21}}{2} & -\hbar\Delta_1 \end{pmatrix}. \quad (\text{A.9})$$

where Δ_i is the detuning between the i^{th} incident field frequency and the i^{th} transition frequency.

A.1.3 Degenerate Five-level W System

For a five-level system with three degenerate excited levels, two ground levels, and with each transition excited by a near-resonant field, the Hamiltonian can be written as,

$$H = \begin{pmatrix} 0 & \frac{\hbar\Omega_{g(e,0)}}{2}(e^{iw_p t} + cc) & \frac{\hbar\Omega_{g(e,1)}}{2}(e^{iw_p t} + cc) & \frac{\hbar\Omega_{g(e,-1)}}{2}(e^{iw_p t} + cc) & 0 \\ \frac{\hbar\Omega_{g(e,0)}^*}{2}(e^{iw_p t} + cc) & E_e & 0 & 0 & \frac{\hbar\Omega_{c(e,0)}}{2}(e^{iw_s t} + cc) \\ \frac{\hbar\Omega_{g(e,1)}^*}{2}(e^{iw_p t} + cc) & 0 & E_e & 0 & \frac{\hbar\Omega_{c(e,1)}}{2}(e^{iw_s t} + cc) \\ \frac{\hbar\Omega_{g(e,-1)}^*}{2}(e^{iw_p t} + cc) & 0 & 0 & E_e & \frac{\hbar\Omega_{c(e,-1)}}{2}(e^{iw_s t} + cc) \\ 0 & \frac{\hbar\Omega_{c(e,0)}^*}{2}(e^{iw_s t} + cc) & \frac{\hbar\Omega_{c(e,1)}^*}{2}(e^{iw_s t} + cc) & \frac{\hbar\Omega_{c(e,-1)}^*}{2}(e^{iw_s t} + cc) & E_c \end{pmatrix}. \quad (\text{A.10})$$

One can then rotate this matrix using the degenerate excited states as the reference level,

$$U_0 = \begin{pmatrix} \exp(-i\frac{E_e}{\hbar}t) \exp(iw_p t) & 0 & 0 & 0 & 0 \\ 0 & \exp(-i\frac{E_e}{\hbar}t) & 0 & 0 & 0 \\ 0 & 0 & \exp(-i\frac{E_e}{\hbar}t) & 0 & 0 \\ 0 & 0 & 0 & \exp(-i\frac{E_e}{\hbar}t) & 0 \\ 0 & 0 & 0 & 0 & \exp(-i\frac{E_e}{\hbar}t) \exp(iw_s t) \end{pmatrix}. \quad (\text{A.11})$$

Making the RWA leaves us with,

$$H'_{RWA} = \begin{pmatrix} -\hbar\Delta_g & \frac{\hbar\Omega_{g(e,0)}}{2} & \frac{\hbar\Omega_{g(e,1)}}{2} & \frac{\hbar\Omega_{g(e,-1)}}{2} & 0 \\ \frac{\hbar\Omega_{g(e,0)}^*}{2} & 0 & 0 & 0 & \frac{\hbar\Omega_{c(e,0)}}{2} \\ \frac{\hbar\Omega_{g(e,1)}^*}{2} & 0 & 0 & 0 & \frac{\hbar\Omega_{c(e,1)}}{2} \\ \frac{\hbar\Omega_{g(e,-1)}^*}{2} & 0 & 0 & 0 & \frac{\hbar\Omega_{c(e,-1)}}{2} \\ 0 & \frac{\hbar\Omega_{c(e,0)}^*}{2} & \frac{\hbar\Omega_{c(e,1)}^*}{2} & \frac{\hbar\Omega_{c(e,-1)}^*}{2} & -\hbar\Delta_c \end{pmatrix}, \quad (\text{A.12})$$

where Δ_i is the detuning between the i^{th} incident field frequency and the degenerate transition frequencies i^{th} lower levels.

Appendix B

Scaling Parameters

For most single-atom quantum control systems in the RWA, it is possible to reduce the number of free parameters by scaling the evolution of the system. In most calculations, this scaling is done with respect to a chosen Rabi frequency strength. Under this scaling, the Lindblad-Von Neumann master equation,

$$\frac{\partial \rho}{\partial t} = -\frac{i}{\hbar}[H_{RWA}, \rho] - L(\rho), \quad (\text{B.1})$$

becomes,

$$\frac{\partial \rho}{\partial(\Omega t)} = -\frac{i}{\hbar}[H_{RWA}/\Omega, \rho] - L(\rho)/\Omega, \quad (\text{B.2})$$

$$\frac{\partial \rho}{\partial t'} = -\frac{i}{\hbar}[H'_{RWA}, \rho] - L'(\rho). \quad (\text{B.3})$$

In general, this allows us to report other system parameters using the chosen Rabi frequency as a unit as,

$$\begin{aligned}
\gamma &= \gamma' \Omega, \\
\Delta &= \Delta' \Omega, \\
\Omega_i &= \Omega'_i \Omega, \\
t &= t' \frac{1}{\Omega}, \\
\omega_i &= \omega'_i \Omega.
\end{aligned}
\tag{B.4}$$

The rates reported in Chapter 2 and 3 are all scaled in this manner.

B.1 Number Density

One new scaling parameter introduced into the study of dense ensembles is the number density (N_a) which is simply defined as the number of quantum emitters (atoms) per unit volume. In order to give a empirical feel for how dense various systems are, various number densities of a few materials are provided below [116]:

Object	Density ($\frac{g}{m^3}$)	Molecular Weight ($\frac{g}{mol}$)	Number Density (m^{-3})
N_2 gas (\approx Air)	1.25×10^3	28.014	2.69×10^{25}
H_2O (liquid)	9.97×10^5	18.015	3.33×10^{28}
Au (Metal)	1.93×10^7	196.967	5.90×10^{28}
ZnO powder (Quantum Dot material)	5.6×10^6	81.408	4.14×10^{28}

Appendix C

Steady State Solutions to the Master Equation

One useful property of the master equation is that, due to its Hermitian nature, it consists of N^2 unique equations and N^2 unknowns if ($\dot{\rho} = 0$) and therefore the steady-state solution is always solvable. This means that for any given system, as long as one knows the relevant decay rates, detunings and driving frequencies, one can always predict what the final steady-state populations should be.

For the all cases except the two-level system, the actual solution of the equations was handled through the Maple 11 [117] software package due to the fact that each N level system requires the solution of N^2 equations.

For the two-level system, the steady-state conditions have been solved explicitly simply to demonstrate the overall method, the final solution is identical to that obtained by Maple 11 (see C.1).

C.1 Steady State Conditions of a Two-Level System

In order to find the steady-state condition, one simply needs to find the condition at which $\dot{\rho} = 0$. This involves solving only two update equations (with $\hbar = 1$),

$$\dot{\rho}_{gg} = 0 = \frac{\Omega}{2}(2\text{Im}(\rho_{ge})) + \gamma(1 - \rho_{gg}), \quad (\text{C.1})$$

$$\dot{\rho}_{ge} = 0 = i\frac{\Omega}{2}(2\rho_{gg} - 1) + \rho_{ge}(-i\Delta - \frac{\gamma}{2}), \quad (\text{C.2})$$

as $\rho_{ge} = \rho_{eg}^\dagger$ and $\rho_{ee} = 1 - \rho_{gg}$. By setting $\rho_{gg} = a$ and $\rho_{ge} = b + ic$ and splitting the previous equations into real and imaginary components one is left with,

$$\Omega c + \gamma(1 - a) = 0, \quad (\text{C.3})$$

$$\frac{\Omega}{2}(2a - 1) - b\Delta - c\frac{\gamma}{2} = 0, \quad (\text{C.4})$$

$$c\Delta - b\frac{\gamma}{2} = 0. \quad (\text{C.5})$$

Solving these equations yields,

$$a = 1 - \frac{\frac{\Omega^2}{4}}{\Delta^2 + \frac{\gamma^2}{4} + \frac{\Omega^2}{2}}, \quad (\text{C.6})$$

$$b = \frac{\frac{1}{2}\Delta\Omega}{\Delta^2 + \frac{\gamma^2}{4} + \frac{\Omega^2}{2}}, \quad (\text{C.7})$$

$$c = \frac{\frac{1}{4}\Omega\gamma}{\Delta^2 + \frac{\gamma^2}{4} + \frac{\Omega^2}{2}}. \quad (\text{C.8})$$

Therefore,

$$\rho_{gg} = a = 1 - \frac{\frac{\Omega^2}{4}}{\Delta^2 + \frac{\gamma^2}{4} + \frac{\Omega^2}{2}}, \quad (\text{C.9})$$

$$\rho_{ge} = b + ic = \frac{\frac{1}{2} \Delta \Omega + i \frac{1}{4} \Omega \gamma}{\Delta^2 + \frac{\gamma^2}{4} + \frac{\Omega^2}{2}}. \quad (\text{C.10})$$

The final steady state of a two-level system is therefore independent of the initial state.

C.2 Preparation Limitations of Two-level Quantum Systems

A two-level quantum system with states $|g\rangle$ and $|e\rangle$ is the simplest model of a qubit. This quantum system is driven by a electromagnetic wave that is incident on the entire system. The Hamiltonian of this driven two-level quantum system has the field-matter interaction of the system treated in the electric-dipole approximation described by $\hat{H} = \hat{H}_a + \mu \cdot \mathbf{E}(t)$, where H_a is the Hamiltonian of a two-level system, μ is the transition dipole moment of the system and $\mathbf{E}(t)$ is electric field of the wave interacting with the system. This electric field magnitude varies in time as $E(t) = E_L \cos(\omega_L t)$ where ω_L is the frequency of the incident wave.

Making the rotating wave approximation (RWA), the matrix form of the Hamiltonian can be written as,

$$H_{RWA} = \begin{pmatrix} 0 & \frac{\hbar \Omega_{ge}}{2} \\ \frac{\hbar \Omega_{ge}^*}{2} & -\hbar \Delta \end{pmatrix}, \quad (\text{C.11})$$

where Δ represents the detuning between the frequency of the incident field and frequency of the state transition. The Rabi frequency, $\Omega_{ge} = \frac{\mu_{ge} E_L}{\hbar}$, depends on the

amplitude of the local electric field (E_L).

In order to study the time-dependent response of an qubit to both the environment and the incident electromagnetic wave, I use a density matrix representation of the qubit's state. For our two-level system this density matrix is of the form,

$$\rho = \begin{pmatrix} \rho_{gg} & \rho_{ge} \\ \rho_{eg} & \rho_{ee} \end{pmatrix}. \quad (\text{C.12})$$

This density matrix evolves in time under the Liouville-Von Neumann equation which takes the form,

$$\dot{\rho} = -\frac{i}{\hbar}[H_{RWA}, \rho] - L(\rho). \quad (\text{C.13})$$

In this evolution equation, the Lindblad term, L , models the decoherence in the system. This term is linear in the state density operator and is of the form,

$$\hat{L} = \sum_d \frac{\gamma_d}{2} (\sigma_d^\dagger \sigma_d \rho + \rho \sigma_d^\dagger \sigma_d - 2\sigma_d \rho \sigma_d^\dagger), d = 0, 1. \quad (\text{C.14})$$

In this equation, σ_d are the Lindblad operators and I assume that the only decoherence mechanism present is spontaneous emission. Therefore γ_d represents the decay rate from the excited states to the ground state and I take $\sigma_d^\dagger = |g\rangle\langle e|$. I quantify the purity of a state as $Purity = Tr(\rho^2)$ [118]. Under this description, states with a higher purity are closer to being pure states.

If one wants to prepare a qubit in a stable initial state without having any knowledge of its initial state, we must use a continuous applied field and set the qubit to a steady state. As the Lindblad equation describes the evolution of the state densities over time, one solves it under the condition that $\dot{\rho} = 0$ and find the steady state populations of the system,

$$\rho_{gg} = 1 - \frac{\frac{\Omega^2}{4}}{\Delta^2 + \frac{\gamma^2}{4} + \frac{\Omega^2}{2}}; \quad (\text{C.15})$$

$$\rho_{ge} = \frac{\frac{1}{2} \Delta \Omega + i \frac{1}{4} \Omega \gamma}{\Delta^2 + \frac{\gamma^2}{4} + \frac{\Omega^2}{2}}; \quad (\text{C.16})$$

These equations indicate which final state the system will end up in, *regardless of initial conditions*, as long as a continuous field is applied (even if that field is zero). In order to illustrate this, I have evolved a qubit to the same final state for a variety of initial mixed states. Figures C.1 and C.2 show this system evolving, under an arbitrary chosen detuning and spontaneous decay rate, to a desired final ground state population $\rho_{gg} = 0.75$. Each state is initialized with no coherence, $\rho_{ge} = 0$ and evolves to the same final state in the same amount of time.

As the purity of the quantum system is dependent on only the coherence and ground state population, the final purity of any quantum state subjected to an external field will only depend on the steady-state that will be reached. In fact the steady-state purity of the two-level qubit can be shown, using Equations C.15 and C.16, to be entirely dependant on the choice of a desired, steady-state, ground state population, ($\rho_{gg} = \rho_d$), with

$$Purity = 4\rho_d - 2\rho_d^2 - 1. \quad (\text{C.17})$$

This dependence of the purity on the final steady-state indicates that a continuous electromagnetic wave can be used to reset a quantum state to a fixed purity. This differs from pulsed excitation schemes in that the initial purity can be changed and the initial state does not need to be known. It also avoids the need to allow the system to decay completely to the ground state.

Under this relationship it is not possible to reach a completely pure steady-state that is not in the ground state configuration using only spontaneous decay and a two-level system. This limitation restricts this method of preparation to those in which high levels of purity are not required. It also indicates that for a purely two-level quantum system, including a nanoparticle simply serves to enhance the rate at which

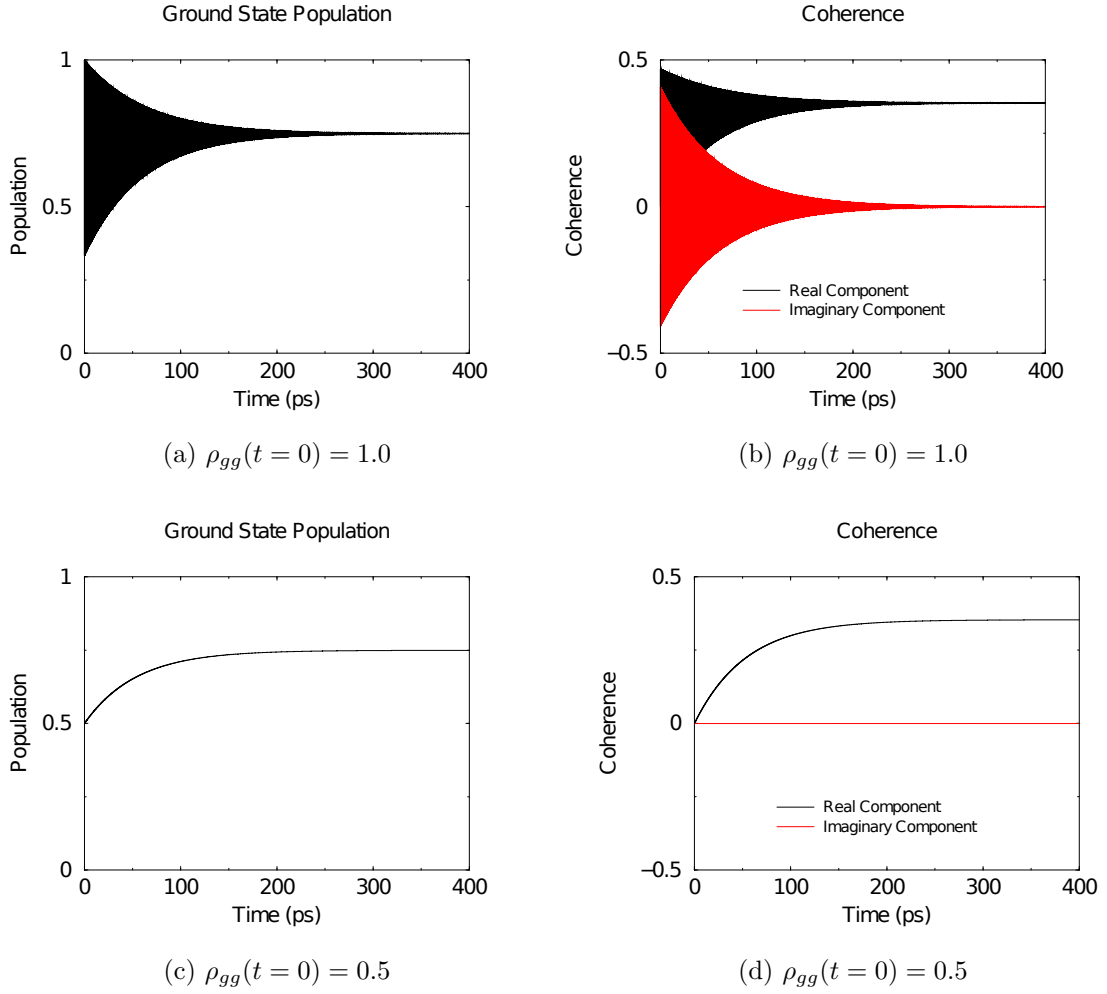


Figure C.1: Ground state populations and coherences of the qubit with $\gamma = 2.81 \times 10^{10} s^{-1}$ and $\Delta = 1.37 \times 10^{14} s^{-1}$ is evolved from a variety of initial conditions to reach the desired state populations $\rho_{gg} = 0.75$ and $\rho_{ee} = 0.25$

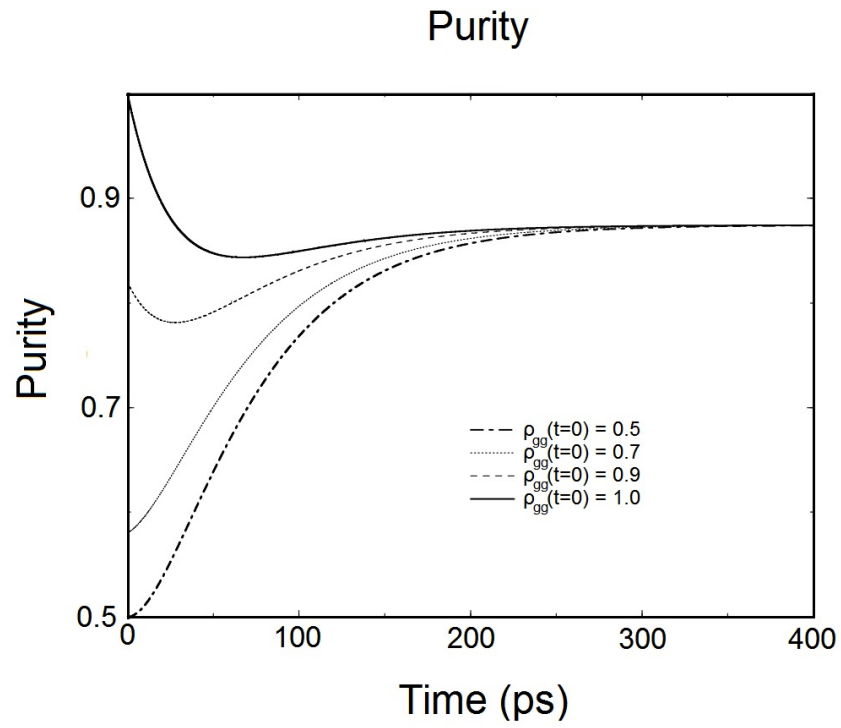


Figure C.2: Purity of the qubit, with $\gamma = 2.81 \times 10^{10} s^{-1}$ and $\Delta = 1.37 \times 10^{14} s^{-1}$, when it is evolved from a variety of initial conditions to reach the desired state populations $\rho_{gg} = 0.75$ and $\rho_{ee} = 0.25$

the two-level quantum system reaches a steady-state; it does not improve the purity of that state in any way. The specifics for this calculations are shown in [C.2.1].

C.2.1 Purity of a Two-level System in a Steady-State

In order to find the purity relationship for the two level system, one needs to evaluate the magnitude of the matrix elements as

$$Purity = tr(\rho^2) = 1 - 2\rho_{gg} + 2\rho_{gg}^2 + 2|\rho_{ge}|^2. \quad (C.18)$$

From the previous steady state solutions one can define the quantities required to find the purity,

$$\rho_{gg} = 1 - \frac{\frac{\Omega^2}{4}}{\Delta^2 + \frac{\gamma^2}{4} + \frac{\Omega^2}{2}} = \frac{\Delta^2 + \frac{\gamma^2}{4} + \frac{\Omega^2}{4}}{\Delta^2 + \frac{\gamma^2}{4} + \frac{\Omega^2}{2}}, \quad (C.19)$$

$$\rho_{ge} = \frac{\frac{1}{2} \Delta \Omega + i\frac{1}{4}\Omega\gamma}{\Delta^2 + \frac{\gamma^2}{4} + \frac{\Omega^2}{2}}, \quad (C.20)$$

$$|\rho_{ge}|^2 = \frac{\Omega^2}{4} \frac{\Delta^2 + \frac{\gamma^2}{4}}{(\Delta^2 + \frac{\gamma^2}{4} + \frac{\Omega^2}{2})^2}. \quad (C.21)$$

One can express ρ_{gg} in terms of itself and $|\rho_{ge}|^2$ as

$$\rho_{gg} = \frac{\Delta^2 + \frac{\gamma^2}{4} + \frac{\Omega^2}{4}}{\Delta^2 + \frac{\gamma^2}{4} + \frac{\Omega^2}{2}} \cdot \frac{\Delta^2 + \frac{\gamma^2}{4} + \frac{\Omega^2}{4}}{\Delta^2 + \frac{\gamma^2}{4} + \frac{\Omega^2}{2}}, \quad (C.22)$$

$$\rho_{gg} = \frac{(\Delta^2 + \frac{\gamma^2}{4} + \frac{\Omega^2}{4})(\Delta^2 + \frac{\gamma^2}{4} + \frac{\Omega^2}{2})}{(\Delta^2 + \frac{\gamma^2}{4} + \frac{\Omega^2}{2})^2}, \quad (C.23)$$

$$\rho_{gg} = \frac{(\Delta^2 + \frac{\gamma^2}{4} + \frac{\Omega^2}{4})^2 + \frac{1}{4}\Omega^2(\Delta^2 + \frac{\gamma^2}{4}) + \frac{\Omega^4}{16}}{(\Delta^2 + \frac{\gamma^2}{4} + \frac{\Omega^2}{2})^2}, \quad (C.24)$$

$$\rho_{gg} = \rho_{gg}^2 + |\rho_{ge}|^2 + (1 - \rho_{gg})^2. \quad (C.25)$$

Therefore,

$$|\rho_{ge}|^2 = 3\rho_{gg} - 2\rho_{gg}^2 - 1, \quad (\text{C.26})$$

and the purity for any steady-state two-level system can be expressed in terms of ρ_{gg} with,

$$\text{Purity} = 4\rho_{gg} - 2\rho_{gg}^2 - 1. \quad (\text{C.27})$$

C.3 Preparing Pure States in a Three-level Lambda System with Decay Enhancement

In a three-level lambda system it is possible to set up a doubly-driven system in which both transitions experience the same detuning ($\Delta_{ge} = \Delta_{ce}$). This purification occurs due to the presence of a dark state similar to what is used for electromagnetically induced transparency. With this condition one can solve the Lindblad equation for the steady state condition ($\dot{\rho} = 0$). This yields steady state densities,

$$\rho_{gg} = \frac{\Omega_{ce}^2}{\Omega_{ge}^2 + \Omega_{ce}^2}, \quad (\text{C.28})$$

$$\rho_{cc} = \frac{\Omega_{ge}^2}{\Omega_{ge}^2 + \Omega_{ce}^2}, \quad (\text{C.29})$$

$$\rho_{gc} = \frac{\Omega_{ge}\Omega_{ce}}{\Omega_{ge}^2 + \Omega_{ce}^2}, \quad (\text{C.30})$$

$$\rho_{ce} = \rho_{ge} = \rho_{ee} = 0, \quad (\text{C.31})$$

leaving,

$$\rho = \begin{pmatrix} \frac{\Omega_{ce}^2}{\Omega_{ge}^2 + \Omega_{ce}^2} & 0 & \frac{\Omega_{ge}\Omega_{ce}}{\Omega_{ge}^2 + \Omega_{ce}^2} \\ 0 & 0 & 0 \\ \frac{\Omega_{ge}\Omega_{ce}}{\Omega_{ge}^2 + \Omega_{ce}^2} & 0 & \frac{\Omega_{ge}^2}{\Omega_{ge}^2 + \Omega_{ce}^2} \end{pmatrix}, \quad (\text{C.32})$$

which is a completely pure state ($Purity = 1$) which can be reached regardless of the initial qubit state. This allows a completely pure state can be reached under excitation.

For a three-level system, the time taken to reach this pure state is no longer proportional to a single decay rate but to two different decay rates. In other words, in order to increase the purification time of the system, one is not required to increase both decay rates. This can be seen in Figure C.3 in which the time required to reach a steady state, normalized to the case in which one decay rate is negligible when compared to the other, is plotted versus various ratios of decay rates. This significance of this effect is in the fact that the overall convergence time is not equal to the product of the two decay rates; even if one is negligible, if the other decay rate is large enough, one can still purify on a short timescale. This means that in the case of a highly enhanced decay rate, the overall time required to reach a completely pure state will depend mostly on the highest decay rate.

This overall effect is significant in that it is a purely quantum effect as opposed to a classical one. If one were to look at the classical picture of a dipole oriented in an arbitrary direction, one would be able to decompose it into two perpendicular dipoles. Each of these dipoles would have its own relaxation rate and thus the overall relaxation rate of the system would be proportional to the slowest rate. For a quantum system however, it is not always possible to decouple the two different transitions, therefore the relaxation rate of one transition can affect the other even if the two effective dipoles are perpendicular.

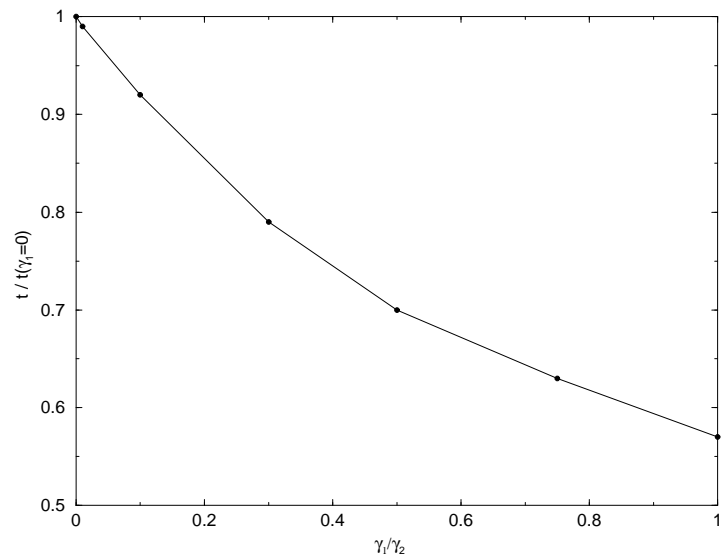


Figure C.3: The time required to reach a steady state in a three-level lambda system, normalized to the case in which one decay rate is negligible when compared to the other, is plotted versus various ratios of decay rates.

Appendix D

Lorentz-Lorenz Shift

D.1 Classical Evaluation

This derivation is largely from [H.A. Lorentz, The Theory of Electrons, 1952], sections 110-140 and Note 54.

The main idea behind the LL shift is that in an atom there are electrons. If one views the nuclei of the atoms to be stationary, all interactions between the atoms and an electric field is due to the movement of the electron. This means that there is a classical differential equation in 3D that describes the movement of that electron in terms of the fields (given that the electron and proton form a dipole). For a field in the z direction,

$$\begin{aligned} m \frac{\partial^2 x}{\partial t^2} &= e(E_x + aP_x) - fx - g \frac{\partial x}{\partial t} + \frac{eH_{extz}}{c} \frac{\partial y}{\partial t}, \\ m \frac{\partial^2 y}{\partial t^2} &= e(E_y + aP_y) - fy - g \frac{\partial y}{\partial t} - \frac{eH_{extz}}{c} \frac{\partial x}{\partial t}, \\ m \frac{\partial^2 z}{\partial t^2} &= e(E_z + aP_z) - fz - g \frac{\partial y}{\partial t}. \end{aligned} \tag{D.1}$$

In this equation m and e are the mass/charge of the electron, f is the term that describe the natural oscillation of the dipole, g represents a damping force and H_{extz} is the external magnetic field.

These equations can be converted to those that only depend on the polarization P by assuming that the position of the electron determines the polarization. It is also assumed that the electron is in an area in which there are N other electrons. Introducing the following scaled variables,

$$\begin{aligned} m' &= \frac{m}{Ne^2}, \\ f' &= \frac{f}{Ne^2}, \\ g' &= \frac{g}{Ne^2}, \end{aligned} \tag{D.2}$$

this takes the form,

$$\begin{aligned} m' \frac{\partial^2 P_x}{\partial t^2} &= E_x + aP_x - f'P_x - g' \frac{\partial P_x}{\partial t} + \frac{H_{extz}}{cNe} \frac{\partial P_y}{\partial t}, \\ m' \frac{\partial^2 P_y}{\partial t^2} &= E_y + aP_y - f'P_y - g' \frac{\partial P_y}{\partial t} - \frac{H_{extz}}{cNe} \frac{\partial P_x}{\partial t}, \\ m' \frac{\partial^2 P_z}{\partial t^2} &= E_z + aP_z - f'P_z - g' \frac{\partial P_z}{\partial t}. \end{aligned} \tag{D.3}$$

Now in the work by Lorentz, it is assumed that,

$$P \rightarrow \exp(i\omega t), \tag{D.4}$$

which leads to equations,

$$\begin{aligned}
 E_x &= (\alpha + i\beta)P_x - i\gamma P_y, \\
 E_y &= (\alpha + i\beta)P_y + i\gamma P_x, \\
 E_z &= (\alpha + i\beta)P_z,
 \end{aligned}
 \tag{D.5}$$

where,

$$\begin{aligned}
 \alpha &= f' - a - m'\omega^2, \\
 \beta &= g'\omega, \\
 \gamma &= \frac{H_{extz}}{cNe}.
 \end{aligned}
 \tag{D.6}$$

Now if one assumes that $H_{extz} \rightarrow 0$ and $\beta \rightarrow 0$, one can show from Maxwell's equations of motion for an EM wave that,

$$n^2 = 1 + \frac{1}{\alpha},
 \tag{D.7}$$

where n is the index of refraction. Therefore the main contribution of the Lorentz-Lorenz shift comes from the dependence of the new frequency of oscillation α on the number of electrons N .

Appendix E

Pseudo-Spectral Time Domain

E.1 Evolution of the Fields

In order to evolution the fields, I implement a Pseudo-Spectral Time-Domain method (PSTD)[101, 102]. This method basically uses a Fourier transform to evaluate the spatial derivatives in Maxwell's Equations and then updates the fields discretely in time. The analysis and symbol conventions are taken from Section 1.4 and 3.7 of [119]. In Maxwell's equations, a non-physical “magnetic conductivity” (σ^M) is introduced to allow no reflection and strong absorption at the boundaries. Thus the equations that are solved are,

$$\nabla \times \mathbf{E} = -\mu \frac{\partial \mathbf{H}}{\partial t} - \sigma^M \mathbf{H} \quad (\text{E.1})$$

and

$$\nabla \times \mathbf{H} = \epsilon \frac{\partial \mathbf{E}}{\partial t} + \sigma \mathbf{E} + \mathbf{J}, \quad (\text{E.2})$$

where \mathbf{H} and \mathbf{E} are the magnetic and electric fields respectively, σ and σ^M are the electrical conductivity and “magnetic conductivity” and \mathbf{J} is the free current density.

In my calculations, these conductivities (σ , σ^M) are only used at the boundaries to attenuate fields without reflections and therefore are set to zero everywhere else.

The first thing I do is note the symmetry of the two equations (E.1 and E.2). I rewrite them in the form,

$$\nabla \times \mathbf{G} = a \frac{\partial \mathbf{F}}{\partial t} - \sigma_a \mathbf{F} + \mathbf{J}_a, \quad (\text{E.3})$$

where $(\mathbf{G}, \mathbf{F}, a, \sigma_a, \mathbf{J}_a) = (\mathbf{E}, \mathbf{H}, -\mu, \sigma^M, 0)$ or $(\mathbf{H}, \mathbf{E}, \epsilon, -\sigma, J)$. This allows for the reuse of numerical subroutines to update both electric and magnetic fields. Rearranging the above into an update equation for a \mathbf{F} ,

$$\frac{\partial \mathbf{F}}{\partial t} = \frac{1}{a} [\nabla \times \mathbf{G} + \sigma_a \mathbf{F} - \mathbf{J}_a]. \quad (\text{E.4})$$

Note that all vectors (\mathbf{F} , \mathbf{G} and \mathbf{J}_a) are in Cartesian components to get scalar equations for each directional component. This yields

$$\frac{\partial F_x}{\partial t} = \frac{1}{a} \left[\frac{dG_z}{dy} - \frac{dG_y}{dz} + \sigma_a F_x - J_{ax} \right], \quad (\text{E.5})$$

$$\frac{\partial F_y}{\partial t} = \frac{1}{a} \left[\frac{dG_x}{dz} - \frac{dG_z}{dx} + \sigma_a F_y - J_{ay} \right], \quad (\text{E.6})$$

and

$$\frac{\partial F_z}{\partial t} = \frac{1}{a} \left[\frac{dG_y}{dx} - \frac{dG_x}{dy} + \sigma_a F_z - J_{az} \right]. \quad (\text{E.7})$$

Now in order to update these equations, I need to evaluate the spatial derivatives, which is the main computational cost. For this calculation, I use a complex, 3D Fast-Fourier Transform (FFT) method. I implement the open-source FFTW package [120] as it is numerically stable, parallelized and officially supported by the SHARCNET [121] system. In this package, the three field components (G_η , where $\eta = x, y, z$) are

transformed into the wavenumber domain, yielding

$$G_\eta(x, y, z) \rightarrow G_\eta(n, l, m) = \sum_{n,l,m} A_{n,l,m} \exp(ik_x^{(n)}x) \exp(ik_y^{(l)}y) \exp(ik_z^{(m)}z). \quad (\text{E.8})$$

In this domain, the spatial derivatives can be evaluated by

$$\frac{dG_\eta(n, l, m)}{d\eta'} = \sum_{n,l,m} ik_{\eta'}^{(s)} A_{n,l,m} \exp(ik_x^{(n)}x) \exp(ik_y^{(l)}y) \exp(ik_z^{(m)}z). \quad (\text{E.9})$$

where $(\eta', s) = (x, n)$, (y, l) or (z, m) . In order to obtain the spatial derivative of G_η , I use an Inverse FFT on the derivative to return to real space:

$$\frac{dG_\eta(n, l, m)}{d\eta'} \rightarrow \frac{dG_\eta(x, y, z)}{d\eta'}. \quad (\text{E.10})$$

Therefore in order to evaluate all the derivatives needed, I require 3 FFTs (one for each real space component) and 6 inverse FFTs (one for each derivative).

Once the derivatives are calculated, I simply update the fields by

$$F_\eta(t + \Delta t) = F_\eta(t) + \frac{\Delta t}{a} \left[\frac{dG_z}{dy} - \frac{dG_y}{dz} + \sigma_a F_x - J_{ax} \right]. \quad (\text{E.11})$$

However, this leads to issues near the spatial boundaries of the simulation. Given that the FFT provides a spatially periodic boundary condition (its functional form is $\exp(ik_\eta^{(s)}\eta)$, which is naturally periodic), in order to terminate the simulation in the propagation direction, an attenuating perfectly-matched layer (PML) [122] is needed. If this boundary is not placed in, one is left with a wraparound error in which fields leaving the simulation in the propagation direction will loop around at the boundary and re-enter the simulation.

The PML chosen for this simulation is the uniaxial PML, which introduces direction-dependent conductivities (σ_η). σ_η is a parameter which controls the attenuation of

fields travelling in the $\hat{\eta}$ direction at different locations [119, 123]. The PML matches a strongly attenuating layer to the edges of the simulation so that the reflection coefficient of the interface between that boundary layer and the simulation space is zero. This lack of reflection is enforced through the matching condition

$$\frac{\sigma_\eta}{\epsilon} = \frac{\sigma_\eta^M}{\mu} \quad (\text{E.12})$$

and by using a “coordinate stretching” tensor inside the PML [119, 123]. First I introduce field stretching variables in each direction η ,

$$S_\eta = 1 + \frac{\sigma_\eta}{i\omega\epsilon}, \quad (\text{E.13})$$

for the electric field and,

$$S_\eta^M = 1 + \frac{\sigma_\eta^M}{i\omega\mu}, \quad (\text{E.14})$$

for the magnetic field. With these, the field components are transformed as,

$$E'_\eta = S_\eta E_\eta, \quad (\text{E.15})$$

and

$$H'_\eta = S_\eta^M H_\eta. \quad (\text{E.16})$$

The matching condition, $S_\eta = S_\eta^M$, ensures that there is no reflection of either field. By setting σ_η and σ_η^M to a non-zero value, attenuation is introduced to fields travelling in the η direction.

If one examines Maxwell’s equations in the PML, one can write it with these stretched fields as [123],

$$i\omega\epsilon \overleftrightarrow{T} \mathbf{E}' = \nabla \times \mathbf{H}', \quad (\text{E.17})$$

and

$$i\omega\mu\overleftrightarrow{T}\mathbf{H}' = -\nabla \times \mathbf{E}'. \quad (\text{E.18})$$

Here \overleftrightarrow{T} is a tensor defined as,

$$\overleftrightarrow{T} = \begin{pmatrix} \frac{S_y S_z}{S_x} & 0 & 0 \\ 0 & \frac{S_x S_z}{S_y} & 0 \\ 0 & 0 & \frac{S_x S_y}{S_z} \end{pmatrix}. \quad (\text{E.19})$$

One then introduces a new set of variable to help deal with the tensor. For the electric and magnetic fields I introduce “stretched fields”, \mathbf{D} and \mathbf{B} , with,

$$\begin{aligned} D_x &= \epsilon \frac{S_z}{S_x} E_x, \\ D_y &= \epsilon \frac{S_x}{S_y} E_y, \\ D_z &= \epsilon \frac{S_y}{S_z} E_z, \\ B_x &= \epsilon \frac{S_z}{S_x} H_x, \\ B_y &= \epsilon \frac{S_x}{S_y} H_y, \\ B_z &= \epsilon \frac{S_y}{S_z} H_z. \end{aligned} \quad (\text{E.20})$$

I then place these stretched fields into the left hand side of Equations E.17 and E.18. I then replace the remaining S_η term with its definition in E.13 (keeping in mind that $S_\eta = S_\eta^M$) and replace $i\omega$ with $\frac{d}{dt}$. For the \hat{x} components of E.20,

$$\frac{dD_x}{dt} + \frac{\sigma_y}{\epsilon} D_x = \frac{dH_z}{dy} - \frac{dH_y}{dz}.$$

Similarly,

$$\begin{aligned}
\frac{dD_y}{dt} + \frac{\sigma_z}{\epsilon} D_y &= \frac{dH_x}{dz} - \frac{dH_z}{dx}, \\
\frac{dD_z}{dt} + \frac{\sigma_x}{\epsilon} D_z &= \frac{dH_y}{dx} - \frac{dH_x}{dy}, \\
\frac{dB_x}{dt} + \frac{\sigma_y}{\epsilon} B_x &= -\left(\frac{dE_z}{dy} - \frac{dE_y}{dz}\right), \\
\frac{dB_y}{dt} + \frac{\sigma_z}{\epsilon} B_y &= -\left(\frac{dE_x}{dz} - \frac{dE_z}{dx}\right), \\
\frac{dB_z}{dt} + \frac{\sigma_x}{\epsilon} B_z &= -\left(\frac{dE_y}{dx} - \frac{dE_x}{dy}\right)
\end{aligned} \tag{E.21}$$

and:

$$\begin{aligned}
\epsilon \frac{dE_x}{dt} + \sigma_z E_x &= \frac{dD_x}{dt} + \frac{\sigma_x}{\epsilon} D_x, \\
\epsilon \frac{dE_y}{dt} + \sigma_x E_y &= \frac{dD_y}{dt} + \frac{\sigma_y}{\epsilon} D_y, \\
\epsilon \frac{dE_z}{dt} + \sigma_y E_z &= \frac{dD_z}{dt} + \frac{\sigma_z}{\epsilon} D_z, \\
\mu \frac{dH_x}{dt} + \sigma_z H_x &= \frac{dB_x}{dt} + \frac{\sigma_x}{\epsilon} B_x, \\
\mu \frac{dH_y}{dt} + \sigma_x H_y &= \frac{dB_y}{dt} + \frac{\sigma_y}{\epsilon} B_y, \\
\mu \frac{dH_z}{dt} + \sigma_y H_z &= \frac{dB_z}{dt} + \frac{\sigma_z}{\epsilon} B_z.
\end{aligned} \tag{E.22}$$

With these equations, one can implement an update equation for both fields (stretched and regular) with the update equations $((G, F, a, \sigma_\eta, L) = (E, H, -\mu, \sigma_\eta, D)$ or $(H, E, \epsilon, \sigma_\eta, B)$):

$$\begin{aligned}
L_x(t + \Delta t) &= \frac{2\epsilon - \sigma_y \Delta t}{2\epsilon + \sigma_y \Delta t} L_x(t) + \frac{a}{|a|} \frac{2\epsilon \Delta t}{2\epsilon + \sigma_y \Delta t} \left(\frac{dG_z}{dy} - \frac{dG_y}{dz} \right), \\
L_y(t + \Delta t) &= \frac{2\epsilon - \sigma_z \Delta t}{2\epsilon + \sigma_z \Delta t} L_y(t) + \frac{a}{|a|} \frac{2\epsilon \Delta t}{2\epsilon + \sigma_z \Delta t} \left(\frac{dG_x}{dz} - \frac{dG_z}{dx} \right), \\
L_z(t + \Delta t) &= \frac{2\epsilon - \sigma_x \Delta t}{2\epsilon + \sigma_x \Delta t} L_z(t) + \frac{a}{|a|} \frac{2\epsilon \Delta t}{2\epsilon + \sigma_x \Delta t} \left(\frac{dG_y}{dx} - \frac{dG_x}{dy} \right).
\end{aligned} \tag{E.23}$$

$$\begin{aligned}
F_x(t + \Delta t) &= \frac{2\epsilon - \sigma_z \Delta t}{2\epsilon + \sigma_z \Delta t} F_x(t) + \frac{1}{|a|} \left(\frac{2\epsilon + \sigma_x \Delta t}{2\epsilon + \sigma_z \Delta t} L_x(t + \Delta t) - \frac{2\epsilon - \sigma_x \Delta t}{2\epsilon + \sigma_z \Delta t} L_x(t) \right), \\
F_y(t + \Delta t) &= \frac{2\epsilon - \sigma_x \Delta t}{2\epsilon + \sigma_x \Delta t} F_y(t) + \frac{1}{|a|} \left(\frac{2\epsilon + \sigma_y \Delta t}{2\epsilon + \sigma_x \Delta t} L_y(t + \Delta t) - \frac{2\epsilon - \sigma_y \Delta t}{2\epsilon + \sigma_x \Delta t} L_y(t) \right), \\
F_z(t + \Delta t) &= \frac{2\epsilon - \sigma_y \Delta t}{2\epsilon + \sigma_y \Delta t} F_z(t) + \frac{1}{|a|} \left(\frac{2\epsilon + \sigma_z \Delta t}{2\epsilon + \sigma_y \Delta t} L_z(t + \Delta t) - \frac{2\epsilon - \sigma_z \Delta t}{2\epsilon + \sigma_y \Delta t} L_z(t) \right).
\end{aligned} \tag{E.24}$$

Note that the $|a|$ terms exist to account for the sign difference between E and H fields in Maxwell's equations.

With these update equations, as long as no free currents exist near the boundaries, all that needs to be done to ensure attenuation in a region (in the η direction) without reflection is to set $\sigma_\eta \gg 0$. The addition of stretched fields do increase the memory requirements of the system, but do not significantly increase computational time as the bulk of the time is required to perform Fourier transforms.

If I examine places in which the PML is not present ($\sigma = 0$) these equations reduce to:

$$\begin{aligned}
L_x(t + \Delta t) &= L_x(t) + \frac{a}{|a|} \Delta t \left(\frac{dG_z}{dy} - \frac{dG_y}{dz} \right), \\
L_y(t + \Delta t) &= L_y(t) + \frac{a}{|a|} \Delta t \left(\frac{dG_x}{dz} - \frac{dG_z}{dx} \right), \\
L_z(t + \Delta t) &= L_z(t) + \frac{a}{|a|} \Delta t \left(\frac{dG_y}{dx} - \frac{dG_x}{dy} \right).
\end{aligned} \tag{E.25}$$

and

$$\begin{aligned}
F_x(t + \Delta t) &= F_x(t) + \frac{1}{|a|}(L_x(t + \Delta t) - L_x(t)), \\
F_y(t + \Delta t) &= F_y(t) + \frac{1}{|a|}(L_y(t + \Delta t) - L_y(t)), \\
F_z(t + \Delta t) &= F_z(t) + \frac{1}{|a|}(L_z(t + \Delta t) - L_z(t)).
\end{aligned} \tag{E.26}$$

When combined, we are left with

$$\begin{aligned}
F_x(t + \Delta t) &= F_x(t) + \frac{\Delta t}{a} \left(\frac{dG_y}{dx} - \frac{dG_x}{dy} \right), \\
F_y(t + \Delta t) &= F_y(t) + \frac{\Delta t}{a} \left(\frac{dG_x}{dz} - \frac{dG_z}{dx} \right), \\
F_z(t + \Delta t) &= F_z(t) + \frac{\Delta t}{a} \left(\frac{dG_y}{dx} - \frac{dG_x}{dy} \right),
\end{aligned} \tag{E.27}$$

which is the same as the general update equation when $\mathbf{J}=0$ in the local region. In order to account for the contribution of the free current (\mathbf{J}) to the total electric field, a local contribution is calculated,

$$E_\eta^J = -\frac{J_\eta \Delta t}{\epsilon}, \tag{E.28}$$

and then added to the new fields,

$$\mathbf{E}(t + \Delta t) = \mathbf{E}_{fields}(t + \Delta t) + \mathbf{E}^J. \tag{E.29}$$

In order to find the free current [47], one needs to find the rate of change of the polarization (\mathbf{P}) as,

$$\mathbf{J} = \frac{d\mathbf{P}}{dt}. \tag{E.30}$$

To do this, one calculates the polarization in each direction,

$$P_\eta = N_a \langle \mu_\eta \rangle = N_a \text{Tr}(\rho \hat{\mu}_\eta), \quad (\text{E.31})$$

where ρ is the density matrix of the local atoms, μ is the dipole moment operator ($\hat{\mu}_\eta = -\frac{d\hat{H}}{dE_\eta}$) and N_a is the number density of the atoms. Putting these together with the reasonable assumptions that $\frac{\partial \hat{\mu}_\eta}{\partial t} = \frac{\partial N_a}{\partial t} = 0$ we get,

$$J_\eta = N_a \text{Tr}(\dot{\rho} \hat{\mu}_\eta), \quad (\text{E.32})$$

where,

$$\dot{\rho} = -\frac{i}{\hbar} [H_{RWA}, \rho] - L(\rho). \quad (\text{E.33})$$

E.1.1 PSTD Stability

The PSTD method's stability in this form has been evaluated previously [101, 102] and for this method the stability criterion is (for a 3D case),

$$\frac{c \Delta t}{\Delta x} < \frac{2}{\sqrt{3\pi}}, \quad (\text{E.34})$$

where Δx and Δt are the coarse-grain lattice size and finite time step size respectively.

Therefore for a typical case in which nm resolution is needed,

$$\Delta t < \frac{2}{\sqrt{3\pi}} \frac{\Delta x}{c} = 3.677 \times 10^{-18} \text{s}, \quad (\text{E.35})$$

is the lowest time step that can be used in order for the method to be stable. To be on the safe side, I usually aim for a step size of 1×10^{-19} to 1×10^{-18} s for this level of

resolution. Spatially, one is limited to two lattice cells per wavelength [101]; however this is not a relevant limitation given the size of systems I wish to examine and the resolution required. One improvement that may be considered is the introduction of higher order update equations to reduce the required time step size for the fields.

E.1.2 Introduction of the Source

In order to introduce EM fields into the system, a source is needed. This is a collection of lattice cells that generate fields. For this system, the source is designed to generate a continuous wave in the \hat{z} direction polarized in the y direction. This is implemented by adding field amplitudes in a number of chosen cells,

$$\begin{aligned} E'_y(\mathbf{r}, t) &= E_y(\mathbf{r}, t) + dt \frac{\partial}{\partial t} (E_0(\mathbf{r}, t) \cos(\omega t + \phi(\mathbf{r}))), \\ H'_x(\mathbf{r}, t) &= H_x(\mathbf{r}, t) + dt \frac{\partial}{\partial t} \left(\frac{E_0(\mathbf{r}, t)}{c} \cos(\omega t + \phi(\mathbf{r})) \right), \end{aligned} \quad (\text{E.36})$$

where $\phi(\mathbf{r})$ is a positional phase shift chosen to ensure all spatial source cells are in phase regardless of position. In a PSTD method, implementing a single point source is not ideal as the Fast-Fourier Transform (FFT) of a Dirac-delta function (or any sharp discontinuity) is not numerically stable [101, 102] (it skews the high frequency terms in the FFT). This noise, if high enough, can cause excitation in lattice cell sites that precedes the incoming field.

One way to mitigate this noise is to spread the source over multiple cells [101, 102]. This reduces the sharp discontinuity in the electric field and reduces the exaggeration of the higher frequency modes in the numerical FFT. The more cells that are used to generate fields, the lower the numerical noise will be; however, care must be taken to ensure that these generating cells are far enough away from the distribution to not greatly impact the fields around an object of interest. In fact, only 4-6 cells need to

be used to reduce this noise to minimal (about 1-2 percent) levels [102].

For this particular work, I have opted to use a normalized Gaussian smoothing function over a width of $N=5$ lattice cells. For a z -propagating plane wave in this case,

$$E_0(\mathbf{r}_i, t) = E_{0,incident} \left(\exp\left(\frac{-(k_i - k_3)^2}{2(1)^2}\right) \right) / \sum_i^5 \left(\exp\left(\frac{-(k_i - k_3)^2}{2(1)^2}\right) \right), \quad (\text{E.37})$$

where k_i is the lattice cell number and k_3 is the source cell. Although this leads to the very first wavefront (from $k_z - k_{z_0} = 2$) reaching the system at a earlier time than if I were to use a single source at $i = 3$, this time difference ($\approx \frac{0.5nm}{c} = 5 \times 10^{-18}s$) is negligible when compared to the smallest quantum time-scale in almost all systems ($1/\omega_0 \approx 2 \times 10^{-15}s$).

E.1.3 Parallel Implementation

Due to the large computational requirement of running a relatively large simulation, it is essential that this overall calculation be done in parallel. The two main calculations that need to be performed are the update (time evolution) of the density matrix and the update (time evolution) of the fields. Both of these calculations are relatively easy to implement in parallel.

The main challenge in paralleling the overall calculation is in updating the fields. This is due to the fact that the gradient needs to be calculated across all spatial locations which may be present on different cores. Luckily this is handled by the use of the FFTW [120] MPI package which takes care of the parallel optimized Fourier transform for a 3D lattice. This is also one of the main benefits of using a Fourier transform to update the fields (as opposed to a basis function) as this calculation is simple to process across different cores.

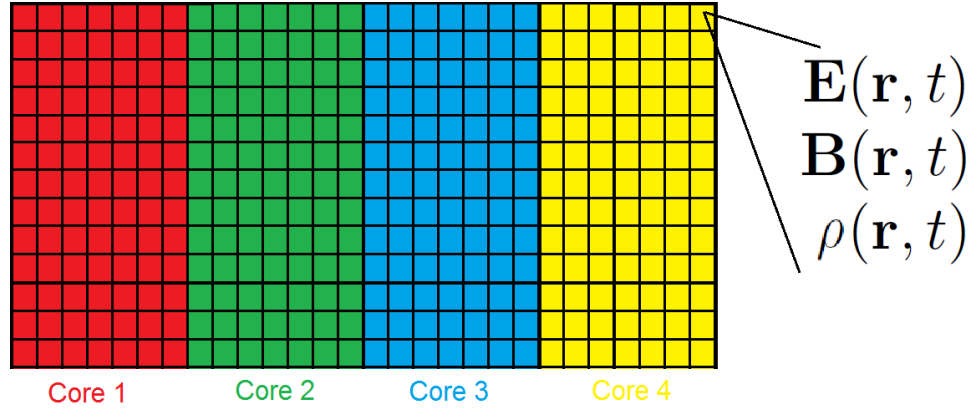


Figure E.1: Parallel scheme for performing the PSTD calculation; coarse-grain lattice cells are arranged and split amongst cores according to the x-position. At each lattice-cell centre, electric fields and density matrices are tracked in real-time and updated.

The updates to the density matrix can be done explicitly in parallel as none of the local state densities depend on one another, this allows them to be done locally. In these calculations, the local density matrices are calculated on the same cores that store the local electric field data. While they could be distributed evenly between cores (in the case of non-uniform distributions of atoms), the amount of time needed to transfer field data from the core in which it is stored to another core would most likely exceed the small amount of time needed to process additional local density matrices unless the system was greatly non-uniform. An overall schematic for the parallel scheme can be seen below in Figure E.1.

When performing most calculations involving dense collections of quantum systems (results of Chapter 4), 10-16 CPU days were required for each individual simulation. Computing resources were provided by SHARCNET [121].

Appendix F

Ensemble fitting parameters

Included in this section are the specific fitting parameters to the ensemble averaged statistical fits used to extract the effective coherence rates. The fitting function is of the form:

$$\rho_{ey,ey} = a \exp(-\gamma_{ens}t) \cos(\Omega t) + b + c \exp(-gt), \quad (\text{F.1})$$

and γ_{ens} is extracted to give a measure of the effective decoherence rates. The following are the fitting parameters for various ensemble number densities N_a .

$$N_a = 1 \times 10^{27} \text{m}^{-3}$$

$$\gamma_{ens} = 6.2434 \times 10^{11} \pm 1.219 \times 10^9 \text{ Hz}$$

$$\Omega = 2.061 \times 10^{14} \pm 6.231 \times 10^8 \text{ Hz}$$

$$c = 0.455385 \pm 0.01248$$

$$a = -0.502126 \pm 9.996 \times 10^5$$

$$g = 8.98337 \times 10^{11} \pm 3.032 \times 10^{11} \text{ Hz}$$

$$b = 0.0422173 \pm 0.01241$$

$$N_a = 2.5 \times 10^{27} \text{m}^{-3}$$

$$\gamma_{ens} = 1.45468 \times 10^{13} \pm 1.355 \times 10^{10} \text{ Hz}$$

$$\Omega = 2.02565 \times 10^{14} \pm 9.594 \times 10^9 Hz$$

$$c = 0.308686 \pm 0.0004984$$

$$a = -0.639961 \pm 0.0004188$$

$$g = 6.17348 \times 10^{12} \pm 2.723 \times 10^{10} Hz$$

$$b = 0.217666 \pm 0.000607$$

$$\mathbf{N_a} = 4 \times 10^{27} \mathbf{m}^{-3}$$

$$\gamma_{ens} = 3.55518 \times 10^{13} \pm 1.355 \times 10^{10} Hz$$

$$\Omega = 1.85383 \times 10^{14} \pm 2.419 \times 10^{10} Hz$$

$$c = 0.304753 \pm 0.0002499$$

$$a = -0.6727 \pm 0.0004625$$

$$g = 1.84484 \times 10^{13} \pm 3.006 \times 10^{10} Hz$$

$$b = 0.282172 \pm 8.938 \times 10^{-05}$$

$$\mathbf{N_a} = 5 \times 10^{27} \mathbf{m}^{-3}$$

$$\gamma_{ens} = 5.07228 \times 10^{13} \pm 5.511 \times 10^{10} Hz$$

$$\Omega = 1.66319 \times 10^{14} \pm 3.675 \times 10^{10} Hz$$

$$c = 0.266439 \pm 6.258 \times 10^{-05}$$

$$a = -0.683112 \pm 0.0005458$$

$$g = 2.63727 \times 10^{13} \pm 3.933 \times 10^{10} Hz$$

$$b = 0.337431 \pm 0.0003251$$

$$\mathbf{N_a} = 7.5 \times 10^{27} \mathbf{m}^{-3}$$

$$\gamma_{ens} = 5.30576 \times 10^{13} \pm 1.897 \times 10^{11} Hz$$

$$\Omega = 2.8366 \times 10^{14} \pm 1.369 \times 10^{11} Hz$$

$$c = 0.302916 \pm 0.0001589$$

$$a = -0.161232 \pm 0.0004006$$

$$g = 9.19251 \times 10^{12} \pm 2.445 \times 10^{10} \text{ Hz}$$

$$b = -0.18188 \pm 0.0001505$$

$$\mathbf{N_a} = 1 \times 10^{28} \mathbf{m^{-3}}$$

$$\gamma_{ens} = 5.1942 \times 10^{13} \pm 2.099 \times 10^{11} \text{ Hz}$$

$$\Omega = 4.41401 \times 10^{14} \pm 1.507 \times 10^{11} \text{ Hz}$$

$$c = 0.683556 \pm 0.002756$$

$$a = -0.0769707 \pm 0.0002182$$

$$g = 1.47507 \times 10^{12} \pm 7.964 \times 10^9 \text{ Hz}$$

$$b = -0.632966 \pm 0.002712$$

Saturation Fit

This overall behaviour of these fitting parameters appears to be best described by a saturation curve, similar to that in Fermi statistics. This takes the form of the logistic function [108] with:

$$\gamma_{ens} = \frac{L}{1 + \exp(-k(N_a - a))}. \quad (\text{F.2})$$

$$\mathbf{E} = 1.5 \times 10^9 \mathbf{V/m}$$

$$L = 5.31639 \times 10^{13} \pm 1.479 \times 10^{12} \text{ Hz}$$

$$k = 1.3532 \times 10^{-27} \pm 1.639 \times 10^{-28} \text{ m}^3$$

$$a = 3.33738 \times 10^{27} \pm 1.189 \times 10^{26} \text{ m}^{-3}$$

$$\mathbf{E} = 7.5 \times 10^8 \mathbf{V/m}$$

$$L = 3.05586 \times 10^{13} \pm 2.594 \times 10^{11} \text{ Hz}$$

$$k = 2.28608 \times 10^{-27} \pm 1.229 \times 10^{-28} \text{ m}^3$$

$$a = 1.76173 \times 10^{27} \pm 4.229 \times 10^{25} \text{ m}^{-3}$$

Bibliography

- [1] David J. Tannor and Stuart A. Rice. Control of selectivity of chemical reaction via control of wave packet evolution. *J. Chem. Phys.*, 83(10):5013–5018, 1985.
- [2] Paul Brumer and Moshe Shapiro. Control of unimolecular reactions using coherent light. *Chem. Phys. Lett.*, 126(6):541–546, 1986.
- [3] Anthony P. Peirce, Mohammed A. Dahleh, and Herschel Rabitz. Optimal control of quantum-mechanical systems: Existence, numerical approximation, and applications. *Phys. Rev. A*, 37(12):4950, 1988.
- [4] J. R. Kuklinski, U. Gaubatz, F. T. Hioe, and K. Bergmann. Adiabatic population transfer in a three-level system driven by delayed laser pulses. *Phys. Rev. A*, 40:6741–6744, 1989.
- [5] Michael Fleischhauer, Atac Imamoglu, and Jonathan P. Marangos. Electromagnetically induced transparency: Optics in coherent media. *Rev. Mod. Phys.*, 77:633–673, 2005.
- [6] Juan I. Cirac and Peter Zoller. Quantum computations with cold trapped ions. *Phys. Rev. Lett.*, 74(20):4091, 1995.
- [7] Daniel Loss and David P. DiVincenzo. Quantum computation with quantum dots. *Phys. Rev. A*, 57:120–126, 1998.

- [8] John von Neumann. *Mathematical foundations of quantum mechanics*. Number 2. Princeton University Press, 1955.
- [9] A.A. Markov. *Theory of Algorithms*. Acad. Sci. USSR, 1954.
- [10] A.R.P. Rau. Unitary integration of quantum Liouville-Bloch equations. *Phys. Rev. Lett.*, 81:4785–4789, 1998.
- [11] A.R.P. Rau and K. Unnikrishnan. Evolution operators and wave functions in a time-dependent electric field. *Phys. Lett. A*, 222(5):304 – 308, 1996.
- [12] David J. Tannor. *Introduction to Quantum Mechanics: A Time-Dependent Perspective*. University Science Books, 2007.
- [13] David J. Tannor, Ronnie Kosloff, and Stuart A. Rice. Coherent pulse sequence induced control of selectivity of reactions: Exact quantum mechanical calculations. *J. Chem. Phys.*, 85(10):5805–5820, 1986.
- [14] Doron Meshulach and Yaron Silberberg. Coherent quantum control of two-photon transitions by a femtosecond laser pulse. *Nature*, 396(6708):239–242, 1998.
- [15] T.C. Weinacht, Jaewook Ahn, and Phil H. Bucksbaum. Controlling the shape of a quantum wavefunction. *Nature*, 397(6716):233–235, 1999.
- [16] Herschel A. Rabitz, Michael M. Hsieh, and Carey M. Rosenthal. Quantum optimally controlled transition landscapes. *Science*, 303(5666):1998–2001, 2004.
- [17] Shi-Yao Zhu and Marlan O. Scully. Spectral line elimination and spontaneous emission cancellation via quantum interference. *Phys. Rev. Lett.*, 76(3):388, 1996.
- [18] W. Wernsdorfer and R. Sessoli. Quantum phase interference and parity effects in magnetic molecular clusters. *Science*, 284(5411):133–135, 1999.

- [19] Brian P. Anderson and M. A. Kasevich. Macroscopic quantum interference from atomic tunnel arrays. *Science*, 282(5394):1686–1689, 1998.
- [20] C. Rangan and P. H. Bucksbaum. Optimally shaped terahertz pulses for phase retrieval in a Rydberg-atom data register. *Phys. Rev. A*, 64:033417, 2001.
- [21] Lukas Novotny and Bert Hecht. *Principles of Nano-Optics*. Cambridge University Press, 2006. Chapter 8.
- [22] S. Swain, P. Zhou, and Z. Ficek. Intensity-intensity correlations and quantum interference in a driven three-level atom. *Phys. Rev. A*, 61:043410, 2000.
- [23] F. Carreo, M. A. Antón, and Oscar G. Caldern. Intensity-intensity correlations in a V-type atom driven by a coherent field in a broadband squeezed vacuum. *J. Opt. B*, 6(7):315, 2004.
- [24] Tigran S. Varzhapetyan, Hebin Li, Gombojav O. Ariunbold, Vladimir A. Sautenkov, Yuri V. Rostovtsev, and Marlan O. Scully. Intensity correlations in a coherently prepared Rb vapor in a magnetic field. *Opt. Commun*, 282(1):39 – 44, 2009.
- [25] Gombojav O. Ariunbold, Yuri V. Rostovtsev, Vladimir A. Sautenkov, and Marlan O. Scully. Intensity correlation and anti-correlations in coherently driven atomic vapor. *J. Mod. Opt.*, 57:1417–1427, 2010.
- [26] Wang Fei, Shi Wen-Xing, and Gong Cheng. Effects of spontaneously generated coherence on intensity-intensity correlation in a driven Y-type atom. *Commun. Theor. Phys*, 56(6):1079, 2011.
- [27] Jun-Tao Chang, Jörg Evers, and M. Suhail Zubairy. Distilling two-atom distance information from intensity-intensity correlation functions. *Phys. Rev. A*, 74(4):043820, 2006.

- [28] D. P. DiVincenzo. The physical implementation of quantum computation. *Fortschr. Phys.*, 48:771, 2000.
- [29] E. J. Griffith, C. D. Hill, J. F. Ralph, H. M. Wiseman, and Kurt Jacobs. Rapid-state purification protocols for a Cooper pair box. *Phys. Rev. B*, 75:014511, 2007.
- [30] M. Kleinmann, H. Kampermann, T. Meyer, and D. Bruß. Physical purification of quantum states. *Phys. Rev. A*, 73:062309, 2006.
- [31] Jan Bouda and Vladimír Bužek. Purification and correlated measurements of bipartite mixed states. *Phys. Rev. A*, 65:034304, 2002.
- [32] Jian-Wei Pan, Sara Gasparoni, Rupert Ursin, Gregor Weihs, and Anton Zeilinger. Experimental entanglement purification of arbitrary unknown states. *Nature*, 423:417–422, 2003.
- [33] Howard Mark Wiseman and J.F. Ralph. Reconsidering rapid qubit purification by feedback. *New J. Phys.*, 8:90, 2006.
- [34] Hongxing Xu, Xue-Hua Wang, Martin P. Persson, H. Q. Xu, Mikael Käll, and Peter Johansson. Unified treatment of fluorescence and Raman scattering processes near metal surfaces. *Phys. Rev. Lett.*, 93:243002, 2004.
- [35] Hongxing Xu, Javier Aizpurua, Mikael Käll, and Peter Apell. Electromagnetic contributions to single-molecule sensitivity in surface-enhanced Raman scattering. *Phys. Rev. E*, 62:4318–4324, 2000.
- [36] M. Ringler, A. Schwemer, M. Wunderlich, A. Nichtl, K. Kürzinger, T. A. Klar, and J. Feldmann. Shaping emission spectra of fluorescent molecules with single plasmonic nanoresonators. *Phys. Rev. Lett.*, 100:203002, 2008.

- [37] A. P. Alivisatos. Semiconductor clusters, nanocrystals, and quantum dots. *Science*, 271(5251):933, 1996.
- [38] Xiaodong Xu, Bo Sun, Paul R. Berman, Duncan G. Steel, Allan S. Bracker, Dan Gammon, and L. J. Sham. Coherent optical spectroscopy of a strongly driven quantum dot. *Science*, 317(5840):929–932, 2007.
- [39] Xiaoqin Li, Yanwen Wu, Duncan Steel, D. Gammon, T. H. Stievater, D. S. Katzer, D. Park, C. Piermarocchi, and L. J. Sham. An all-optical quantum gate in a semiconductor quantum dot. *Science*, 301(5634):809–811, 2003.
- [40] Alexander Shnirman, Gerd Schön, and Ziv Hermon. Quantum manipulations of small Josephson junctions. *Phys. Rev. Lett.*, 79:2371–2374, 1997.
- [41] Hanhee Paik, D. I. Schuster, Lev S. Bishop, G. Kirchmair, G. Catelani, A. P. Sears, B. R. Johnson, M. J. Reagor, L. Frunzio, L. I. Glazman, S. M. Girvin, M. H. Devoret, and R. J. Schoelkopf. Observation of high coherence in Josephson junction qubits measured in a three-dimensional circuit QED architecture. *Phys. Rev. Lett.*, 107:240501, 2011.
- [42] P. Goy, J. M. Raimond, M. Gross, and S. Haroche. Observation of cavity-enhanced single-atom spontaneous emission. *Phys. Rev. Lett.*, 50:1903–1906, 1983.
- [43] D. J. Heinzen, J. J. Childs, J. E. Thomas, and M. S. Feld. Enhanced and inhibited visible spontaneous emission by atoms in a confocal resonator. *Phys. Rev. Lett.*, 58:1320–1323, 1987.
- [44] Y. Yamamoto, S. Machida, Y. Horikoshi, K. Igeta, and G. Bjrk. Enhanced and inhibited spontaneous emission of free excitons in GaAs quantum wells in a microcavity. *Opt. Commun.*, 80(5):337 – 342, 1991.

- [45] A. Bienfait, J. J. Pla, Y. Kubo, X. Zhou, M. Stern, C. C. Lo, C. D. Weis, T. Schenkel, D. Vion, D. Esteve, J. J. L. Morton, and P. Bertet. Controlling spin relaxation with a cavity. *Nature*, 531:74–77, 2016.
- [46] Nikhil Ganesh, Wei Zhang, Patrick C Mathias, Edmond Chow, JANT Soares, Viktor Malyarchuk, Adam D Smith, and Brian T Cunningham. Enhanced fluorescence emission from quantum dots on a photonic crystal surface. *Nat. Nanotechnol.*, 2(8):515–520, 2007.
- [47] Maxim Sukharev and Abraham Nitzan. Numerical studies of the interaction of an atomic sample with the electromagnetic field in two dimensions. *Phys. Rev. A*, 84:043802, 2011.
- [48] Raiju Puthumpally-Joseph, Maxim Sukharev, Osman Atabek, and Eric Charron. Dipole-induced electromagnetic transparency. *Phys. Rev. Lett.*, 113:163603, 2014.
- [49] Alexei Deinega and Tamar Seideman. Self-interaction-free approaches for self-consistent solution of the Maxwell-Liouville equations. *Phys. Rev. A*, 89:022501, 2014.
- [50] S. D. Jenkins, J. Ruostekoski, J. Javanainen, R. Bourgain, S. Jennewein, Y. R. P. Sortais, and A. Browaeys. Optical resonance shifts in the fluorescence of thermal and cold atomic gases. *Phys. Rev. Lett.*, 116:183601, 2016.
- [51] Juha Javanainen, Janne Ruostekoski, Yi Li, and Sung-Mi Yoo. Shifts of a resonance line in a dense atomic sample. *Phys. Rev. Lett.*, 112:113603, 2014.
- [52] A. S. Kuraptsev and I. M. Sokolov. Spontaneous decay of an atom excited in a dense and disordered atomic ensemble: Quantum microscopic approach. *Phys. Rev. A*, 90:012511, 2014.

- [53] Eran Sela, Victor Fleurov, and Vladimir A. Yurovsky. Molecular spectra in collective dicke states. *Phys. Rev. A*, 94:033848, 2016.
- [54] I. M. Sokolov, D. V. Kupriyanov, and M. D. Havey. Microscopic theory of scattering of weak electromagnetic radiation by a dense ensemble of ultracold atoms. *J. Exp. Theor. Phys*, 112(2):246–260, 2011.
- [55] Maxim Sukharev and Eric Charron. Molecular plasmonics: The role of rovibrational molecular states in exciton-plasmon materials under strong-coupling conditions. *Phys. Rev. B*, 95:115406, 2017.
- [56] H.A. Lorentz. *The theory of electrons and its applications to the phenomena of light and radiant heat*. Dover Publications, Inc, New York, NY, USA, 2 edition, 1952.
- [57] Tobias Preis, Peter Virnau, Wolfgang Paul, and Johannes J. Schneider. GPU accelerated Monte Carlo simulation of the 2D and 3D Ising model. *J. Comput. Phys*, 228(12):4468–4477, 2009.
- [58] Riccardo Guida and J. Zinn-Justin. 3D Ising model: the scaling equation of state. *Nucl. Phys. B*, 489(3):626–652, 1997.
- [59] T. Abdallah, T.A. El-Brolosy, M.B. Mohamed, K. Easawi, S. Negm, and H. Talaat. Effect of shape and interstice on surface enhanced raman scattering (sers) of molecules adsorbed on gold nanoparticles in the near-dipole and quadrupole regions. *J. Raman Spectrosc.*, 43(12):1924–1930, 2012.
- [60] Samuel L. Oliveira and Stephen C. Rand. Intense nonlinear magnetic dipole radiation at optical frequencies: Molecular scattering in a dielectric liquid. *Phys. Rev. Lett.*, 98:093901, 2007.

- [61] Stephen C. Rand, W.M. Fisher, and Samuel L. Oliveira. Optically induced magnetization in homogeneous, undoped dielectric media. *J. Opt. Soc. Am B*, 25(7):1106–1117, 2008.
- [62] Stephen C. Rand. Quantum theory of coherent transverse optical magnetism. *J. Opt. Soc. Am. B*, 26(12):B120–B129, 2009.
- [63] Natthi L. Sharma. Comment on “Intense nonlinear magnetic dipole radiation at optical frequencies: Molecular scattering in a dielectric liquid”. *Phys. Rev. Lett.*, 102:119403, 2009.
- [64] S. L. Oliveira and S. C. Rand. Oliveira and Rand reply:. *Phys. Rev. Lett.*, 102:119404, 2009.
- [65] Peter Palffy-Muhoray. Comment on “Intense nonlinear magnetic dipole radiation at optical frequencies: Molecular scattering in a dielectric liquid”. *Phys. Rev. Lett.*, 99:189401, 2007.
- [66] Samuel L. Oliveira and Stephen C. Rand. Oliveira and Rand reply:. *Phys. Rev. Lett.*, 99:189402, 2007.
- [67] W. M. Fisher and S. C. Rand. Light-induced dynamics in the Lorentz oscillator model with magnetic forces. *Phys. Rev. A*, 82:013802, 2010.
- [68] H. Huang, S.-Y. Zhu, M. S. Zubairy, and M. O. Scully. Two-time intensity correlation in a driven three-level system. *Phys. Rev. A*, 53:1834–1838, 1996.
- [69] K.-J. Boller, A. Imamoglu, and S. E. Harris. Observation of electromagnetically induced transparency. *Phys. Rev. Lett.*, 66:2593–2596, 1991.
- [70] Anthony O’Keefe and David A.G. Deacon. Cavity ring-down optical spectrometer for absorption measurements using pulsed laser sources. *Rev. Sci. Instrum.*, 59(12):2544–2551, 1988.

- [71] T. Udem, J. Reichert, R. Holzwarth, and TW Hänsch. Absolute optical frequency measurement of the cesium D 1 line with a mode-locked laser. *Phys. Rev. Lett.*, 82(18):3568, 1999.
- [72] Thang B. Hoang, Gleb M. Akselrod, Christos Argyropoulos, Jiani Huang, David R. Smith, and Maiken H. Mikkelsen. Ultrafast spontaneous emission source using plasmonic nanoantennas. *Nat. Commun.*, 6:7788, 2015.
- [73] E.M. Purcell. Spontaneous emission probabilities at radio frequencies. *Phys. Rev.*, 69(681), 1946.
- [74] Mark I. Stockman. Nanoplasmonics: past, present, and glimpse into future. *Opt. Express*, 19(22):22029–22106, 2011.
- [75] Patrick Rooney, Asad Rezaee, Songbo Xu, Touraj Manifar, Abdollah Hassan-zadeh, Ganna Podoprygorina, Volker Böhmer, Chitra Rangan, and Silvia Mittler. Control of surface plasmon resonances in dielectrically coated proximate gold nanoparticles immobilized on a substrate. *Phys. Rev. B*, 77:235446, 2008.
- [76] S. M. Hashemi Rafsanjani, T. Cheng, S. Mittler, and C. Rangan. Theoretical proposal for a biosensing approach based on a linear array of immobilized gold nanoparticles. *J. Appl. Phys.*, 107(9), 2010.
- [77] Vincenzo Giannini, Antonio I. Fernández-Domínguez, Yannick Sonnefraud, Tyler Roschuk, Roberto Fernández-García, and Stefan A. Maier. Controlling light localization and light–matter interactions with nanoplasmonics. *Small*, 6(22):2498–2507, 2010.
- [78] Cecilia Noguez. Surface plasmons on metal nanoparticles: The influence of shape and physical environment. *J. Phys. Chem. C*, 111(10):3806–3819, 2007.

- [79] M. A. Antón, F. Carreño, Sonia Melle, Oscar G. Calderón, E. Cabrera-Granado, Joel Cox, and Mahi R. Singh. Plasmonic effects in excitonic population transfer in a driven semiconductor-metal nanoparticle hybrid system. *Phys. Rev. B*, 86:155305, 2012.
- [80] Ellen J. Zeman and George C. Schatz. An accurate electromagnetic theory study of surface enhancement factors for silver, gold, copper, lithium, sodium, aluminum, gallium, indium, zinc, and cadmium. *J. Phys. Chem*, 91(3):634–643, 1987.
- [81] Bruce T. Draine and Piotr J. Flatau. Discrete-dipole approximation for scattering calculations. *J. Opt. Soc. Am A*, 11(4):1491–1499, 1994.
- [82] Qiang Fu and Wenbo Sun. Mie theory for light scattering by a spherical particle in an absorbing medium. *Appl. Opt.*, 40(9):1354–1361, 2001.
- [83] J.R. Hodgkinson and I. Greenleaves. Computations of light-scattering and extinction by spheres according to diffraction and geometrical optics, and some comparisons with the Mie theory. *J. Opt. Soc. Am*, 53(5):577–588, 1963.
- [84] Lumerical Solutions Inc [http://www.lumerical.com/tcad products/fdtd/](http://www.lumerical.com/tcad_products/fdtd/).
- [85] Kirk E. Jordan, Gerard R. Richter, and Ping Sheng. An efficient numerical evaluation of the Green’s function for the Helmholtz operator on periodic structures. *J. Comput. Phys*, 63(1):222–235, 1986.
- [86] Filippo Capolino, Donald R. Wilton, and William A. Johnson. Efficient computation of the 2-D Green’s function for 1-D periodic structures using the Ewald method. *IEEE Trans. Antennas*, 53(9):2977–2984, 2005.
- [87] T. Cheng, C. Rangan, and J. E. Sipe. Metallic nanoparticles on waveguide

- structures: effects on waveguide mode properties and the promise of sensing applications: erratum. *J. Opt. Soc. Am. B*, 31(11):2845–2845, 2014.
- [88] J. D. Jackson. *Classical Electrodynamics (3rd ed)*. Wiley, New York, 1998.
- [89] P. B. Johnson and R. W. Christy. Optical constants of the noble metals. *Phys. Rev. B*, 6:4370–4379, 1972.
- [90] S. Pillai, K. R. Catchpole, T. Trupke, and M. A. Green. Surface plasmon enhanced silicon solar cells. *J. Appl. Phys*, 101(9), 2007.
- [91] Emmanuel Fort and Samuel Grésillon. Surface enhanced fluorescence. *J. of Phys. D*, 41(1):013001, 2007.
- [92] H. Khosravi and R. Loudon. Vacuum field fluctuations and spontaneous emission in a dielectric slab. *Proc. R. Soc. A*, 436(1897):373–389, 1992.
- [93] Prashant K. Jain, Xiaohua Huang, Ivan H. El-Sayed, and Mostafa A. El-Sayed. Noble metals on the nanoscale: Optical and photothermal properties and some applications in imaging, sensing, biology, and medicine. *Accounts of Chemical Research*, 41(12):1578–1586, 2008. PMID: 18447366.
- [94] Dong Ick Son, Byoung Wook Kwon, Dong Hee Park, Won-Seon Seo, Yeonjin Yi, Basavaraj Angadi, Chang-Lyoul Lee, and Won Kook Choi. Emissive ZnO-graphene quantum dots for white-light-emitting diodes. *Nat. Nanotechnol.*, 7(7):465–471, 2012.
- [95] James R. Morris and Bruce W. Shore. Reduction of degenerate two-level excitation to independent two-state systems. *Phys. Rev. A*, 27:906–912, 1983.
- [96] A. A. Rangelov, N. V. Vitanov, and B. W. Shore. Extension of the Morris-Shore transformation to multilevel ladders. *Phys. Rev. A*, 74:053402, 2006.

- [97] E. Arimondo. *Coherent population trapping in laser spectroscopy*, volume 35, page 257–354. Elsevier, Amsterdam, 1996.
- [98] H.R. Gray, R.M. Whitley, and C.R. Stroud. Coherent trapping of atomic populations. *Opt. Lett.*, 3(6):218–220, 1978.
- [99] C. S. DiLoreto and C. Rangan. Polarization control of spontaneous emission for rapid quantum-state initialization. *Phys. Rev. A*, 95:043834, 2017.
- [100] Claudia Strümpel, Michelle McCann, Guy Beaucarne, Vladimir Arkhipov, Abdelilah Slaoui, V. Švrček, C. Del Cañizo, and I. Tobias. Modifying the solar spectrum to enhance silicon solar cell efficiency - an overview of available materials. *Sol. Energ. Mat. Sol. Cells*, 91(4):238–249, 2007.
- [101] Q. H. Liu. The PSTD algorithm: A time-domain method requiring only two cells per wavelength. *Microw. Opt. Technol. Lett.*, 15(3):158–165, 1997.
- [102] Qing Huo Liu. Large-scale simulations of electromagnetic and acoustic measurements using the pseudospectral time-domain (PSTD) algorithm. *IEEE T. Geosci. Remote*, 37(2):917–926, 1999.
- [103] Karl S. Kunz and Raymond J. Luebbers. *The finite difference time domain method for electromagnetics*. CRC press, 1993.
- [104] A. Fratolocchi, C. Conti, and G. Ruocco. Three-dimensional *ab initio* investigation of light-matter interaction in Mie lasers. *Phys. Rev. A*, 78:013806, 2008.
- [105] Alexander Munro Davie and Andrew James Stothers. Improved bound for complexity of matrix multiplication. *Proc. R. Soc. A*, 143(02):351–369, 2013.
- [106] Christopher DiLoreto. The effect of chain rigidity on pore formation by peptide action in model polymeric bilayers. *Electronic Theses and Dissertations, University of Guelph*, 2012. <http://hdl.handle.net/10214/3919>.

- [107] A. V. Gruzinov and P. H. Diamond. Self-consistent theory of mean-field electrodynamics. *Phys. Rev. Lett.*, 72:1651–1653, 1994.
- [108] Neil A. Gershenfeld. *The nature of mathematical modeling*. Cambridge University Press, 1999.
- [109] Natthi L. Sharma, Ernest R. Behringer, and Rene C. Crombez. A study of electric dipole radiation via scattering of polarized laser light. *American Journal of Physics*, 71(12):1294–1302, 2003.
- [110] D.J. Griffiths. *Introduction to Electrodynamics*. Prentice Hall, 1999.
- [111] M. H. Shah, H. A. Camp, M. L. Trachy, G. Veshapidze, M. A. Gearba, and B. D. DePaola. Model-independent measurement of the excited fraction in a magneto-optical trap. *Phys. Rev. A*, 75:053418, 2007.
- [112] G. Veshapidze, J.-Y. Bang, C. W. Fehrenbach, H. Nguyen, and B. D. DePaola. Model-free measurement of the excited-state fraction in a ^{85}Rb magneto-optical trap. *Phys. Rev. A*, 91:053423, 2015.
- [113] H. Mabuchi and A.C. Doherty. Cavity quantum electrodynamics: coherence in context. *Science*, 298(5597):1372–1377, 2002.
- [114] David Press, Thaddeus D. Ladd, Bingyang Zhang, and Yoshihisa Yamamoto. Complete quantum control of a single quantum dot spin using ultrafast optical pulses. *Nature*, 456(7219):218–221, 2008.
- [115] Samuel G. Carter, Timothy M. Sweeney, Mijin Kim, Chul Soo Kim, Dmitry Solenov, Sophia E. Economou, Thomas L. Reinecke, Lily Yang, Allan S. Bracker, and Daniel Gammon. Quantum control of a spin qubit coupled to a photonic crystal cavity. *Nat. Photon*, 7(4):329–334, 2013.

- [116] W. M. Haynes. *CRC Handbook of Chemistry and Physics (Online)*. CRC Press, 97th edition, 1978.
- [117] Maple 11 <http://www.maplesoft.com/>.
- [118] Āaslav Brukner and Anton Zeilinger. Operationally invariant information in quantum measurements. *Phys. Rev. Lett.*, 83:3354–3357, 1999.
- [119] Jean-Pierre Brenger. Perfectly matched layer (PML) for computational electromagnetics. *Synthesis Lectures on Computational Electromagnetics*, 2(1):1–117, 2007.
- [120] Matteo Frigo and Steven G. Johnson. The design and implementation of FFTW3. *Proceedings of the IEEE*, 93(2):216–231, 2005. Special issue on “Program Generation, Optimization, and Platform Adaptation”.
- [121] SHARCNET (www.sharcnet.ca) is a consortium of colleges, universities and research institutes operating a network of high-performance computer clusters across south western, central and northern Ontario.
- [122] Jean-Pierre Berenger. A perfectly matched layer for the absorption of electromagnetic waves. *J. Comput. Phys.*, 114(2):185–200, 1994.
- [123] Stephen D. Gedney. Introduction to the finite-difference time-domain (FDTD) method for electromagnetics. *Synthesis Lectures on Computational Electromagnetics*, 6(1):1–250, 2011.

Vita Auctoris

NAME: Christopher DiLoreto
PLACE OF BIRTH: Woodstock, ON
YEAR OF BIRTH: 1988
EDUCATION: Belle River District High School, Belle River, ON, 2006
University of Windsor, B.Sc., Windsor, ON, 2010
University of Guelph, M.Sc., Guelph, ON, 2012
University of Windsor, B.Ed., Windsor, ON, 2013